ECAP-2023-002

Investigation of Dosimetry for FLASH Radiotherapy with the Photon-Counting Pixel Detector Dosepix

Master's Thesis in Physics

Presented by
Markus Schneider
February 17 2023

Erlangen Centre for Astroparticle Physics
Physikalisches Institut IV
Friedrich-Alexander-Universität Erlangen-Nürnberg

Supervisor: PD Dr. Thilo Michel

Contents

1 Introduction

Radiotherapy is used in $60 - 70\,\%$ of all cancer treatments, making it the most utilized technique for cancer therapy ([Lin21][KSB$^+$20]). However, disadvantages of radiotherapy are skin reactions like the formation of scar tissue as well as the potential damaging of surrounding healthy tissue ([SHF$^+$20][Lin21]). Latter is addressed by some already existing treatment techniques like image-guided radiotherapy (IGRT), where imaging of the tumor is used simultaneously to its radiation, resulting in higher accuracy ([SKJ18]). Ion therapy also facilitates the sparing of healthy tissue. Often carbon ions are used for this kind of treatment. Heavy charged particles deposit most of their energy at the end of their track. Furthermore, less lateral scattering occurs compared to photon and electron irradiation, resulting in higher accuracy and sparing of healthy surrounding tissue. Ion therapy is mostly used for head, neck and prostate cancers [Lin21]. [SKJ18]

A rather new technique of cancer treatment is FLASH radiotherapy, where high dose rates in the order of several Gy/s are used, resulting in a very short total irradiation time ([RSM$^+$20]). In the first clinical treatment with FLASH radiotherapy, the treatment time only lasted 90 ms ([Lin21]). It is observed that the application of such high dose rates results in improved sparing of the healthy surrounding tissue whereas the destruction of cancer cells is similar to conventional radiotherapy at comparable applied total doses. This is known as FLASH effect. Due to the reduced damage of healthy tissue, FLASH radiotherapy is a promising tool for future cancer treatments. In clinical use, the dose must be applied to the patient precisely. Therefore, dose measurement systems, which are able to handle the challenges of such high dose rates must be established. [SHF$^+$20][Lin21]

In this thesis, the suitability of the Dosepix detector, a hybrid photon-counting pixel detector, for the determination of the applied dose at FLASH radiotherapy is investigated. At first, an ionization chamber, which is built out of the Dosepix detector, is used. It is supposed to determine the applied dose of the FLASH beam by measuring its secondary particles produced by the primary particle beam. The aim is to determine the dose of the radiation from the measured signal.
Furthermore, the effective sensor thickness of Dosepix is reduced by applying smaller bias voltages than the default value of 100 V, causing no full depletion of the sensor material. This leads to a reduced rate of detected events. The investigations focus

on the reduction of pile-up occuring at high radiation fluxes. Additionally, the signal from different types of particles measured by Dosepix with respect to bias voltage is examined.
The last chapter of this thesis deals with measurements of Dosepix performed inside a water phantom. The behavior of Dosepix under high dose rate electron radiation and the determination of depth dose distributions is investigated, allowing conclusions about the type and energy of the primary particles. The corresponding measurements are performed at the Strahlenklinik Erlangen ([Strb]).

2 Theoretical Background

Contents

In this chapter, the necessary theoretical background is discussed. Since different kinds of particles are used in this thesis, occurring interactions of photons, electrons, heavy charged particles, like alpha particles or protons, are discussed in the first section followed by the functionality of x-ray tubes and linear particle accelerators. Furthermore, essential quantities of dosimetry are described. Additionally, the Dosepix detector and its functionality are discussed. The chapter ends with a brief introduction of semiconductors.

2.1 Interaction of particles with matter

2.1.1 Interaction of photons with matter

Electromagnetic radiation can interact with matter via four different interaction channels: coherent scattering, Photoelectric effect, Compton scattering, and pair production. All of them will be discussed in the following. The descriptions are based on [Dem18], [Mes15] and [SKJ18].

Coherent scattering

Coherent scattering is also known as Rayleigh scattering. It takes place between a photon and an entire atom. No electrons are released from the atom, and no energy is transferred during this process. Therefore, the photon energy stays the same after the process. However, the incoming photon is deflected. Dosepix is not able to detect these interactions since no energy is deposited. [Dem18][Mes15]

Photoelectric effect

The Photoelectric effect occurs when a photon interacts with a bound electron of the irradiated material, causing the electron to be released from its atom. For the electron to be set free, the energy of the impinging photon must be higher than the work function W_a of the material. The photon transfers its total energy to the electron, thus the photon does not exist anymore after the interaction. The kinetic energy of the released electron is

$$E_\mathrm{kin} = h\nu - W_\mathrm{a} \tag{2.1.1}$$

Here, h is Planck's quantum of action, and ν is the frequency of the incoming photon. If an electron from an atom's inner shell is emitted, the atom will remain in an excited state which will cause an electron of an outer shell to occupy the free state in the inner shell. The respective energy difference can either be carried away via a fluorescence photon or transferred to an outer electron causing it to be released from its atom. These electrons are called Auger electrons. The energy of optical photons is smaller than the work function of most materials. Therefore the photoelectric effect mainly occurs at UV-, x-ray, and gamma radiation. In the measured deposition spectra, the photoelectric effect causes a full energy peak from which the energy of the photons can be determined. [Dem18][Mes15][SKJ18]

Compton scattering

Compton scattering, also called Compton effect or incoherent scattering, is another type of interaction between a photon and a bound electron. The photon does not transfer all of its energy to the electron during this process, meaning that the photon still exists after the process. The electron is released from its atom and the photon energy E_γ decreases, i.e. its wavelength λ decreases via:

$$\Delta\lambda = \frac{h}{m_\mathrm{e}c}(1 - \cos\phi_\mathrm{sc}) = \lambda_\mathrm{C}(1 - \cos\phi_\mathrm{sc}) \tag{2.1.2}$$

Here, h is Planck's quantum of action, m_e is the electron mass, ϕ_sc is the scattering angle between the electron and the photon, and $\lambda_\mathrm{C} = 2.4 \cdot 10^{-12}\,\mathrm{m}$ is the Compton wavelength of electrons. The change of the wavelength does not depend on the initial energy of the photon but only on the scattering angle. The energy of the photon after the interaction E'_γ is described by ([Kri17]):

$$E'_\gamma = \frac{E_\gamma}{1 + \frac{E_\gamma}{m_\mathrm{e} c^2}(1 - \cos\phi_\mathrm{sc})} \tag{2.1.3}$$

Here, c is the speed of light. The electrons released in this process produce a signal in the detector. The maximal energy transfer of the photon on the electron occurs at a scattering angle of 180°. This corresponds to the backscattering of the incoming photon. This energy corresponds to the Compton edge in the deposition spectrum. [Dem18][Mes15][SKJ18]

Pair production

Pair production occurs for photons with energies above 1022 keV which is twice the rest mass of electrons. A photon with sufficient energy can convert into an electron and a positron at pair production. This interaction occurs only within the Coulomb field of an atom because of energy and momentum conservation. Since such high photon energies are not reached in this thesis, pair production is negligible. [Dem18][Mes15]

2.1.2 Beer-Lambert law

Because of the mentioned interactions of absorption and scattering, the radiation intensity decreases within matter. It is described by the Beer-Lambert law ([Mes15]):

$$I(x) = I_0 \cdot e^{-\mu\rho x} \tag{2.1.4}$$

Here, I_0 is the initial intensity of the radiation, μ the mass attenuation coefficient, ρ the density of the material, and x the thickness of the material. The mass attenuation coefficient depends on the material and the photon energy. Its dependence on the photon energy is shown in figure 2.1.1 for silicon. Photoelectric effect is the dominant type of interaction for energies up until 60 keV. Above that, photons interact mainly via Compton scattering. [Mes15]

2.1.3 Interaction of massive particles with matter

Electrons and alpha particles are used in this thesis, too. Additionally, simulations with protons were performed. The interaction of massive particles differs from the ones of photons. Also, the interaction of electrons and heavy charged particles with matter cannot be described similarly. First, the interaction of electrons with matter is discussed.

Interaction of electrons with matter

There are mainly three types of interaction of electrons with matter. If an electron enters the Coulomb field of an atom, it is decelerated and loses kinetic energy which is emitted via photons. This kind of radiation is called bremsstrahlung. The energies of the emitted photons depend on the deceleration of the electrons. Therefore, bremsstrahlung is continuous. [Kri18]
The second interaction type is through collisions of the primary electrons with the

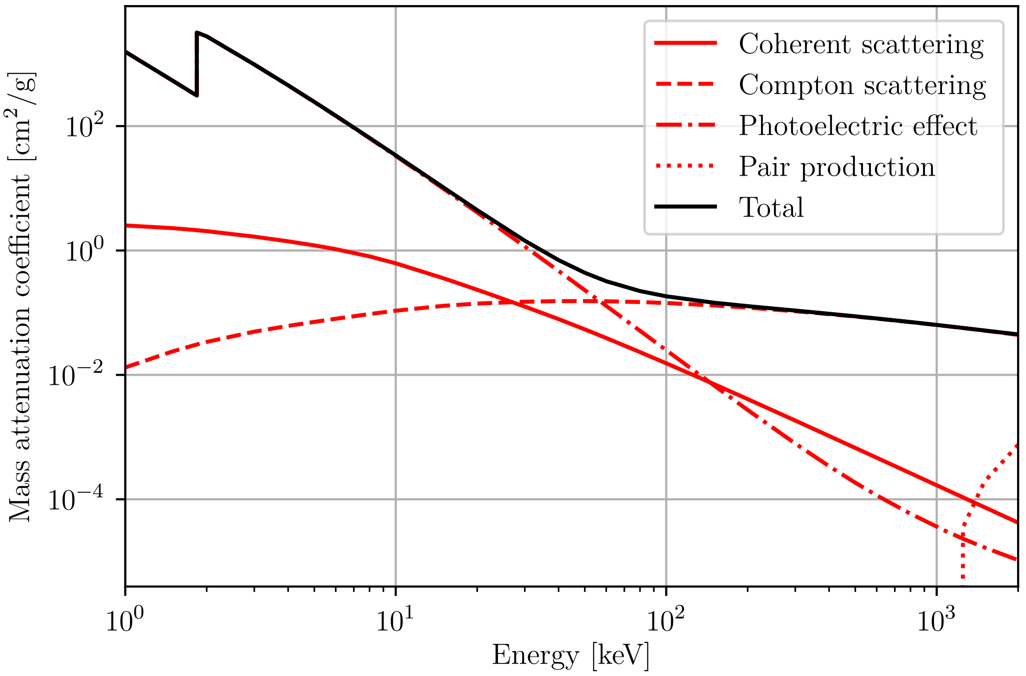

Figure 2.1.1: Mass attenuation coefficients for coherent scattering, Compton scattering, Photoelectric effect and pair production with respect to photon energy for silicon. Data is taken from [XCO].

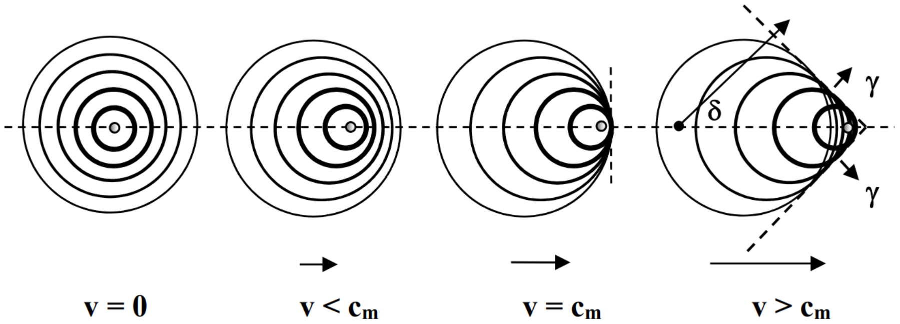

Figure 2.1.2: Scheme of the Cerenkov effect. If an electron moves faster than the speed of photons in a medium, a cone beam of Cerenkov light forms. The picture is taken from [Kri17].

shell electrons of the irradiated material. The shell electrons can be released from their atom, which results in a vacancy filled by another electron from an outer shell fills up this vacancy. The energy difference is emitted via a photon. This is called characteristic radiation. In contrast to bremsstrahlung, characteristic radiation can only have certain energies since only discrete energy transitions exist in atoms. [Kri18]
Since this thesis uses high energy electrons with energies up to 15 MeV, another type of interaction occurs: the Cerenkov effect. Electrons with such high energies move at nearly the speed of light. In a medium, the speed of photons is decreased. This is described by the refractive index n ([Dem17]):

$$n = \frac{c}{v_{\text{ph}}} \tag{2.1.5}$$

Here, c is the speed of light in vacuum and v_{ph} the speed of photons in the respective material. Because of the decreased speed of photons in material, high-energy electrons may move faster than photons. As a result, the electrons polarize the surrounding atoms, emitting electromagnetic radiation in the relaxation process. In the case of electrons being slower than photons, the photon radiation interferes deconstructively, so no radiation is observed. On the other hand, in the case of electrons faster than the photon radiation, the new wavefront cannot be reached by the previous one, resulting in the emission of electromagnetic radiation in the shape of a cone beam. This is sketched in figure 2.1.2. The radiation appears as optical blue light and is called Cerenkov light. The relation between the Cerenkov angle θ_{C} and the velocity of the electrons is ([KW16]):

$$\cos\theta_{\text{C}} = \frac{1}{\beta n} \tag{2.1.6}$$

The cone beam has an opening angle of $2\theta_\mathrm{C}$. β is the ratio between the velocity of the electrons and the speed of light: $\beta = \frac{v_\mathrm{e}}{c}$. Therefore, it is possible to determine the energy of the electrons from the Cerenkov angle. [KW16][Kri17]

Interaction of heavy charged particles with matter and Bragg peak

The interaction of heavy charged particles with matter is described in this section. The energy loss of heavy particles like alpha particles and protons is described by the Bethe-Bloch formula ([Kri17]):

$$S_\mathrm{col} = \left(\frac{dE}{dx}\right)_\mathrm{col} = \rho \cdot 4\pi \cdot r_\mathrm{e}^2 \cdot m_0 c^2 \cdot \frac{Z}{u \cdot A} \cdot z^2 \frac{1}{\beta^2} \cdot R_\mathrm{col}(\beta) \tag{2.1.7}$$

Here, ρ is the density of the material, r_e the classical electron radius, m_0 the rest mass of the particle, Z the atomic number of the material, u the unified atomic mass unit, A the mass number of the material, z the charge of the particle and R_col a rest function which additional dependencies. Charged particles only lose a small amount of energy in a single interaction, thus many interactions are required to stop a particle. Heavy charged particles lose their energy mainly due to interactions with shell electrons of the irradiated material. This leads to ionization or excitement of the atoms. There are soft and hard collisions. In case of soft collisions, the distance between the particles and its collision partner is much bigger than the radius of the interacting atom. This distance is called impact parameter. The particle interacts with the whole atom. In case of hard collisions, where the impact parameter is approximately as big as the radius of the interacting atom, the emitted electrons have much bigger energies, and larger scattering angles than the ones in soft collisions. The electrons emitted at hard collisions are called δ-electrons.

The energy loss increases with decreasing energy of heavy charged particles, resulting in the so-called Bragg peak, which appears at the stoppage of the particles. Figure 2.1.3 shows a scheme of the Bragg peak for alpha particles released from a ^{241}Am-source. The stopping power increases with the path length until the alpha particle is nearly stopped. In radiotherapy, the Bragg peak is instrumental since the particle energy can be chosen such that the particles are stopped in the tumor and deposit most of their energy there. The surrounding healthy tissue is spared. [Kri17][SKJ18]

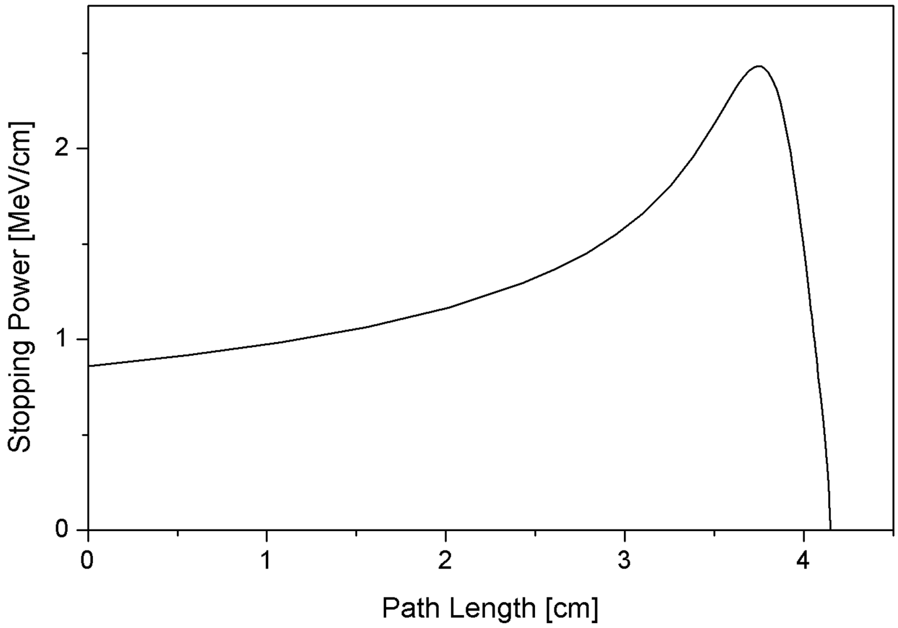

Figure 2.1.3: Bragg peak of ^{241}Am-alpha particles. The stopping power increases with the path length until the alpha particle is nearly stopped. The picture is taken from [Rad, edited].

2.2 Ionization chamber

Ionization chambers are often used for dosimetry in clinics to ensure the accuracy of the applied dose to the patient. They consist of a gas-filled condensator. Particles traversing the gas ionize the particles, leading to free electrons and ions as described in section 2.1.3. These charged particles are accelerated by applying a voltage between the electrodes, where they produce a measurable current, from which the deposited energy can be determined. Figure 2.2.1 illustrates the scheme of an ionization chamber. Ionization chambers are not sensitive to single particles but are suitable for high particle fluxes. A limiting effect of ionization chambers is recombination. It means that electrons and ions recombine before they reach the electrodes and do not contribute to the measured current. Therefore, a high voltage must be applied between the electrodes to increase the electric field. This leads to a higher acceleration of the ionized particles, resulting in a reduced recombination effect. For plate condensators, the electric field E is given by:

$$E = \frac{U}{d} \tag{2.2.1}$$

Here, U is the applied voltage between the electrodes, and d is the distance between the electrodes. The electric field can also be increased by decreasing the distance

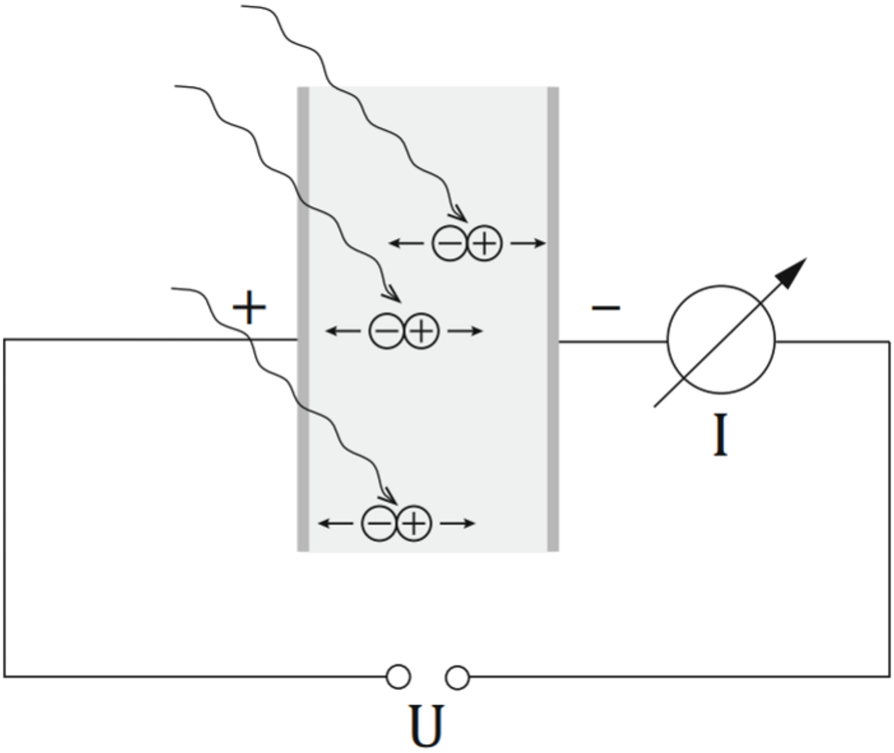

Figure 2.2.1: Scheme of an ionization chamber consisting of a gas-filled condensator. Irradiation ionizes the atoms, leading to free electrons and ions, which are accelerated towards the electrodes, producing a measurable current. Figure is taken from [KW16].

between the electrodes. Especially for ultra-high dose rates, recombination plays a significant role. [SKJ18][KW16]

2.3 Radiation systems

Two different radiation systems are used in this thesis. The first one is an x-ray tube. The second one is a linear particle accelerator which is used for the irradiation with electrons. The functionality of both devices is described in the following.

2.3.1 X-ray tubes

This section discusses the functionality of x-ray tubes and the production of x-rays. X-rays belong to the electromagnetic spectrum and lie in the energy range of about 100 eV to 1 MeV. X-ray tubes can produce this kind of radiation. An x-ray tube consists of a vacuumed cylinder in which an anode and a cathode are installed. High voltage, called tube voltage U_{XRT}, is applied between the anode and the cathode. Typical values for the tube voltage are 10 kV up to 150 kV. A heating voltage U_{H} is applied to the cathode, which leads to thermal emission of electrons. These electrons are accelerated to the anode due to the applied tube voltage. Figure 2.3.1 shows a scheme of an x-ray tube. The kinetic energy of the accelerated electrons is $E_{\mathrm{kin}} = e \cdot U_{\mathrm{XRT}}$ when they reach the anode. The interaction of the electrons with the anode material produces x-rays as described in section 2.1.3. The two produced kinds of radiation are bremsstrahlung and characteristic radiation. bremsstrahlung produces continuous radiation, whereas the photons of characteristic radiation can only have certain energies which correspond to the energy transitions of the shell electrons of atoms. The characteristic radiation appears as distinct lines in the spectrum of an x-ray tube. The maximum energy of the produced x-rays depends on the applied high voltage between the cathode and the anode. Figure 2.3.2 shows a simulated spectrum of an x-ray tube with a tungsten anode at a tube voltage of 120 kV. The simulation is performed with [Boo]. For a high voltage of 120 kV, the accelerated electrons have a kinetic energy of 120 keV when they reach the anode. Therefore, the maximum energy of the x-rays photons is 120 keV in case

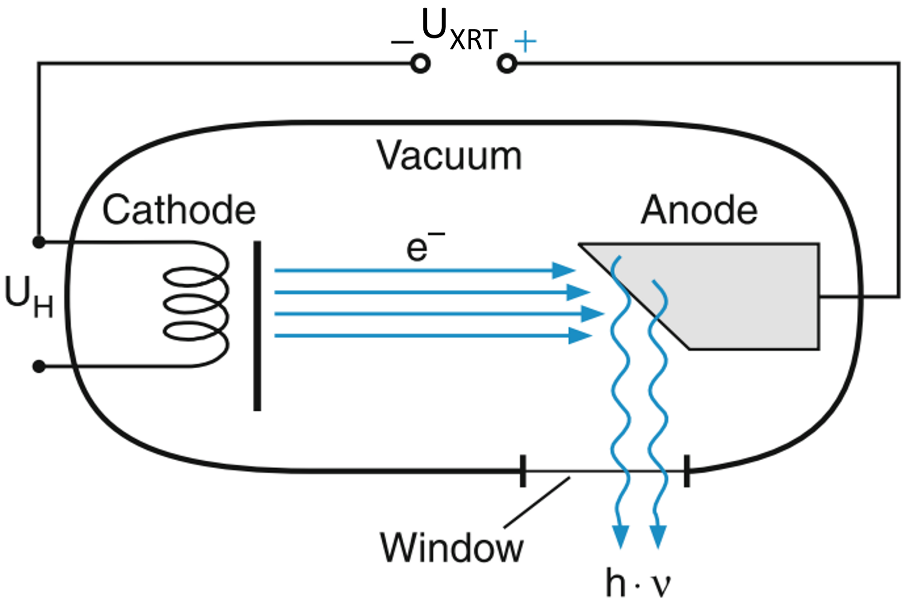

Figure 2.3.1: Scheme of an x-ray tube. By a heating voltage U_{H}, electrons are emitted from the cathode and accelerated towards the anode by a high voltage U_{XRT}. The electrons interact with the anode material, which produces x-rays. These leave the x-ray tube through an exit window. The figure is taken from [Dem18, edited].

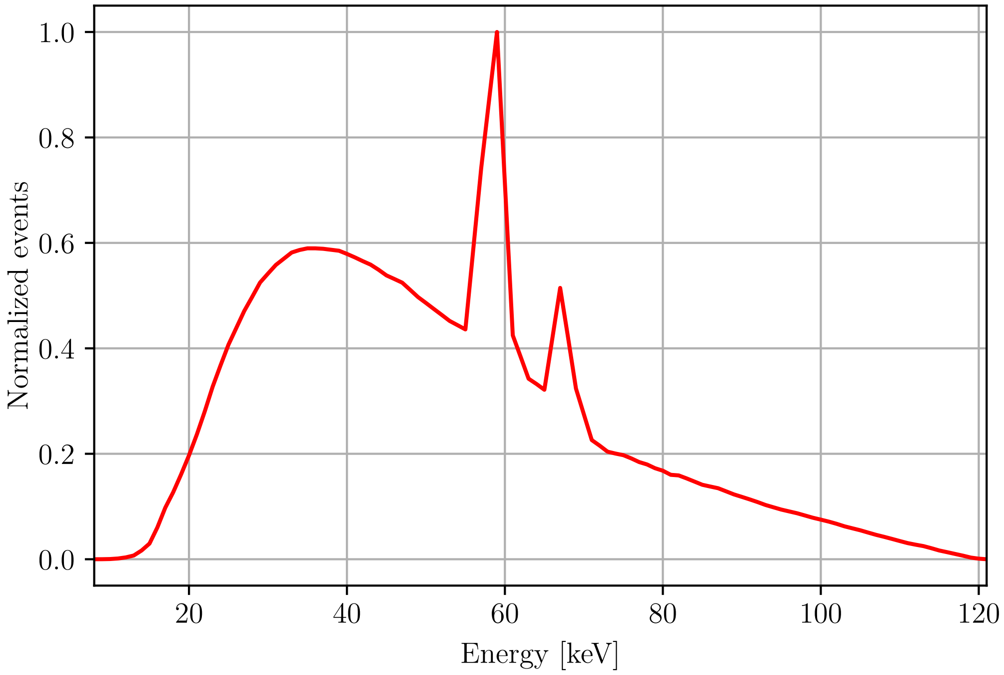

Figure 2.3.2: Simulated spectrum of an x-ray tube with a tube voltage of 120 kV. The number of events are normalized to the largest value. No filters were applied. The continuous spectrum results from bremsstrahlung, whereas the discrete lines result from the characteristic radiation. Data is taken from [Boo].

the total kinetic energy of an electron is emitted as a photon in the process of bremsstrahlung. [Dem18]

2.3.2 Linear particle accelerator

Measurements with clinical electrons are performed in this thesis. They are accelerated by a linear particle accelerator (LINAC). The setup of a clinical LINAC is shown in figure 2.3.3. The most important part of the modulator (Mo) is the source for the production of microwaves which are transported to the accelerator pipe (B) via the high-frequency transport system (HF). In the accelerator pipe, the electron gun (K) is positioned at one end of the pipe. It consists of a cathode and an anode. In the cathode, free electrons are produced by thermal emission. They are accelerated via a voltage applied between the cathode and the anode. Behind the anode, the acceleration of the electrons via microwaves starts. There are two possible types of acceleration which are explained in the following. [Kri18][SKJ18]

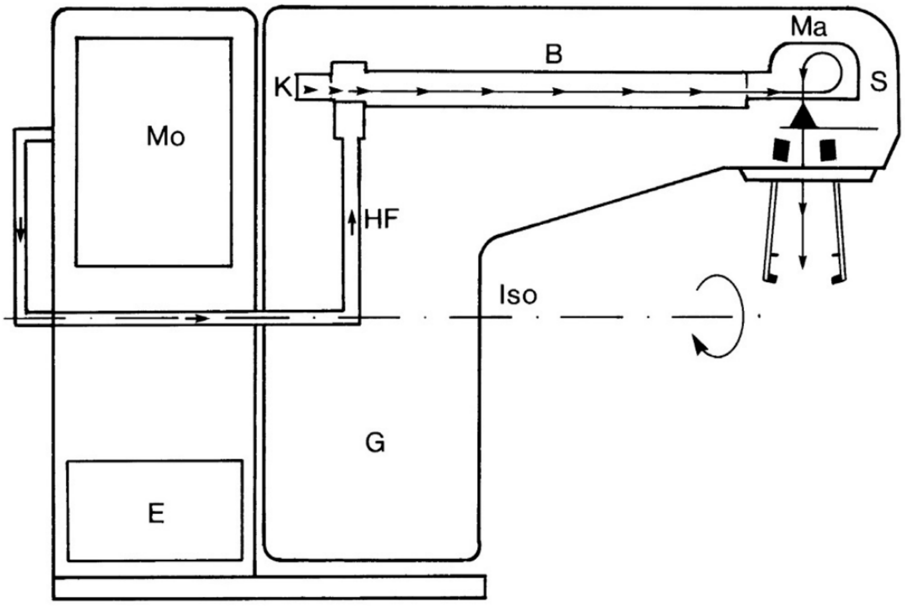

Figure 2.3.3: Setup of a clinical LINAC. Mo is the modulator, E is the energy supply, HF is the high-frequency transport system, K is the electron canon, B is the accelerator pipe, Ma is the deflection magnets, S is the radiator head, Iso is the isocentre axis and G the Gantry. The picture is taken from [Kri18].

Traveling waves

For the technique of traveling waves, the accelerator pipe is divided into small resonators with a length of 2.5 cm at a microwave frequency of 3 GHz. The length of the resonators must be one-fourth of the wavelength of the microwaves to fulfill the resonance condition. The segments between the resonators act as pinholes. The phase velocity of the microwaves depends on the pinholes' diameters. Directly behind the electron gun, the phase velocity of the microwaves must be relatively small since the inserted electrons have a small velocity there. In further segments, the phase velocity of the micro waves becomes larger because of the construction, leading to the acceleration of electrons. Those positioned right before the maxima of the microwaves are accelerated continuously throughout the accelerator pipe because they travel with the microwaves. Electrons traveling in front of the maximum are exposed to a smaller electric field which causes them to experience a smaller acceleration. Electrons behind experience larger accelerations. This leads to the production of electron bundles. This process is called phase focusing. Therefore, electron radiation is not continuous, but pulsed. [Kri18][SKJ18]

Standing waves

The main difference between the technique of traveling waves to the one of standing waves is that the microwave is reflected at the end of the accelerator pipe, which causes the incoming and the reflected wave to interfere. The geometry is chosen such that this leads to standing waves, i.e. the maxima and knots of the wave remain at the same position. The amplitudes of the waves are opposite in two neighboring resonators. Electrons experience acceleration at negative amplitudes. They are accelerated into the next resonator, where a positive amplitude was present in the process of acceleration of the electrons in the previous resonator. The time of flight of the electrons and the oscillation time are set to be identical. This leads to a negative wave amplitude in the next resonator, which causes the electron to accelerate again. So, electrons experience acceleration throughout the whole accelerator pipe. [Kri18][SKJ18]

The accelerator pipe is positioned in the arm of the gantry. The electron beam is deflected in the radiator head. Additionally, a scatter foil system is installed for the operation with electrons. Apertures are used for shaping the beam. In principle, it is also possible to produce photons with a LINAC via irradiation of a tungsten plate with the accelerated electrons. They interact with the material as described in section 2.1.3. Because of the high electron energy, bremsstrahlung is produced mainly in forward direction. Flattening filters are used in order to achieve a homogeneous radiation field. However, only electron radiation from LINACs is used in this thesis. [Kri18][SKJ18]

2.4 Dosimetric quantities

Dosepix is designed for dosimetric tasks. In this chapter, the most important dosimetric quantities are introduced. The descriptions are based on [Kri17] and [SKJ18].

Absorbed dose

The most important dosimetric quantity for this thesis is the absorbed dose D. It is defined as the absorbed energy dE_{abs} divided by the mass dm of the irradiated volume element dV of the material with density ρ:

$$D = \frac{dE_{\text{abs}}}{dm} = \frac{1}{\rho}\frac{dE_{\text{abs}}}{dV} \tag{2.4.1}$$

The unit of the absorbed dose is Gray (Gy), defined as Joule divided by kilogram. The absorbed dose depends on the irradiated material, so for declarations about the absorbed dose, the irradiated material must be known. [Kri17][SKJ18]

Ion dose

The ion dose J is the produced charge of the same sign dQ per air mass unit dm_{air}:

$$J = \frac{dQ}{dm_{\text{air}}} = \frac{1}{\rho}\frac{dQ}{dV} \tag{2.4.2}$$

The unit of the ion dose is Coulomb divided by kilogram. [Kri17][SKJ18]

Kerma

Kerma K is the abbreviation for kinetic energy released per unit mass. It describes the kinetic energy dE_{kin} transferred to secondary charged particles in matter divided by the mass unit of the irradiated material:

$$K = \frac{dE_{\text{kin}}}{dm} = \frac{1}{\rho}\frac{dE_{\text{kin}}}{dV} \tag{2.4.3}$$

The unit of kerma is Gray. As for the absorbed dose, the kerma depends on the irradiated material. [Kri17][SKJ18]

Equivalent dose

The effect of radiation depends on the particle type and the irradiated tissue. Therefore, additional quantities are necessary to take these effects into account. The equivalent dose H is defined as the product of the absorbed dose and a quality factor Q:

$$H = Q \cdot D \tag{2.4.4}$$

The quality factor depends on the respective particle type. For light particles like photons and electrons, the quality factor is 1. However, for alpha particles, the quality factor is 20.

When multiple types of particles are used, the equivalent dose is described by the sum of the equivalent doses of the single types of particles:

$$H = \sum_i Q_i \cdot D_i \tag{2.4.5}$$

The unit of the equivalent dose is Sievert which is defined, like the unit Gray, as Joule divided by kilogram. [Kri17][SKJ18]

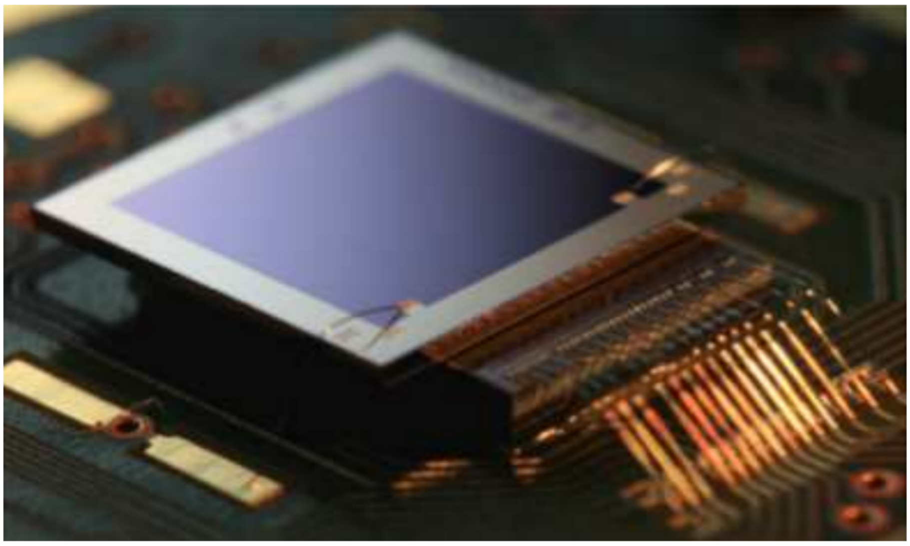

Figure 2.5.1: An image of the Dosepix detector. The picture is taken from [Gab12].

2.5 The Dosepix detector

The Dosepix detector is used for all measurements in this thesis. Dosepix is a hybrid pixelated photon-counting energy-resolving x-ray detector. It is mainly used for dosimetry of photon radiation. However, other kinds of radiation are used in this thesis, too. CERN ([CER]) designed Dosepix in cooperation with ECAP and IBA dosimetry ([IBA]). Figure 2.5.1 shows an image of Dosepix. It is a hybrid detector, meaning that the application-specific integrated circuit (ASIC) and the sensor are produced separately. This allows the attachment of different kinds of sensors to the ASIC. In this thesis, a 300 µm thick p-in-n-doped silicon sensor is used, except for chapter 5 where no sensor is attached to the ASIC. If a particle impinges on the sensor, it interacts with the sensor material as described in section 2.1. These interactions lead to ionized atoms and free electrons. The free electrons also ionize atoms which results in the production of electron-hole pairs. The required energy for this process is 3.62 eV in silicon ([Kno00]). A bias voltage is applied between the sensor's upper side and the ASIC's electrodes. The produced electric field accelerates the charge carriers. For the three-detector-setup, which is a setup, where three detector can be used simultaneously with one read-out board, the default bias voltage is 100 V. For the single-detector-setup, where only one detector is connected to a read-out board, the default bias voltage is 48 V. In the standard operation mode, the holes are accelerated towards the electrodes of the ASIC, where the charge signal is further processed. The amount of charge carriers is proportional to the deposited energy. Figure 2.5.2 shows the setup of a hybrid pixel detector. The sensor is connected to the ASIC via bump bonds. The Dosepix ASIC is divided into 16 x 16 pixels with a pixel pitch of 220 µm. The sensor also has 16 x 16 pixels, which are divided into large and small pixels. The first two and the last two rows are small pixels with a size of 55 µm x 55 µm, which means that there are gaps between the pixels, where no events are detected. The other 12 x 16 pixels in between have a size of 220 µm x 220 µm. The detection area has a size of 3.52 mm x 3.52 mm. The small pixels are used for high flux radiation since the detected event rate is smaller for a smaller pixel size. A separate readout electronics exists for each pixel. The readout is performed column-wise, which means that the readout is performed at once for 4 small pixels and 12 large pixels. Therefore, no dead-time exists for Dosepix, since always 15 of the 16 pixel-columns measure simultaneously. [Won12]

2.5.1 Signal processing

Figure 2.5.3 shows a block diagram of the pixel electronics for signal processing. A charge-sensitive preamplifier amplifies the charge signal from the sensor. Its output is compared to a threshold voltage via a discriminator. Figure 2.5.4 shows the signal from the charge-sensitive amplifier and the threshold voltage. Every measured event produces a pulse with an amplitude proportional to the deposited energy in the sensor. The preamplified charge signal is decreased by a current proportional to I_{krum}, which is handed over to Dosepix from the outside. I_{krum} also compensates leakage current. The discriminator outputs a high signal if a particle deposits energy in the sensor and the preamplified charge signal exceeds the threshold voltage. The time over threshold (ToT) is measured via a reference clock with a frequency of 100 MHz. The ToT counter counts the clock cycles in

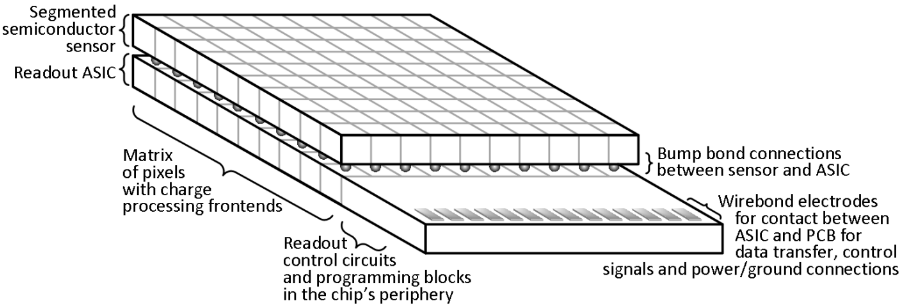

Figure 2.5.2: Setup of a hybrid pixel detector. The sensor is connected to the ASIC via bump bonds pixel-wisely. The ASIC can be connected to a printed circuit board (PCB) for data transfer via wirebond electrodes. The picture is taken from [Won12].

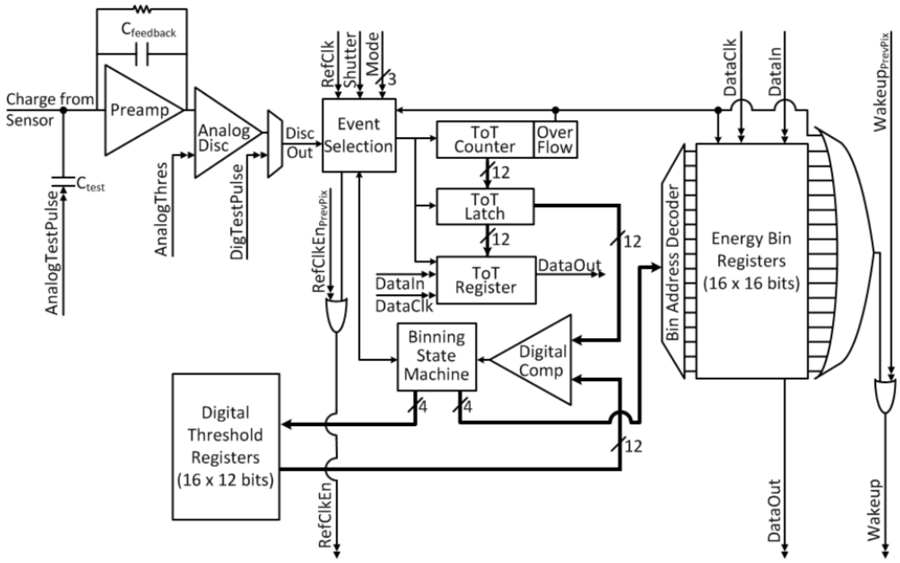

Figure 2.5.3: Block diagram of the pixel electronics of Dosepix. The picture is taken from [Won12].

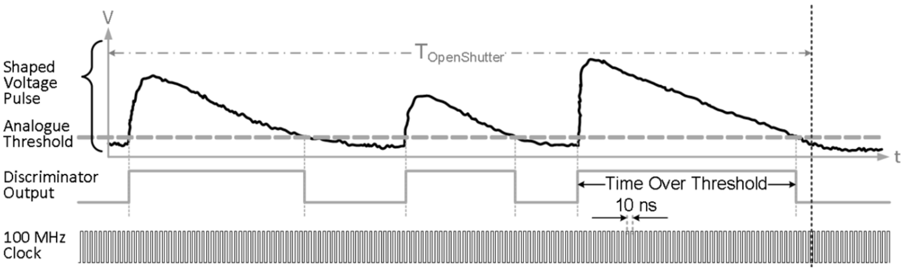

Figure 2.5.4: Signal processing of charge signals in a pixel. The preamplified charge signal is compared to a threshold voltage by a discriminator. The time of the signal exceeding the threshold is measured via a reference clock. This time over threshold encodes the information about the deposited energy. The picture is taken from [Won12].

discrete values while the preamplified charge signal exceeds the threshold voltage. One clock cycle has a duration of 10 ns. The deposited energy in the sensor can be determined by the ToT value. This requires an energy calibration which is described in section 4.2. The ToT value depends on the adjusted threshold voltage and I_{krum}. The threshold voltage is set above the noise level so that the preamplified charge signal only exceeds the threshold due to sufficient deposited energy in the sensor. However, also low energy events are not measured if the preamplified charge signal does not exceed the threshold voltage. If the threshold voltage is increased, the ToT value becomes smaller. The adjustment of the threshold voltage is further discussed in section 4.1. If I_{krum} is increased, the preamplified charge signal is decreased faster, which leads to smaller ToT values. This reduces pile-up. Pile-up means that an event is measured while the charge signal of the previous event still exceeds the threshold voltage. Therefore, multiple events are registered as one event with higher energy than the actual energy of the particles. By increasing I_{krum}, the probability of pile-up is reduced. A disadvantage of an increased I_{krum} is a worse energy resolution since one clock cycle covers a bigger energy range.
Another important effect is charge sharing. The electron-hole pairs that are created in the sensor form a charge cloud. This charge cloud diffuses with time because of repulsion of the charged particles, which leads to a spread of its radius. This leads to a probability that the signal is not detected by a single pixel but by multiple ones. Therefore, one event is detected as multiple ones with less energy than the actual deposited energy. The probability of charge sharing depends on the spot of interaction in the sensor and the applied bias voltage. The probability for charge sharing increases for interactions with a large distance from the ASIC and small bias voltages because the duration for the charge cloud to reach the ASIC is larger. [MPS+02][KDM+17][Dur08][Sch21]

2.5.2 Operation modes

Dosepix is operated in several modes: ToT-mode, Integration-mode, Dosi-mode, and photon-counting mode. These are described in the following. The description is based on [Won12].

ToT-mode

In ToT-mode, the clock cycles of each preamplified charge signal exceeding the threshold voltage are counted as already described in section 2.5.1. The latest ToT values in each pixel are stored in the ToT register. The previous ToT value is overwritten in this mode when a new event is detected. The number of events depends on the readout speed. For the three-detector-setup, the readout speed is approximate 10 Hz, and for the single-detector-setup, the readout speed can reach a readout speed of about 300 Hz. So, from the ToT-mode, no conclusions can be drawn on the total events or dose. However, the ToT-mode measures exact ToT values, which makes it suitable for measuring energy deposition spectra and for energy calibration. [Won12]

Integration-mode

In Integration-mode, all measured ToT values of a pixel within one frame are summed up. Therefore, the integrated deposited energy in units of ToT can be measured with this mode. [Won12]

Dosi-mode

Dosi-mode, also called energy-binning mode, is suitable for dosimetry. Here, the ToT values are measured and sorted into a 16-channel histogram via a binning state machine. This histogram has 16 bins, where the bin edges can be adjusted. The bin edges are stored in the digital threshold register and can be set from the outside. The registered ToT values are compared to the provided bin edges via a digital comparator. The registered event is stored in the corresponding energy bin by the binning-state-machine incrementing the respective counter. These histograms can be read out. It contains the number of events that are registered in the corresponding energy bins. The readout is performed column-wise, as already described. So, no dead-time occurs for Dosepix. [Won12]

Photon counting mode

No information about the deposited energy is saved in photon-counting mode, but only the number of registered events. This mode is used for the threshold equalization, which is described in chapter 4.1. [Won12]

2.6 Semiconductors

The bias voltage, which is responsible for the electric field between the electrodes of the ASIC and the upper side of the sensor, is varied in this thesis. Therefore, theoretical background about semiconductors is necessary to understand their functionality. The sensor of Dosepix, which consists of silicon in this thesis, is a semiconductor. For the electric properties of semiconductors, the number of valence electrons of the materials' atoms is essential. Silicon atoms have four valence electrons. A p-doped and an n-doped layer exist within the sensor material. This is done by inserting atoms with three valence electrons in case of p-doping and atoms with five valence electrons in case of n-doping. So, p-doping results

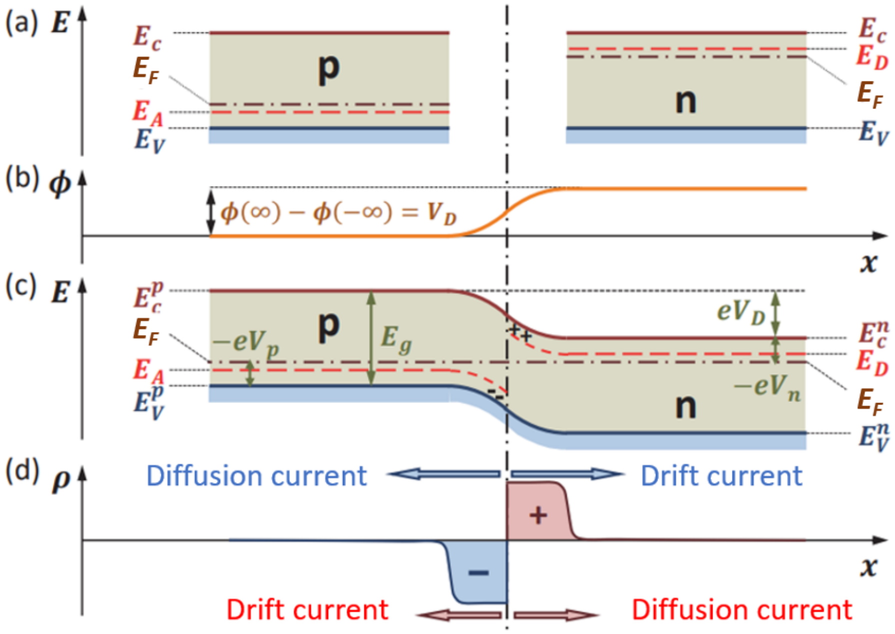

Figure 2.6.1: Scheme of the band structure in semiconductors. In (a), the band structure of n-doped and p-doped material is shown. In p-doped material, the acceptor energy E_A lies above the valence energy E_V. In p-doped material, the donator energy lies beneath the conductor band E_C. (b) shows the course of the potential. In (c), the band structure for a pn-junction is shown. (d) shows the course of the charge density. The picture is taken from [GM18].

in an excess of holes, whereas n-doping leads to an excess of electrons. Multiple important energies exist in the band scheme. The valence energy E_V describes the maximum energy electrons in a semiconductor can have at a temperature of 0 K. The electrons in the valence band are essential for the chemical binding of the material. At room temperature, the valence band is the most energetic band fully occupied by electrons. The conduction band is the next higher energetic band. The maximum energy electrons can have without excitation is called the Fermi level. Due to doping, two additional energy levels exist, the acceptor- and donator levels. For n-doping, the atoms with five valence electrons cannot bind to another electron. Therefore, less energy is required to release these electrons from their atom and lift them to the conduction band. On the other hand, for p-doping, an electron is missing because of the atoms with three electrons. Therefore, only small energies are required to lift electrons from the valence band into the acceptor band, which leaves behind a hole in the valence band. A graphical illustration of the band structure for n-doped and p-doped material is shown in figure 2.6.1.

A pn-junction is produced by bringing a p-doped and an n-doped material in

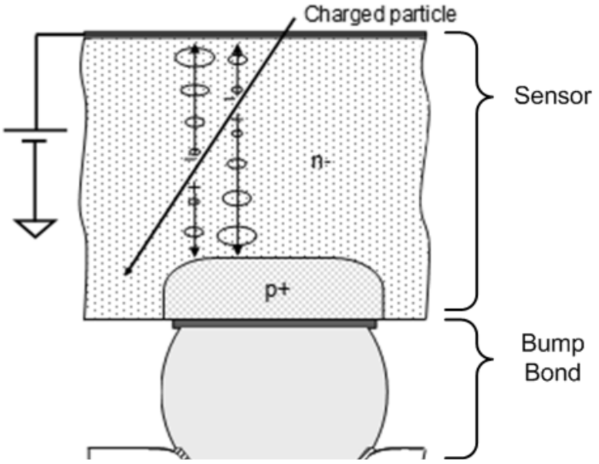

Figure 2.6.2: Illustration of the pn-junction in the sensor of Dosepix. Holes produced by ionizing radiation are accelerated towards the p-doped silicon, which is connected to a bump bond. The figure is taken from [Won12].

contact. The Fermi level remains on the same level for the whole junction. This leads to bending of the introduced bands and the collection of charge carriers at the junction. This is shown in figure 2.6.1(c). The charge carrier zone is also called depletion zone, which is the sensitive part of a semiconductor detector. A diffusion current is produced because of the different types of charge carriers in the p-doped and n-doped layers. The electrons of the n-doped layer diffuse into the p-doped layer, and the holes of the p-doped layer diffuse into the n-doped layer. This is shown in figure 2.6.1(d). At the border region of the n-doped and p-doped layer, a positive charge density forms at the side of the n-doped layer and a negative charge density at the side of the p-doped layer. Because of the opposing charge densities, a drift current is produced, which is in opposition to the diffusion current. The drift current can also be derived from the diffusion voltage V_{D}, which is the difference between the potential in the p-doped material and the n-doped material at a sufficient distance to the junction. This is shown in figure 2.6.1(b). For Dosepix, the p-doped material is embedded into the n-doped silicon as illustrated in figure 2.6.2. The p-doped parts are connected to the bump bonds.

A voltage can be applied between the p-doped layer and the n-doped layer. The thickness of the depletion zone depends on the applied voltage. The voltage is applied in blocking direction in case of semiconductor detectors, which means that the positive pole is applied to the n-doped layer. This increases the charge densities even more on both sides, resulting in an increased depletion zone thickness. The depletion zone is the sensitive part of the detector. If a particle impinges on the sensor, it interacts via the described interactions from section 2.1. If the particle deposits energy in the depletion zone, the positive charge carriers drift to the electrodes of the ASIC and produce a signal. In comparison, if a particle deposits energy in the n-doped layer or p-doped layer, respectively, the charge carriers recombine and cannot be detected. A reduction of the bias voltage and, therefore, of the thickness of the depletion zone results in a reduced event rate. The threshold voltage of a pn-junction in silicon is approximately 0.7 V. [GM18][KW16][IL08]

3 UHDpulse project

Contents

The primary cancer treatment is radiation therapy. The main challenge in cancer treatment is destroying cancer cells and, simultaneously, minimizing damage to the healthy surrounding tissue. There are a few techniques already existing, such as image-guided radiotherapy (IGRT). Imaging of the tumor is contemporaneously used to its irradiation ensuring a minimized exposure of healthy tissue. Another technique to reduce healthy tissue complications is ion therapy, with, e.g., carbon ions. The advantage of heavy particles compared to photons and electrons is reduced lateral spread of the radiation because of smaller scattering angle occurrence due to their high masses. This allows a more precise treatment in comparison to electron and photon radiation. Another positive effect is the different kind of interaction of heavy charged particles compared to photons and electrons, resulting in the Bragg peak at the stoppage of the particles as seen in section 2.1.3. The Bragg peak is positioned at the tumor's position by adapting the particles energy, leading to a high dose in the tumor region and a small dose in the surrounding healthy tissue. Disadvantages that still arise in new kinds of treatments are, on the one hand, the cost of new treatment systems and, on the other hand, side effects, especially for sensitive regions like the brain. Also, skin reactions such as fibronectrotic lesions, i.e. scar tissue restrict treatment via radiotherapy potentially causing treatment interruptions [SKJ18][SHF$^+$20].

A rather new cancer treatment technique is FLASH radiotherapy. It is based on the so called FLASH effect where high dose rates in the order of several Gy/s with small treatment durations are applied. This results in reduced radiation-induced toxicities of healthy tissue compared to common radiation therapy, which was already observed in the 1960s [BHF$^+$14]. The cell survival rate of tumor cells is nearly equivalent to conventional radiotherapy. The FLASH effect is illustrated in figure 3.0.1. It shows the probability of tumor control corresponding to cell de-

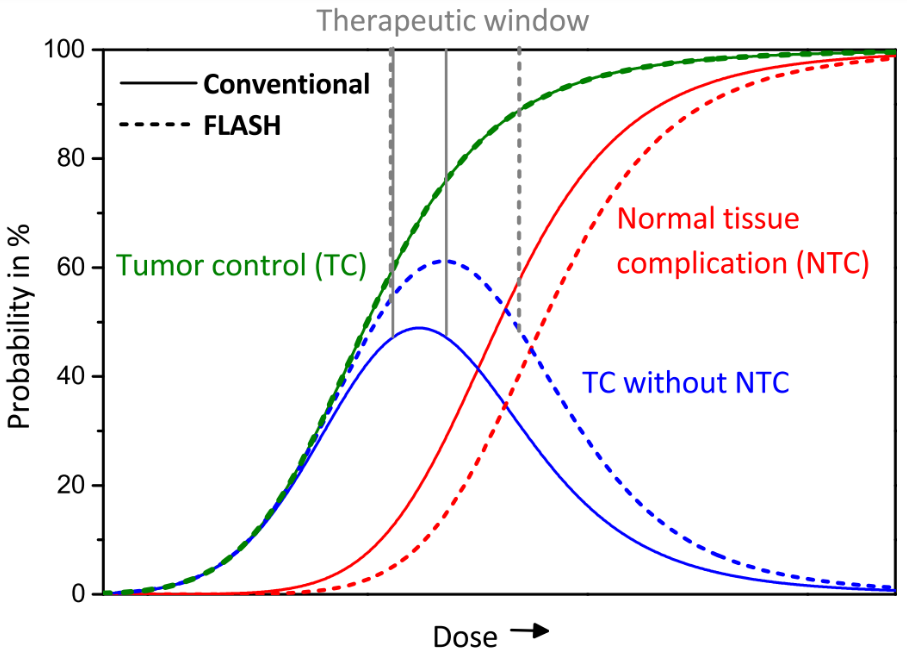

Figure 3.0.1: Comparison of the probability of tumor control and normal tissue complication between conventional and FLASH radiotherapy as a function of the dose. Normal tissue complication has a small probability for FLASH therapy with identical tumor control to conventional radiotherapy. Therefore, tumor control without normal tissue complication is higher, leading to a bigger therapeutic window. The figure is taken from [SHF+20].

struction of tumor cells, and normal tissue complication in dependence on the dose for conventional and FLASH radiotherapy. Because of the reduced normal tissue complication, the probability of tumor control without normal tissue complication is bigger, meaning that larger doses are applicable. The therapeutic window, i.e. the range of treatment with respect to dose, is increased. The FLASH effect has been observed for electrons, photons and protons. Most pre-clinical investigations were performed with electrons up to 20 MeV. However, these electrons are only suitable for superficial or shallow tumors. Very high energy electrons (VHEE) with energies above 100 MeV could be used for deep-seated tumors. For such high energies, laser-driven electron accelerators are used. With these radiation systems, dose rates in the range of 10^9 Gy/s up to 10^{12} Gy/s can be achieved [SHF+20].

For these three types of radiation techniques, FLASH radiotherapy, VHEE and laser-driven beams, metrological challenges arise because of significantly higher dose rates compared to conventional radiotherapy. Figure 3.0.2 illustrates the dose deliv-

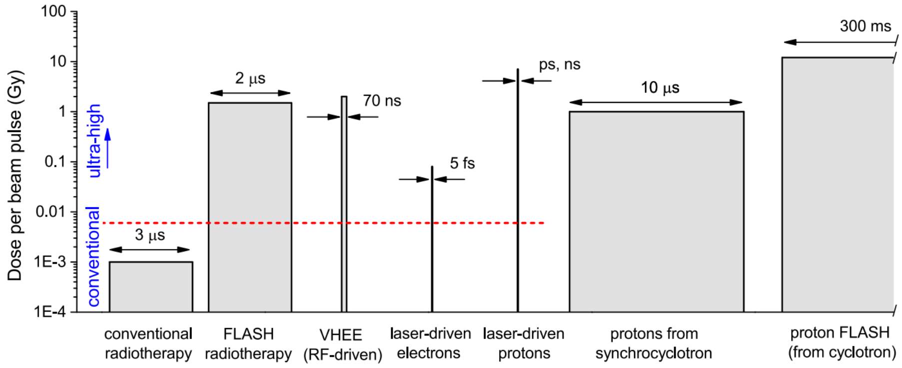

Figure 3.0.2: Illustration of dose per beam pulse and pulse duration for different radiation techniques. The red line indicates the upper limit of the start of deviation of an Advanced Markus chamber. The figure is taken from [SHF+20].

ered per beam pulse and the pulse duration for the different radiation techniques. Comparing the dose per beam pulse of conventional radiotherapy and FLASH radiotherapy, it is more than three magnitudes higher at FLASH radiotherapy at a comparable beam pulse duration. For VHEE accelerators, the dose per pulse is comparable to the one in FLASH radiotherapy, but the pulse duration is much shorter. The dose per beam pulse of laser-driven accelerators is 80 mGy. However, laser-driven accelerators can produce very small pulse durations of 5 fs, resulting in a much higher dose rate during the pulse than for VHEE accelerators. The pulse duration of proton radiation from cyclotrons is around 300 ms and therefore rather large compared to the other radiation techniques. However, novel synchrocyclotrons can reach a dose per beam pulse of 1 Gy at a pulse duration of 10 µs. Ionization chambers as active detectors start to fail at a certain dose per beam pulse. The red line in figure 3.0.2 indicates the upper limit of an Advanced Markus chamber. This is a small-sized plane-parallel ionization chamber with a sensitive volume of $0.02\,\mathrm{cm}^3$ and an electrode distance of 1 mm [PTW][SHF+20].

It is important to developed methods to measure the delivered dose before clinical treatments precisely. The project "Metrology for advanced radiotherapy using particle beams with ultra-high pulse dose rates" (UHDpulse, [UHD]) develops reference standards and validates the methods used to measure dose rates. It encompasses detector systems for radiation in the direct beam and stray radiation. The UHDpulse project is part of the European Metrology Programme for Innovation and Research (EMPIR, [EMP]) which coordinates research projects and enables collaboration between different organizations. The UHDpulse project started in September 2019. Figure 3.0.3 shows the participants of the UHDpulse project, which also includes the Erlangen Centre of Astroparticle Physics (ECAP) [SHF+20][UHD].

Figure 3.0.3: Participants of the UHDpulse project. The figure is taken from [UHD].

In 2016, a mini-pig was irradiated with electrons with FLASH dose rates as well as conventional dose rates in order to treat skin tumors. Different spots were irradiated with doses of 28 Gy, 31 Gy and 34 Gy. For FLASH radiotherapy, the used dose rate is 300 Gy/s whereas for the conventional radiotherapy 5 Gy/min are used. Figure 3.0.4 shows the effect of conventional and FLASH radiotherapy on skin tumor at two points in time after the treatment. Application of FLASH radiotherapy results in a quasi normal morphology after 36 weeks, whereas severe fibronectrotic lesions, i.e. scar tissue, are observed for the conventional approach. Figure 3.0.4(b) shows the skin after 3 years. Again, significantly better results are observed for the FLASH approach. It shows slight hyperkeratosis, i.e. thickening of the skin, and depilation, i.e. reduction of hair growth, while treatment via conventional radiotherapy still leaves contracted and fibrotic skin tissue [VFP+19][SHF+20].

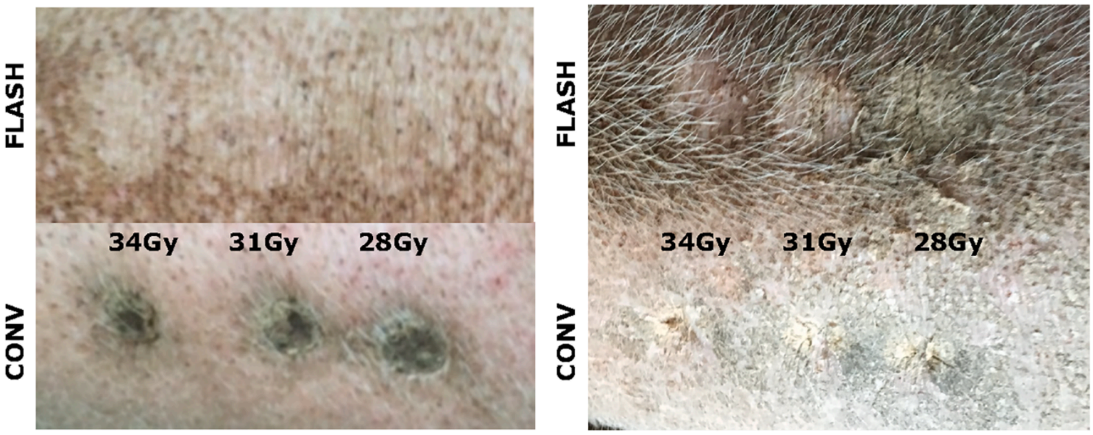

(a) 36 weeks post radiation

(b) 3 years post radiation

Figure 3.0.4: Illustration of the skin of a mini-pig irradiated with FLASH dose rates (upper panel) of 300 Gy/s and conventional dose rates (lower panel) of 5 Gy/min (a) 36 weeks and (b) 3 years after the irradiation. The skin irradiated with conventional dose rates shows fibronectrotic lesions, i.e. scar tissue, after 36 weeks and contraction and fibrosis after three years, whereas the skin irradiated with FLASH dose rates shows quasi-normal appearance and only slight hyperkeratosis, i.e. thickening of the skin and depilation, i.e. reduction of hair growth, after three years. The images are taken from [SHF+20].

3.1 Work packages

The UHDpulse project is separated into four work packages illustrated in figure 3.1.1. Work package 1 (WP1) covers the primary standards which are used as reference systems for dose measurements. It is led by the National Physical Laboratory (NPL, [NPL]). The main task of WP1 is the establishment of systems which are able to determine the dose of high-dose pulse rate beams. They are used to calibrate secondary standards which are systems that ensure correct dose applications in clinical treatments. Since these secondary standard cannot measure the absorbed dose directly, they have to be calibrated by primary standards. Another task is the establishment of reference radiation fields for electron beams allowing calibrations for FLASH radiotherapy with electrons. A suitable reference radiation field, for which the reference dose can be determined, must be provided. This is done by the determination of a spectrum specific factor from which the reference dose can be calculated ([BR08]).
Work package 2 (WP2) covers the secondary standards and reference methods for relative dosimetry. It is led by Eidgenössische Institut für Metrologie (METAS,

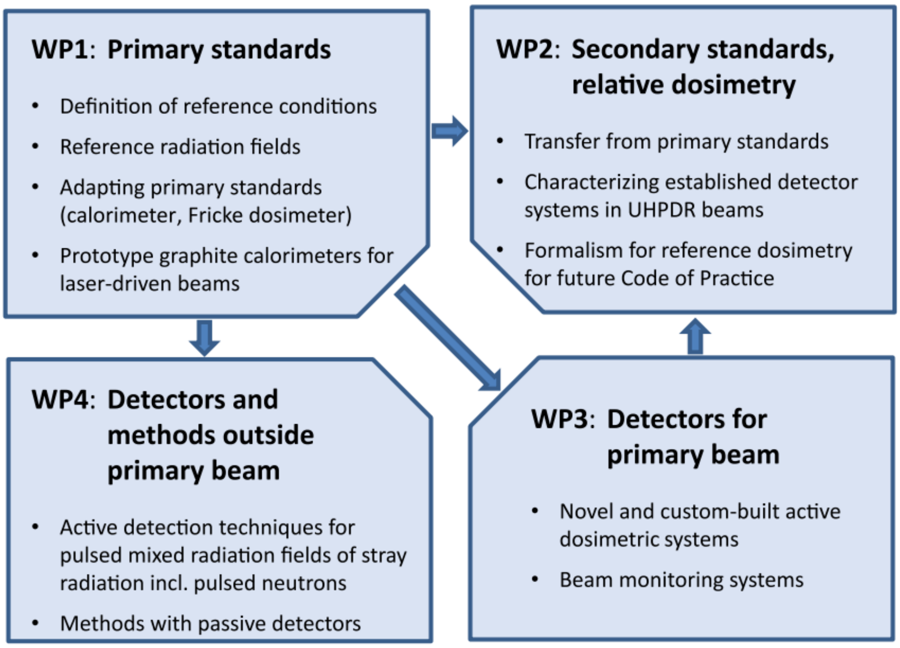

Figure 3.1.1: Work packages of the UHDpulse project. WP1 deals with the establishment of primary standards which can measure the dose without requirement of calibration systems. WP2 works on investigations of secondary standards which are used for dose determination in clinics. These systems need to be calibrated by use of primary standard systems. WP3 deals with the establishment of detectors for measurements in the primary particle beam. Suitable detectors can act as secondary standards. WP4 investigates the usage of detectors outside the primary particle beam for. The figure is taken from [SHF$^+$20].

[MET]). The task of WP2 is the transfer of dosimetry into clinical beam accelerators. The results from WP1 are used to implement the primary standard into the reference dosimetry for the corresponding accelerators. Measurement systems are tested on suitability for secondary standards, for FLASH radiotherapy with electrons and characterized for clinical use. Additionally, metrological frameworks are created to develop working protocols for FLASH radiotherapy in clinics.
Work package 3 (WP3) deals with detector systems for the primary beam. It is led by Centre hospitalier universitaire vaudois (CHUV, [CHU]). WP3 focuses on evaluating absolute and relative dosimeters suitable for clinical and laser-driven accelerators. Absolute dosimeters measure the dose without requirement of reference systems, whereas for relative dosimeters, a reference system is required for dose determination ([SKJ18]). Additionally, novel and custom-built detectors and beam monitoring systems are examined. Beam monitoring is essential because of the

high precision needed for radiotherapy ([Nes14]). Finally, the detector systems are compared to each other in terms of suitability for ultra-high dose particle beams. Work package 4 (WP4) covers detector systems for measurements outside the primary beams. It is led by ADVACAM ([ADV]). The main task of WP4 is the development of methods in order to characterize stray radiation outside of the particle beam. Active dosimeters which measure dose in real time, as well as passive dosimeters whose measurements have to be evaluated first, are investigated [SHF⁺20].

3.2 Challenges of ionization chambers

As seen in the previous section, suitable system for dose measurements are required. Common instruments for clinical reference dosimetry are ionization chambers [RSM$^+$20]. The functionality of ionization chambers is explained in section 2.2. However, dosimetry of ultra-high dose rate particle beams with ionization chambers is accompanied by challenges. The large amount of ionized particles, i.e. electrons and ions produced inside the sensitive volume of the ionization chambers, at ultra-high dose rate particle beams leads to recombination of these particles preventing their detection. Therefore, common ionization chambers are not suitable for accurate dosimetry of FLASH radiotherapy since recombination factors are required to determine the actual dose. The recombination was investigated in [MRL$^+$20],[RSM$^+$20] and [PKF$^+$20] for VHEE beams and in [BSH$^+$20], [KSB$^+$20] and [KPW$^+$21] for FLASH radiotherapy. The most important results are explained in the following.

In [BSH$^+$20], the response of the ionization chamber in dependence on the dose per pulse is investigated. Irradiation was performed with electrons with an energy of 24 MeV at up to 2.5 Gy per pulse. Additionally, an alanine dosimetry system is used. Alanine is an amino acid ([SKJ18]). Stable free radicals are produced in alanine due to irradiation which subsequently are detected via electron spin resonance. These are independent of the dose rate in the investigated range. However, these systems are passive dosimeters which do not provide real-time doses. Figure 3.2.1 shows measurements with an alanine system as well as ionization chamber data without recombination corrections at 300 V operating voltage. An Advanced Markus chamber was used. The alanine system shows a linear dependence on the charge per beam pulse, corresponding to the dose per pulse. In contrast, the Advanced Markus chamber provides under-response compared to passive dosimeters at high dose rates because of the recombination of ionized particles. The model by Petersson et al. ([PJG$^+$17]) was fitted to the data taken by the ionization chamber. Because of the linearity of the alanine system, it is a suitable candidate

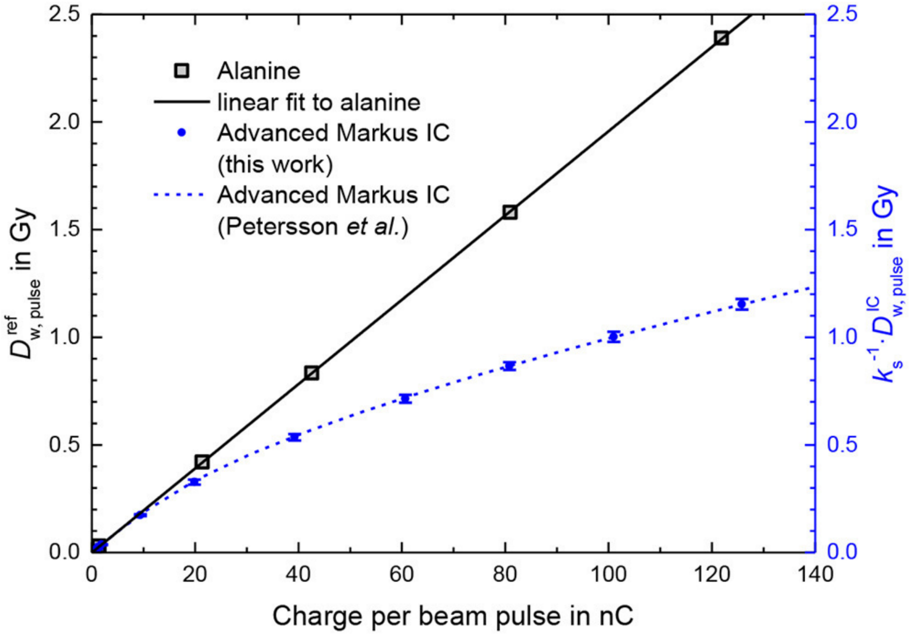

Figure 3.2.1: Dose per pulse measurements with an alanine dosimetry system (black) and an Advanced Markus chamber at an operation voltage of 300 V without recombination factors (blue) as a function of the charge per beam pulse. The ionization chamber provides smaller values than the actual dose because of recombination. The model by Petersson et al. ([PJG+17]) was fitted to the data measured with the ionization chamber. The figure is taken from [BSH+20].

for reference dosimetry allowing the calculation of the recombination factors for the ionization chamber. The recombination factors become bigger with dose per pulse, resulting in a domination of the recombination factors compared to the actual measurements in terms of uncertainty. This makes the ionization chamber not suitable for accurate dose measurements.

In [PKF+20], the efficiency of an Advanced Markus chamber in dependence on the dose per pulse is investigated with a laser-driven electron beam with an energy of 200 MeV. The efficiency is calculated by the ratio of the dose measured by the ionization chamber and the dose obtained by a reference system. The used system of reference is Gafchromic external beam therapy 3 (EBT3) films ([EBT]). The ionization chamber was placed in a water phantom with the dimensions of 30 cm x 30 cm x 10 cm at a water depth of 72 mm. The efficiency of the ionization chamber in dependence on the dose per pulse is illustrated in figure 3.2.2. The operating voltage is 400 V. The measurements were performed with different beam sizes of 3.5 mm and 7 mm, respectively. Moreover, the reference film system was placed once in front and once at the back of the probe holder. The efficiency cleary drops

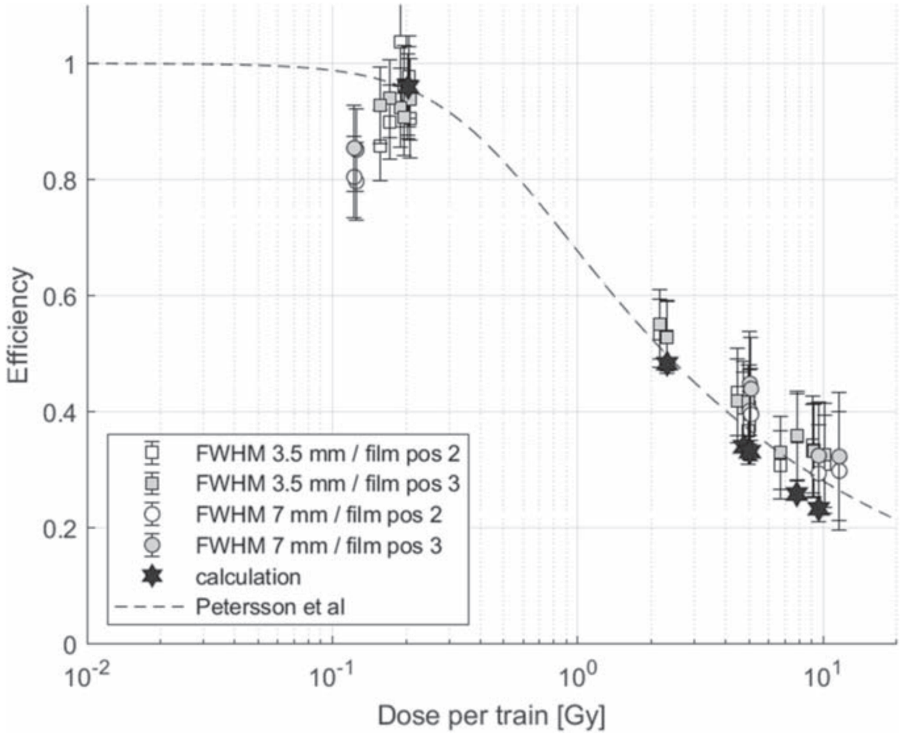

Figure 3.2.2: Efficiency of an Advanced Markus chamber as a function of the dose per pulse. Beam sizes of 3.5 mm and 7 mm were used. Additionally measurements with the film in front and behind the probe holder were performed. The efficiency decreases with increasing dose per pulse because of the recombination of charged particles. The model by Petersson et al. ([PJG+17]) was fitted to the measured data. The calculated values are slightly smaller than the measured ones. The figure is taken from [PKF+20].

to small values of about 30 % at approximately 10 Gy per pulse for all measurements. The calculated values are slightly smaller. The model by Petersson et al. ([PJG+17]) was fitted to the measured data. It is visible that the recombination decreases the efficiency of the Advanced Markus ionization chamber at high doses per pulse, making it unsuitable for dosimetry at ultra-high dose rates.

In [GGCF+22], an ultra-thin parallel plate ionization chamber (UTIC) with a small electrode distance of 0.27 mm is used. A smaller distance of the electrodes results in a larger electric field, increasing ionized particles' drift velocity and reducing recombination. The UTIC was operated at 250 V. The energy of the used electrons was 20 MeV. The chamber was positioned in a water phantom at the reference

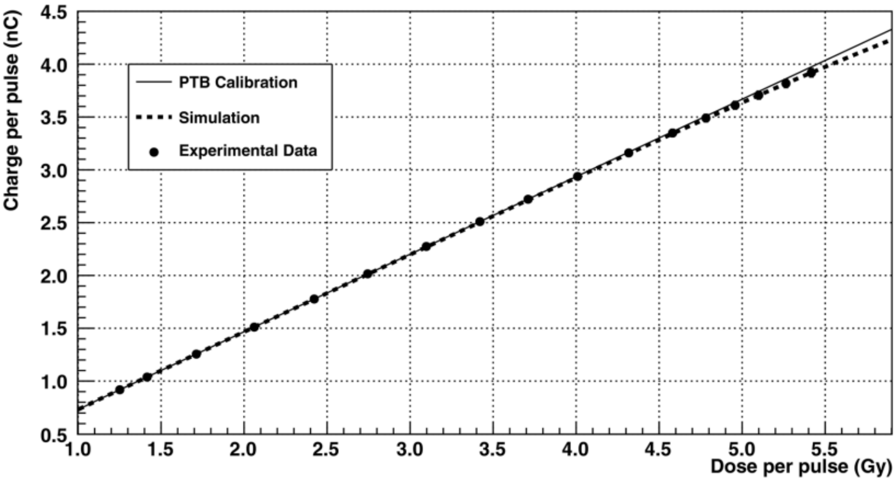

Figure 3.2.3: Charge per pulse measured by an ionization chamber with an electrode distance of 0.27 mm as a function of the dose per pulse. Small deviations are observed at high doses per pulse because of recombination. The figure is taken from [GGCF+22]

depth z_{ref}, which is given by ([KSB+20]):

$$z_{\text{ref}} = 0.6 \cdot R_{50} - 0.1 \tag{3.2.1}$$

Here, R_{50} is the depth in the water phantom in cm where the dose has dropped to 50%. The reference depth is also expressed in cm. Doses per pulse up until 5.4 Gy were used. Figure 3.2.3 shows the response of the UTIC in dependence on the dose per pulse. Recombination shows only a small effect for this ionization chamber at high doses per pulse. At 5.4 Gy per pulse, the recombination loss is 1.4%. Therefore, UTICs may be suitable for doses per pulse in the regarded range. However, the production of these small electrode distances is difficult. The intended distance of the UTIC in [GGCF+22] was 0.25 mm. This causes issues since small deviations in the distance of the electrodes have a huge effect on the measurement [GGCF+22].

3.3 Suitable systems for measuring ultra-high dose rates

Challenges arise for dosimetry at ultra-high dose rates with ionization chambers as discussed in the previous section resulting in the necessity of other systems. In [BSH+20], an aluminum calorimeter was investigated. Aluminum as an absorber material was chosen because of its homogenous form in contrast to graphite, which is the most commonly used material in calorimeters [BSH+20]. The dose is determined by measuring the radiation-induced temperature rise. The temperature rise is determined directly, making this aluminum calorimeter a real-time dosimeter. The calorimeter was irradiated with 50 MeV electrons at a distance of 0.9 m from the beam exit window. The investigated charge pulse is 5 nC to 45 nC per pulse which corresponds to a dose range of 0.3 Gy to 1.8 Gy per pulse. Figure 3.3.1 shows the measured data presented in [BSH+20]. Linearity is observed between the delivered charge per pulse and the measured dose. Therefore, the aluminum calorimeter is suitable in the investigated range and can deal as a real-time dosimetry system for ultra-high dose rates.

In [MFG+22],[KSB+22] and [RFG+22], the response of a diamond detector on ultra-high dose rate beams was investigated. The sensitive volume of this detector is an intrinsic diamond layer with a thickness of about 1 µm, which is positioned on top of a p-doped layer. A metallic contact between the intrinsic layer and a triaxial cable makes the detector a Schottky-diode. In [RFG+22], measurements with a

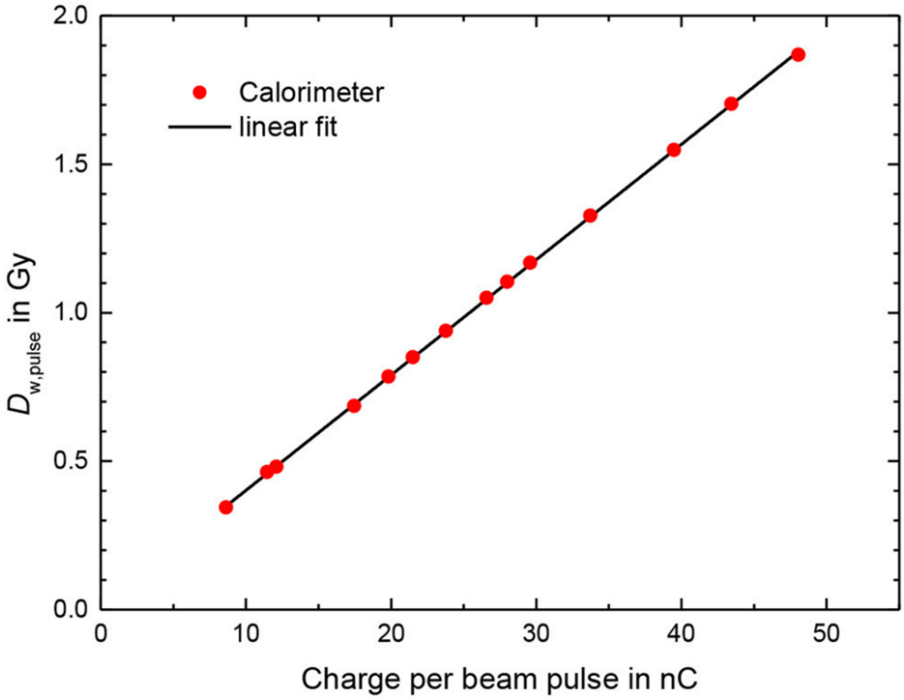

Figure 3.3.1: Illustration of the measured dose of an aluminum calorimeter as a function of the charge per beam. Linearity is observed, making the calorimeter suitable for dosimetry in the investigated range. The figure is taken from [BSH+20].

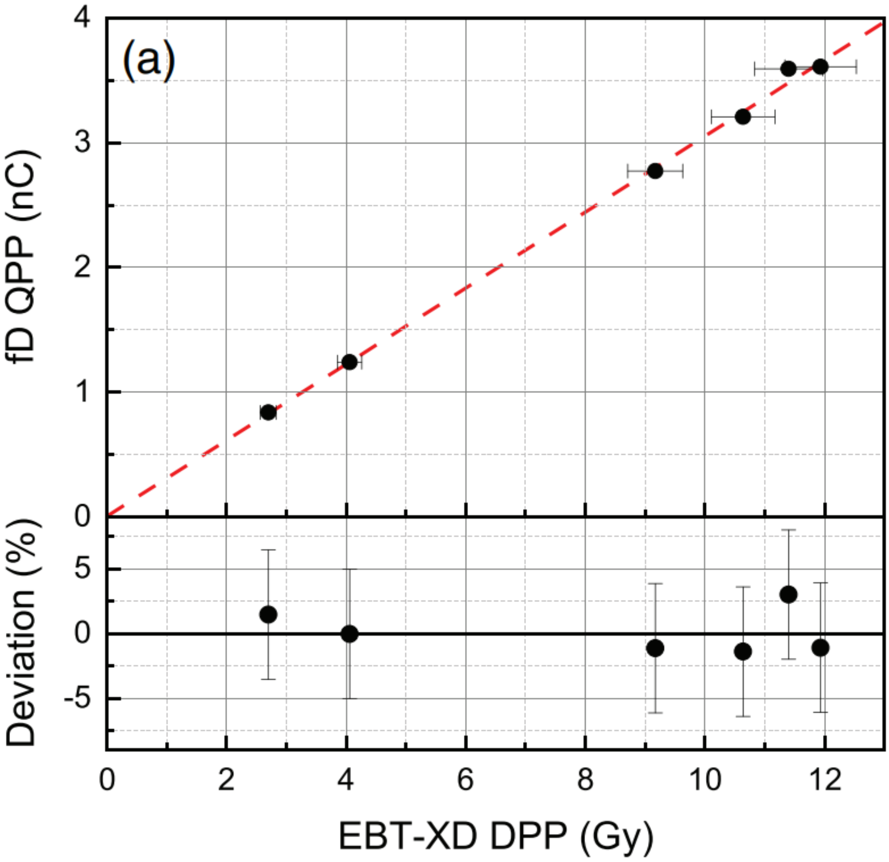

Figure 3.3.2: Charge per pulse (QPP) measured by a diamond detector as a function of the dose per pulse (DPP). Linearity is observed. The deviation shown in the lower panel of the figure lies in the range of ±5%. The figure is taken from [RFG+22].

diamond detector were performed with 9 MeV electrons inside of a water phantom at the water depth of maximal dose. Dose rates up until 11.9 Gy per pulse were used. Figure 3.3.2 shows the response of the diamond detector in dependence on the dose per pulse and the deviation from a linear fit. Linearity of the response in dependence on the dose per pulse is observed. The deviation lies in the range of ±5%, which was explained by uncertainties of EBT-XD films that were used for the calibration or fluctuations of the accelerator output. This result shows the suitability of diamond detectors for ultra-high dose rate beams.

Measurements of the stray radiation of ultra-high dose rate beams were performed in [OBP+22] with a Timepix3 detector. The Timepix3 detector is a hybrid pixel detector. In [OBP+22], two different sensors were utilized with 100 µm and 500 µm

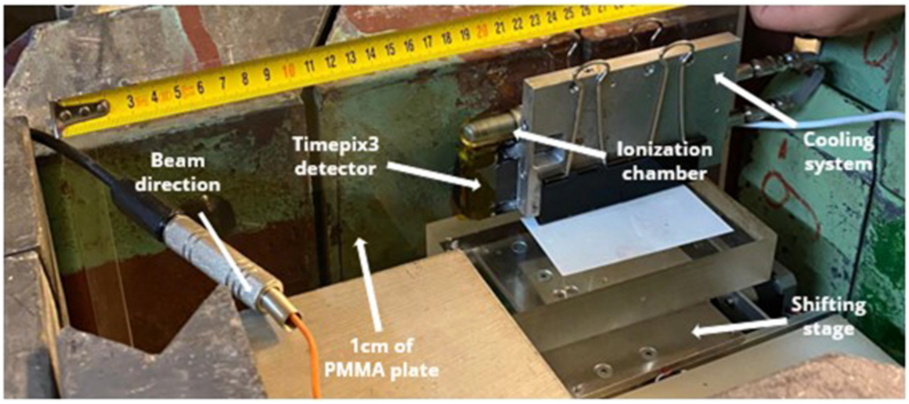

Figure 3.3.3: Image of the setup for stray radiation measurements. The Timepix3 detector is positioned laterally to the beam axis. In between, a PMMA plate is mounted. A 3 cm collimator is used for the beam. The image is taken from [OBP$^+$22].

thickness, respectively. The sensor material for both sensors is silicon. Electrons with an energy of 23 MeV were used at different intensities between 100 nA, 1000 nA corresponding to a dose range of 4 Gy/s to 40 Gy/s. The detector was placed laterally to the beam at a distance of 10 cm from the beam core. In front of the detector, a PMMA plate with a thickness of 1 cm was mounted. A collimator with a diameter of 3 mm was used for the beam. The setup is illustrated in figure 3.3.3. The measurements were performed at three different intensities. The measured dose rate in dependence on time is shown in figure 3.3.4. A linearity of the measured dose rate to the beam intensity was measured. Additionally, the detector shows time stability. At the measurements with an intensity of 1000 nA, an increase in the dose rate with time is observed, resulting from fluctuations in the beam delivery. It is therefore also possible to detect instabilities of the radiators with the Timepix3 detector.

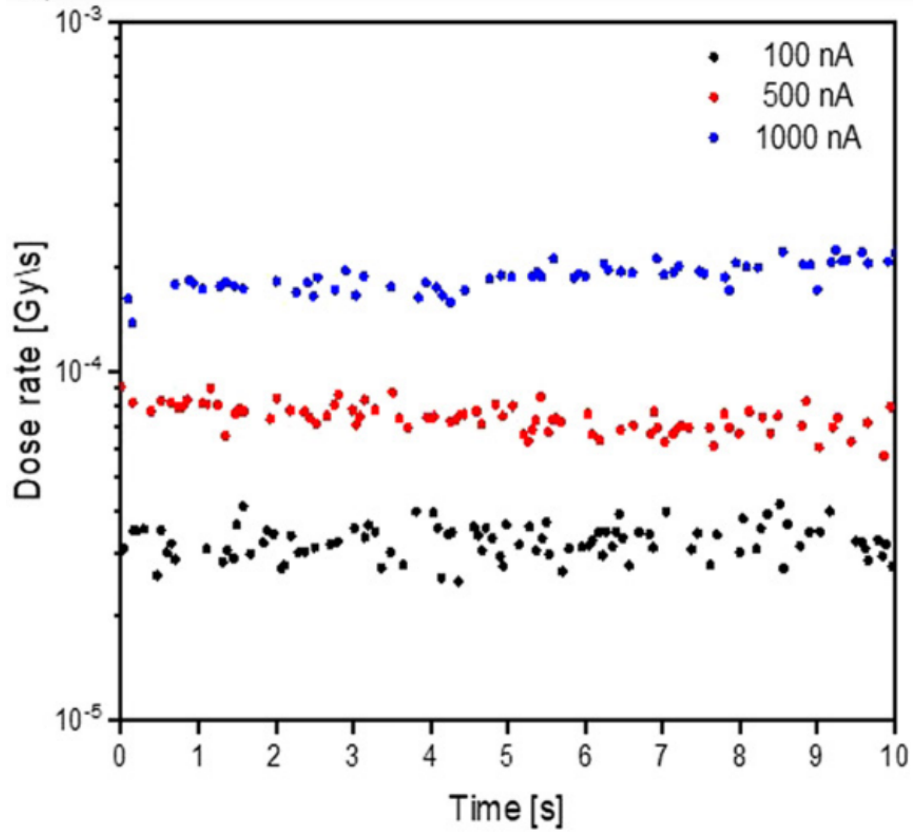

Figure 3.3.4: Measurements with the Timepix3 detector at different beam intensities. The detector can detect beam instabilities like the increase in dose rate at the measurement with a beam intensity of 1000 nA. The figure is taken from [OBP+22].

4 Threshold equalization and energy calibration

Contents

The individual energy thresholds of the pixels of Dosepix need to be equalized in order to conduct proper measurements. Otherwise, the individual thresholds would differ due to small mismatches between transistors of different pixels [Won12]. Additionally, an energy calibration is performed to convert ToT values into energies in keV. Both procedures are explained in the following.

4.1 Equalization

The analogue energy threshold is set globally for all pixels. However, a digital threshold equalization must be performed because of the differences in the electronics of the single pixels [Won12]. The digital threshold for each pixel is adjusted via a global threshold DAC (digital-to-analogue converter) and individual pixel DAC values. Latter are adjusted to fit a global analogue threshold. The pixel DACs per pixel consists of 6 bit, so 64 different values are possible. The threshold equalization is performed in darkness so that optical light does not have an influence on the equalization. The signal produced by a single optical photon does not exceed the noise level, however high photon fluxes of light can lead to pile-up causing the signal to exceed the threshold and influence the threshold equalization process. Dosepix is operated in photon counting mode (see section 2.5.2). The noise level of each pixel is determined first. For this, the threshold DAC is varied from a small to a high value, corresponding to a scan from high to small energies. The value at which noise is measured yields the noise level. This is performed for every pixel for the highest pixel DAC 63 and the smallest pixel DAC 0. This leads to two distributions for the detected noise levels. Subsequently, the mean value of the two determined threshold values is calculated for each pixel yielding a third distribution. The DAC values corresponding to this distribution are the operation pixel DACs

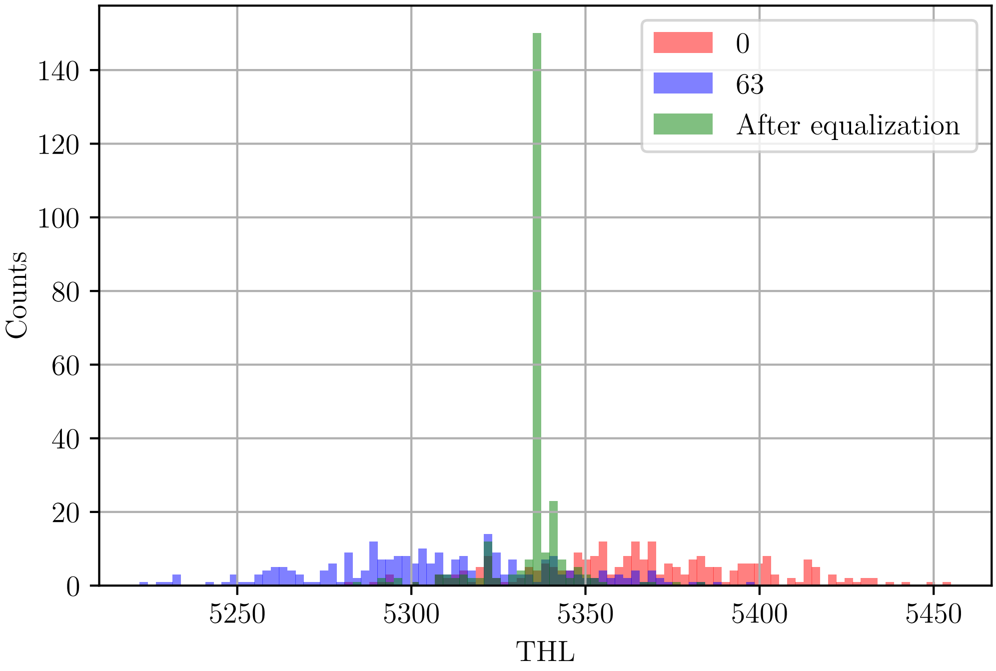

Figure 4.1.1: Distributions of the pixel DACs 0, 63 and the distribution of the mean values after the equalization.

for following measurements. The distributions are shown in figure 4.1.1. In the second step, the analogue threshold is increased so that it exceeds the noise level of all pixels by at least 20 ensuring noise stability. Otherwise, noise may exceed the threshold and is registered in the measurements. This value is the global digital threshold [Haa18].

4.2 Energy calibration

In this section, the energy calibration procedure is described. It is needed to convert ToT values into deposited energies in units of keV. In order to perform an energy calibration, measurements with sources of known photon energies must be performed. Dosepix is utilized in ToT-mode since it provides exact ToT values and therefore best energy resolution. The convolutional neural network developed in [Sch21] is used for the energy calibrations. Only a single measurement is needed for this method. An ^{241}Am-source is used for all calibrations in this thesis. The source is put close to the detector in order to gain high statistics. Additionally, a

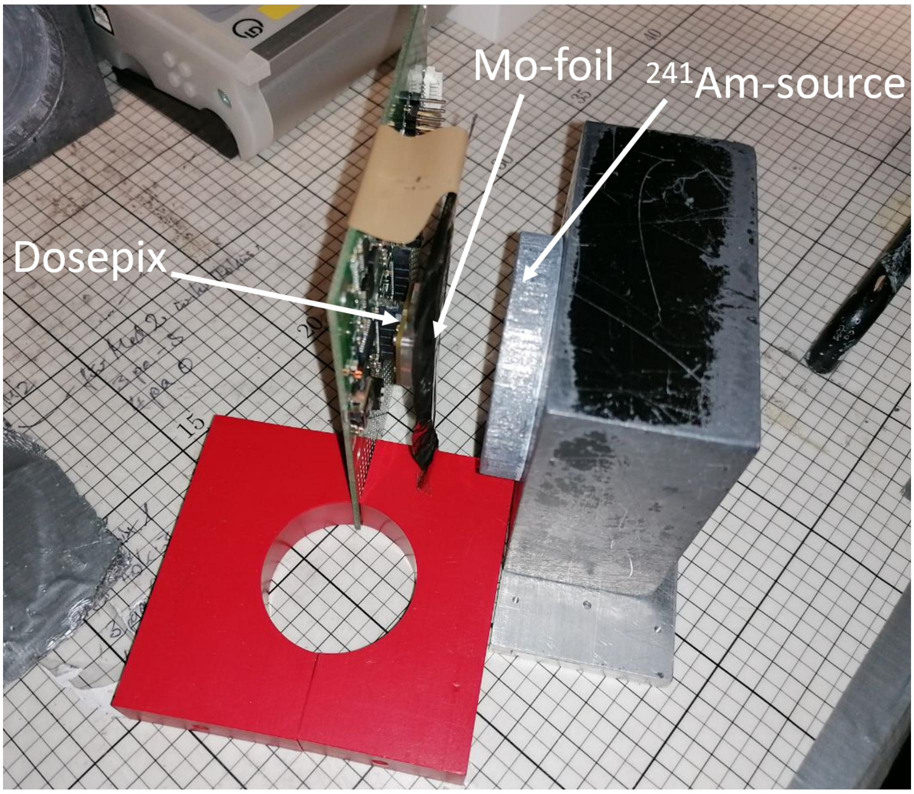

Figure 4.2.1: Setup of the calibration measurements. An ^{241}Am-source is used to irradiate Dosepix, with an Molybdenum foil in between. Fluorescence photons are produced by irradiating the Molybdenum foil. This results in two full-energy peaks, one for each source, which are sufficient for the energy calibration.

Molybdenum foil is placed between the ^{241}Am-source and Dosepix. This leads to the production of fluorescence photons from the k shell of Molybdenum. Figure 4.2.1 shows a picture of the setup. The function for the conversion between ToT and deposited energy in keV is shown in figure 4.2.2. The function is described via ([JCH$^+$08]):

$$\mathrm{ToT}(E) = aE + b + \frac{c}{E - t} \tag{4.2.1}$$

The parameters a, b, c and t are determined by the neural network from the measured ToT spectra. For the function in figure 4.2.2, the values $a = 2$, $b = 100$, $c = -120$ and $d = 8$ are used. The parameter a describes the slope of the linear part of the function which mainly depends on I_{krum}, b is the offset of the function on the ToT-axis, c changes the shape of the transition between the linear and the hyperbolic part of the function and t is the shift of the function on the deposited energy axis. The function consists mainly of two parts. For high energies, the

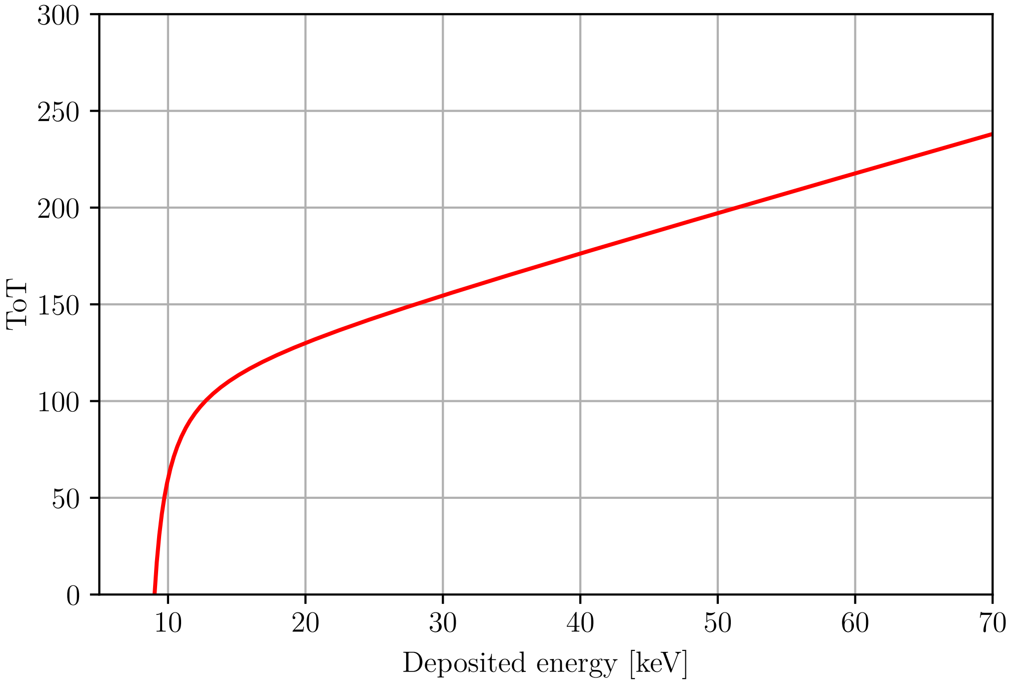

Figure 4.2.2: The function shows an example of the conversion between ToT values and the deposited energy in units of keV. The used parameter values are $a = 2$, $b = 100$, $c = -120$ and $d = 8$.

relation between ToT and deposited energy is linear with the slope depending on I_{krum}. However, at small energies, the relation between ToT and energy becomes hyperbolic [Sch21]. A ToT-measurement of the ^{241}Am-source and the Molybdenum fluorescence target and the resulting energy deposition spectra are shown in figure 4.2.3. This measurement is performed with a I_{krum} of 7 nA and a bias voltage of 100 V. Two peaks are visible in the ToT measurements: the full-energy peak of the photons from the ^{241}Am-source at 59.54 keV ([NIS]) and the full-energy peak of the XRF photons from the Molybdenum foil at 17.48 keV ([NIS]). After the energy calibration, the full-energy peak of ^{241}Am-photons is visible at approximately 60 keV and the full-energy peak of Mo-photons at approximately 17 keV. The structure at approximately 10 keV results from Compton scattering with the Compton edge at 11.25 keV which results from the maximal energy transition of photons on electrons for the interaction of Compton scattering. The energy of the Compton edge is calculated by formula 2.1.3.

The energy calibration depends on the bias voltage because of energy loss in the

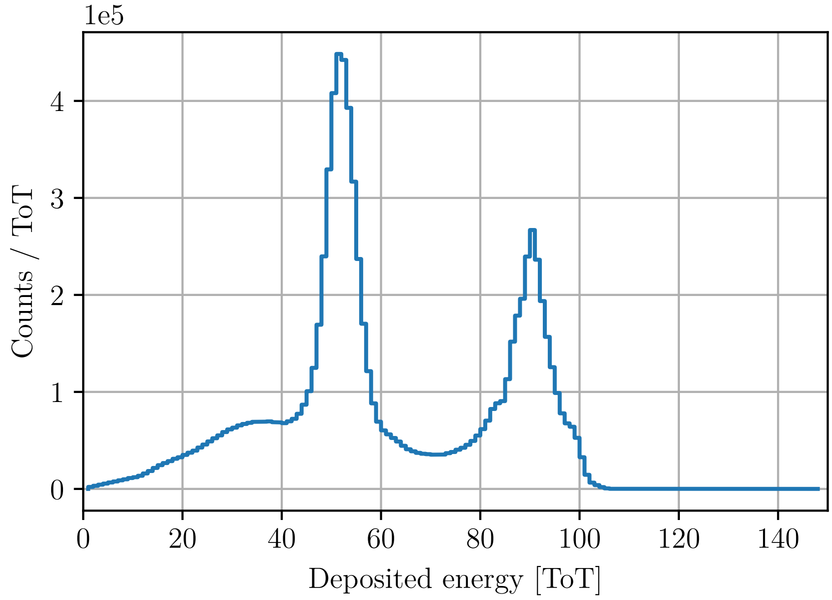

(a) ToT-measurement of calibration setup

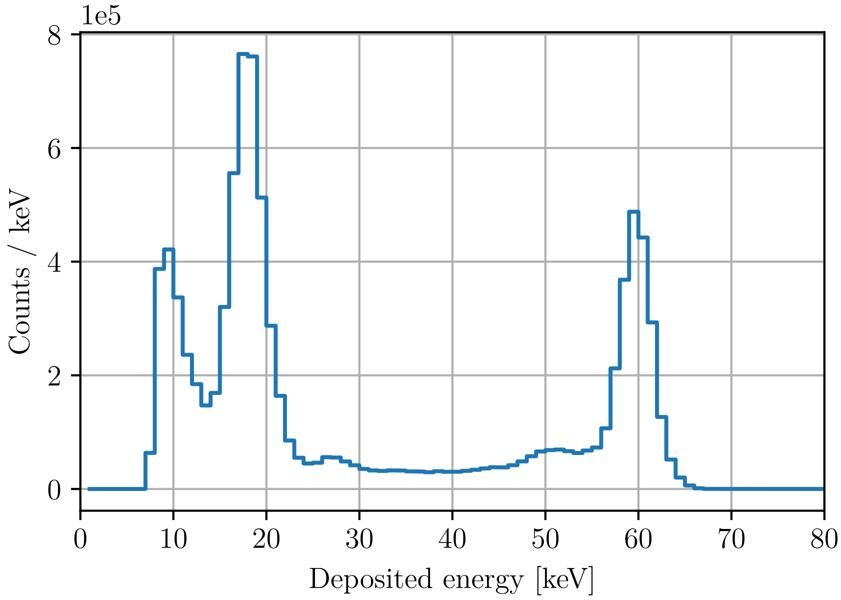

(b) Deposition spectrum after energy calibration

Figure 4.2.3: (a) shows a ToT measurement of the calibration setup with a I_{krum} of 7 nA and a bias voltage of 100 V and (b) shows the corresponding deposition spectra after the energy calibration.

undepleted part of the sensor and charge sharing. Therefore, a different energy calibration is required for every used bias voltage. Only large pixels are considered in the performed calibrations. The threshold voltage of a silicon p-n-junction is 0.7 V. However, a signal was still measured at a bias voltage of 0.3 V. The reason for this behavior is not known. Figure 4.2.4(a) shows the ToT-measurements of the calibration setup at different bias voltages. The shape of the deposition spectra depends on the bias voltage. Especially at small bias voltages, the peak corresponding to the fluorescence lines of the Molybdenum foil becomes small. Furthermore, the full-energy peak of ^{241}Am with the energy of 59.54 keV shifts towards smaller ToT-values with rising bias voltages. This is explained by leakage current which shows the same behavior as the peak positions as a function of the deposited energy as shown in [Ull21]. Figure 4.2.4(b) shows the spectra after the energy calibration. The energy deposition spectrum at a bias voltage of 300 mV looks clearly different compared to the spectra at higher bias voltages. Optimum calibration parameters cannot be determined by the network model due to the small Molybdenum peak. The energy deposition spectrum at 500 mV also shows deviations from the actual energy deposition spectrum since the full-energy peak of ^{241}Am is shifted to smaller energies and has a significantly larger width compared to higher bias voltages. Furthermore, the full-energy peak of Molybdenum does not appear in the energy deposition spectrum. The two full-energy peaks start to appear at higher bias voltages. Comparing the energy deposition spectra at 1 V, 5 V and 20 V to each other, the number of small energy events decreases with increasing bias voltage. This is explained by reduced charge sharing since the drift velocity increases with higher bias voltages which suppressing the spread of the charge cloud.

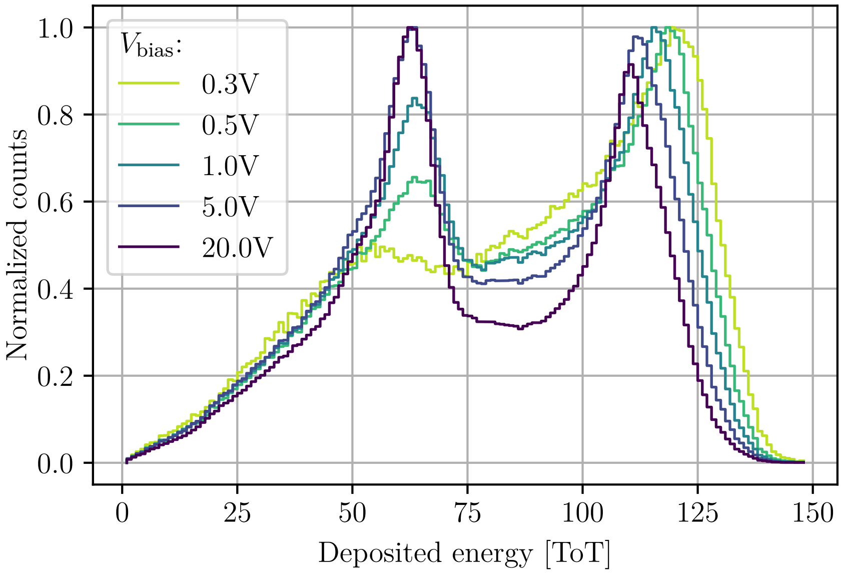

(a) ToT-measurements of calibration setup

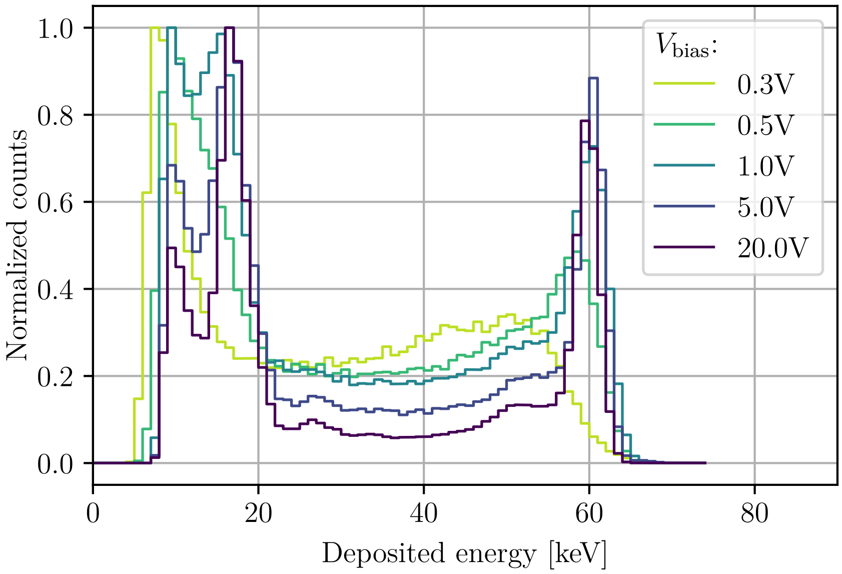

(b) Deposition spectra after energy calibration

Figure 4.2.4: (a) ToT-measurements of the calibration setup for different bias voltages and (b) the corresponding deposition spectra after the energy calibration. I_{krum} is set to 7 nA. The peak that results from the XRF photons of the Molybdenum foil becomes small at low bias voltages which causes the neural network failing to find the optimal parameters.

5 Dosepix-Ionization-Chamber

Contents

The key aspect of FLASH radiotherapy is the application of a radiation field with high doses within small time intervals with dose rates up to several Gy/s [RSM$^+$20][SHF$^+$20]. These dose rates pose a problem to a conventional Dosepix detector setup since the high particle flux causes pile-up. This means that one detector event consists of several particles depositing energy in a sensor pixel within the time the charge signal induced by the first event remains above the threshold level (see chapter 2.5.1). In the conventional setup, a 300 µm thick silicon sensor is attached to the ASIC. The applied bias voltage of 100 V causes full depletion of the sensor material.

In this chapter, a Dosepix-ionization-chamber is introduced to circumvent the previously stated problems of a conventional Dosepix setup. The Dosepix-ionization-chamber is realized by utilizing the Dosepix detector without a sensor element. Figure 5.0.1 shows images of said ionization chamber. Figure 5.0.1(a) shows the photograph of the Dosepix-ionisation-chamber in an angle that allows the side view of Dosepix' ASIC. A copper plate is glued into the inner side of the plastic, shown in 5.0.1(b). The distance between Dosepix and the copper plate is approximately 3 mm. Ambient air is the medium interacting with the ionizing radiation resulting in charge carriers collected in the electrodes of the ASIC pixel. The idea is to measure electrons produced by the radiation that traverses the air between Dosepix and the copper plate. The required energy to produce electron-hole pairs in air is approximately 34 eV ([BCRM19]), which is significantly larger than the required energy of 3.62 eV in silicon ([Kno00]). A metal wire is soldered

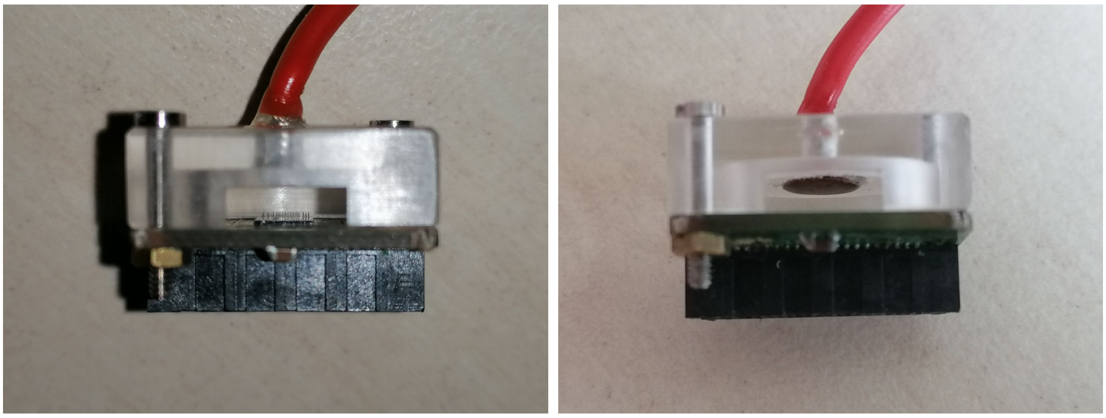

(a) Dosepix without sensor (b) Copper plate glued into the plastic cover.

Figure 5.0.1: Pictures of the Dosepix-ionization-chamber. A side view of (a) the Dosepix ASIC and in (b) the copper plate is shown.

on the copper plate, allowing the application of a voltage. Since Dosepix is on ground, an electric field is created between the detector and the copper plate. The voltage is applied by attaching one pole to the wire and the other pole to the USB plug, which is also on ground. A negative voltage is applied to the copper plate, which accelerates the produced electrons towards the ASIC, where they are measured. The maximal negative voltage applied to the copper plate is 2 kV. Figure 5.0.2 illustrates a scheme of the setup of the Dosepix-ionization-chamber. Since the Dosepix-ionisation-chamber is only supposed to measure secondary electrons produced by the radiation, not the primary particles itself, Dosepix is not radiated from the front as in the conventional case but from the side, parallel to the ASIC surface as it is shown in the figure. To shield the ASIC from direct irradiation, a layer of lead with a thickness of approximately 1 mm is attached to the side of the Dosepix-ionization-chamber. It must be mentioned that the layer of lead may also cover a part of the air between Dosepix and the copper plate resulting in the absorption of photons before they reach the air between Dosepix and the copper plate. In the conventional setup of the Dosepix detector, the operation mode is set to measure holes. Since electrons produce the signal at the Dosepix-ionization-chamber, not holes as in the conventional setup, the operation mode is set to measure electrons. The operation mode register (OMR) as well as the periphery DAC is listed in table 5.0.1.

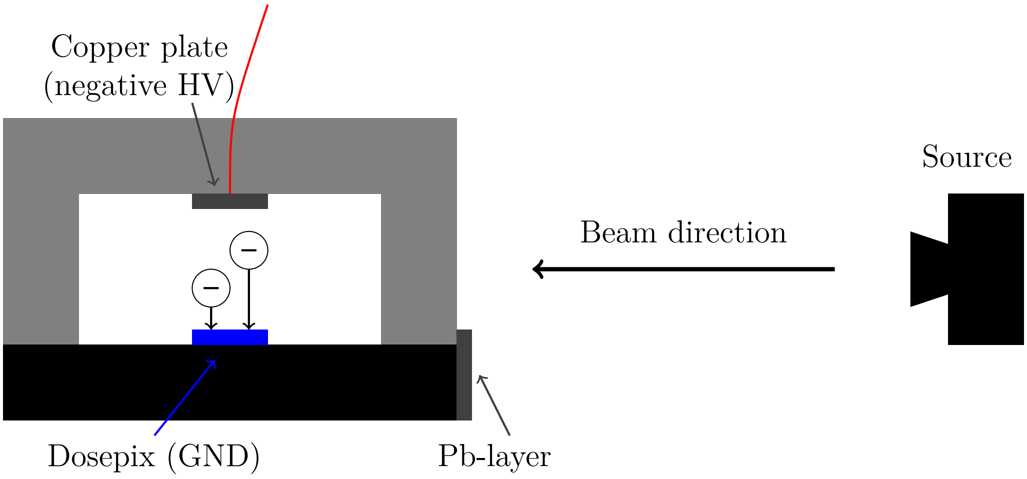

Figure 5.0.2: Scheme of the Dosepix-ionization-chamber. The radiation causes the production of electron-hole pairs in the air volume between the copper plate and Dosepix. An electric field between the copper plate and Dosepix is created by applying negative voltage to the plate, accelerating free electrons towards Dosepix.

Quantity	DAC-value
V_{tha}	5420
$V_{\mathrm{tpref,fine}}$	100
$V_{\mathrm{tpref,coarse}}$	255
I_{tpbufout}	128
I_{tpbufin}	128
I_{disc2}	118
I_{disc1}	48
$V_{\mathrm{casc,preamp}}$	130
V_{gnd}	80
I_{preamp}	100
V_{fbk}	200
I_{krum}	11
I_{pixeldac}	49
$V_{\mathrm{casc,reset}}$	220
OMR	bbffc0

Table 5.0.1: Periphery DAC and OMR of the measurements with the Dosepix-ionization-chamber.

5.1 Bias voltage variation

At first, the behavior of the Dosepix-ionization-chamber while applying different bias voltages is investigated. The radiation source is a MEGALIX CAT PLUS 125/20/40/80-122GW x-ray tube [MEG]. Its settings are a tube voltage V_{XRT} of 40 kV and a tube current I_{XRT} of 50 mA. These setting remain unchanged over the course of the radiations performed in this section. The distance between the Dosepix-ionization-chamber and the x-ray focus spot is approximately 10 cm. Dosepix is operated in Integration-mode utilizing 200 frames with a frame time of 0.2 s. The integrated ToT (iToT) values are calculated by summing up all pixel values over all frames. For each pixel, the standard deviation over all frames is determined. The error on the iToT value of one measurement is calculated by Gaussian error propagation over all pixel values. Figure 5.1.1 shows the iToT value as a function of the bias voltage. For bias voltages $V_{\mathrm{bias}} < 1300\,\mathrm{V}$, the iToT value is

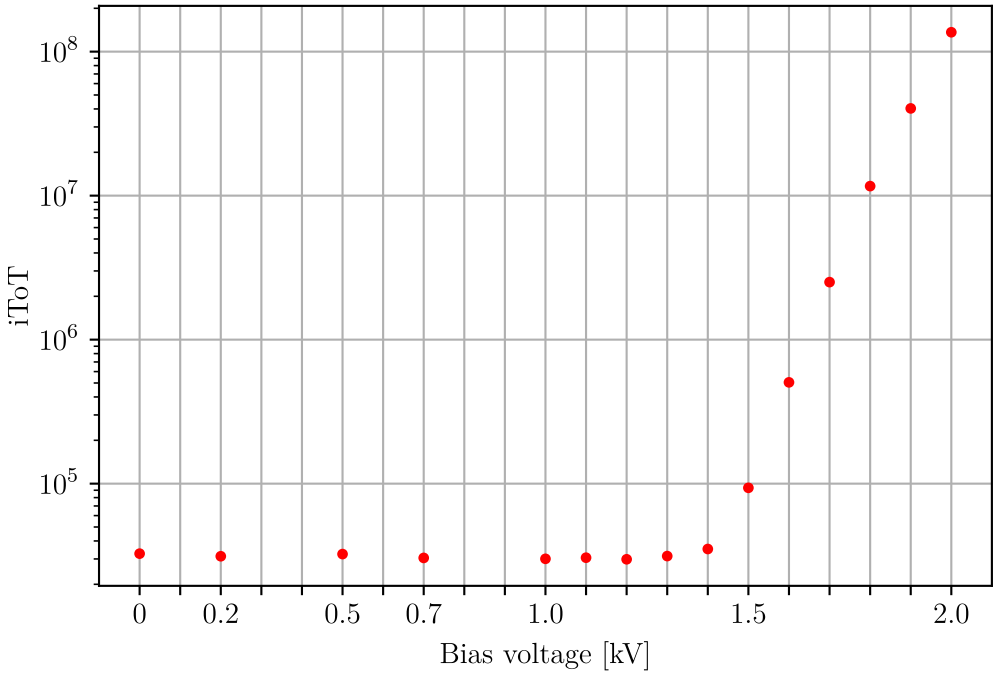

Figure 5.1.1: Integrated ToT value iToT as a function of the applied bias voltage. For all measurements, the tube voltage is 40 kV, the tube current is 50 mA and 200 frames are recorded with a frame time of 0.2 s. The data is shown with statistical errors which are smaller than the data points. A nonzero constant value is observed for bias voltages up until 1.3 kV. An exponential increase of the iToT value is visible for bias voltages above 1.3 kV.

nonzero and remains approximately constant. This nonzero value most likely results from stray radiation that hits the ASIC. It is produced by scattering the incoming photons that are scattered by the material of the Dosepix-ionization-chamber and air. No pixels were noisy in the measurements. For bias voltages $V_{\text{bias}} > 1300\,\text{V}$, the iToT value begins to rise with increasing bias voltage. The probability of free electrons reaching the ASIC and being measured before they are captured by another atom rises with increasing bias voltage. This shows that it is basically possible to measure with the Dosepix-ionization-chamber. In order to investigate the stability of the measurements, the time dependency is investigated in the next section.

5.2 Time dependency

In this section, the stability of measurements with the Dosepix-ionization-chamber is investigated by examination of the time dependency of iToT. It is expected that an ionization chamber shows constant response over prolonged exposures for unchanging irradiation conditions. A time dependence impairs the correctness and reproducibility of the measured dose. In order to investigate time dependency, the total iToT values of each frame are determined. This is done by summing the iToT values of all pixels within one frame. Each frame corresponds to a time interval of the chosen frame time, which is set to 0.5 s.

First, a Dosepix detector with a fully depleted 300 µm thick silicon sensor is irradiated to establish a comparison for the Dosepix-ionisation-chamber. A measurement with the standard setup of the Dosepix detector, including a sensor, yields the expected course. Dosepix is irradiated frontal for this measurement, in contrast to the measurements with the Dosepix-ionization-chamber. Figure 5.2.1 shows the time dependency of the mean <iToT> value, which is the mean ToT value over all pixels within one frame, as a function of frames, corresponding to a time interval. The uncertainties are calculated by the standard deviation over all frames for each pixel. Subsequenty, all determined standard deviations are squared and and summed up. The square root of this value yields the uncertainty of the measurements. The frame time is 0.5 s. It is nearly constant over time with several bumps potentially corresponding to voltage ripples. The bias voltage is set to 100 V. The iToT value stays constant except for some deviations that may result from kV-ripples.

Next, the course of the iToT value as a function of time from measurements with the Dosepix-ionization-chamber is investigated. The applied bias voltage is set to 2 kV. An exemplary measurement is shown in figure 5.2.2(a). The mean integrated ToT value <iToT> is illustrated dependent on time. The uncertainty is calculated by the standard error, which is the standard deviation divided by the square root of number of pixels. It is observed that the mean iToT value remains constant for

the first frames. Over the course of several frames, the mean iToT value starts to rise exponentially. A reason for this behavior is explained in the following.
The sensitive part of the pixels covers only a small part of the ASIC pixel area. The sensitive part are the electrodes on the ASIC which have an octagonal shape with a diameter of 25 µm ([Won12]). This corresponds to an area of 60.36 µm^2. The ASIC pixels have a size of 220 µm x 220 µm. This yields a ratio between the area of the electrode and the area of the pixel of 0.12%. This means that 99.88% of the ASIC area is not sensitive to particles. Secondary electrons produced by the radiation of the Dosepix-ionization-chamber are accelerated towards the ASIC, where they do not necessarily hit the sensitive part of the pixels. This leads to the collection of electrons on the surface of the ASIC. Consequently, these electrons deflect later produced secondary electrons towards the sensitive part of the pixels because of repulsion. After the collection of a certain amount of electrons at the

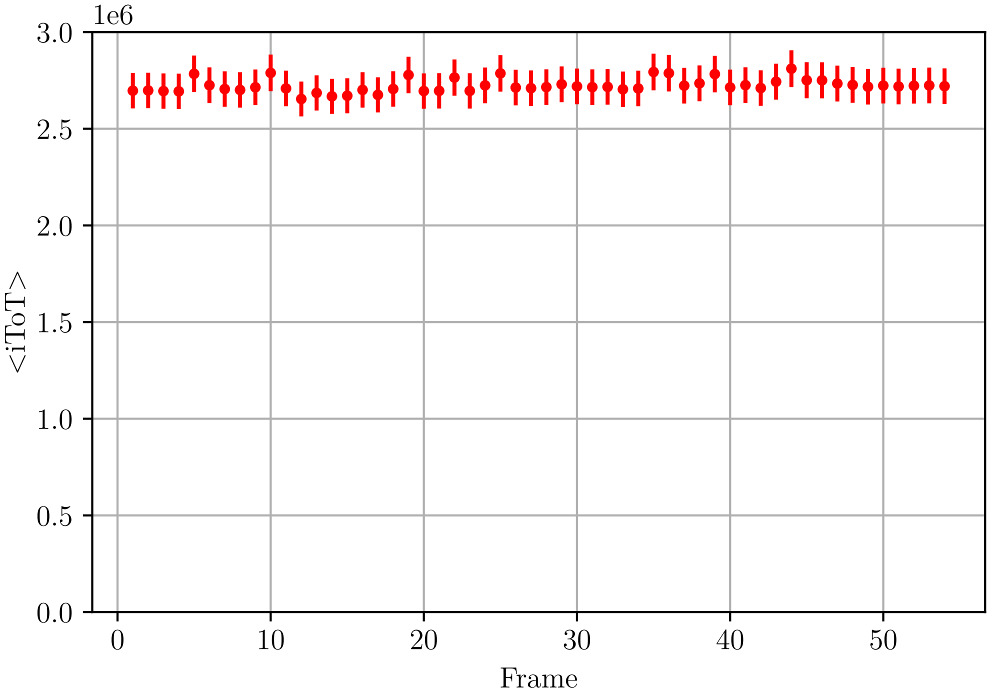

Figure 5.2.1: Time dependency of the standard setup of the Dosepix, including a sensor. The frame time is set to 0.5 s, the tube voltage is 40 kV and the tube current is 50 mA. The distance between the focal spot of the x-ray tube and the Dosepix detector is approximately 60 cm. Statistical uncertainties were calculated via the standard error.

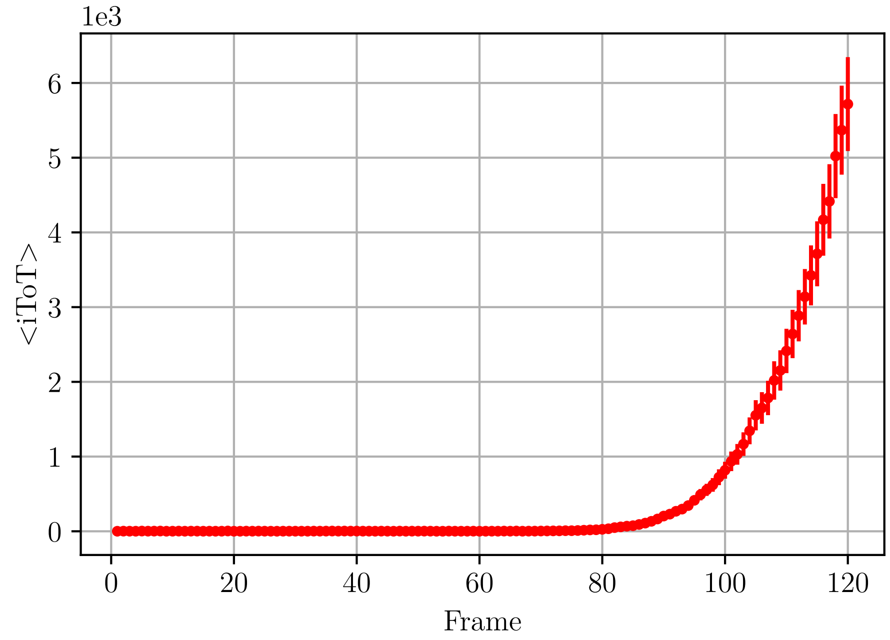

(a) $V_{\text{bias}} = 2\,\text{kV}$

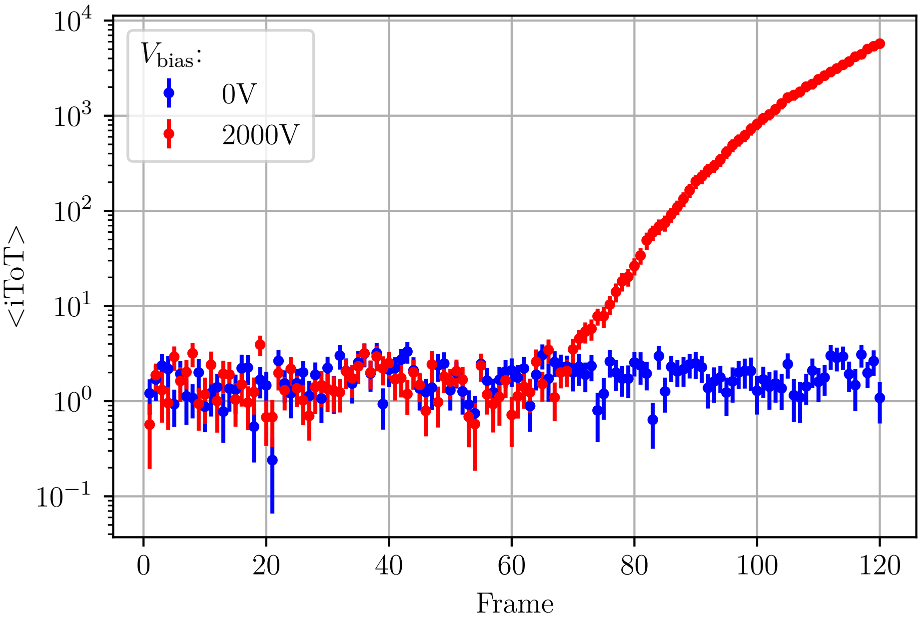

(b) Comparison between measurements at $V_{\text{bias}} = 0\,\text{V}$ and $V_{\text{bias}} = 2\,\text{kV}$.

Figure 5.2.2: (a) Time dependence of the Dosepix-ionization-chamber at $V_{\text{bias}} = 2\,\text{kV}$. For a comparison with the measurement at $V_{\text{bias}} = 0\,\text{V}$, the measurement from (a) is shown with a measurement at $V_{\text{bias}} = 0\,\text{V}$. The frame time is 0.5 s. The iToT value stays identical for the first 60 frames, then the iToT value at 2 kV begins to increase. The uncertainties are calculated by the standard error.

insensitive part of the pixels, enough secondary electrons are deflected towards the sensitive part of the pixels, leading to a measureable signal. Since the population of collected electrons on the ASIC further increases with longer irradiation times, this effect becomes more dominant causing larger iToT values. However, this is only a not proven theory.
In figure 5.2.2(b), the measurement from 5.2.2(a) is shown logarithmically together with a measurement at $V_{\text{bias}} = 0\,\text{V}$. The mean iToT value is nearly identical for the first 60 frames in both measurements. This means that no secondary particles are detected, only stray radiation that hits the ASIC. The signal is produced by photons interacting in the ASIC and producing a charge in the electrodes. The expectation would be that the mean iToT value is bigger at $V_{\text{bias}} = 2\,\text{kV}$, since secondary electrons produced by the primary radiation are accelerated towards the ASIC because of the present electric field and hit the pixel, which results in the collection of charge. However, the sensitive area of the pixels is too small to cause a significant rise in the mean iToT value for the first frames. After 60 frames, the mean iToT value in the measurement with a bias voltage of 2 kV rises because of a high electron population on the insensitive part of the pixels leading to deflection of secondary electrons towards the sensitive pixel area.

In order to further investigate the time dependency, multiple measurements are performed after each other with different waiting times in between. It is tested if the curves show similar trends for each measurement or if the data is affected by previous measurements. The duration of the waiting time was increased inbetween the measurements to examine the influence of the waiting time on the data. Again, Dosepix is operated in Integration-mode with a frame time of 0.5 s. Figure 5.2.3 shows the corresponding measurements with the longest waiting time being 900 s. It has to be kept in mind that the waiting time corresponds to the time between the end of the last measurement and the new run of the script which starts the measurement. Since a Raspberry Pi is used for these measurements, the duration between running the script and the start of the measurement is relatively long, with approximately 11 s. This leads to an additional time delay of 11 s between the actual measurements. The curves differ from each other, resulting in non-reproducible measurements. For the first exposure, the iToT value stays nearly constant for the first 80 frames, subsequently, the curve rises. The script was started again directly after the previous measurement was finished. The radiation was kept switched on between the first and second measurements. For all the other measurements with a longer waiting time, the radiation was switched off to stop collecting further electrons on the ASIC. The measurement with a waiting time of 0 s shows a bigger iToT value in the first frame than in the last of the first measurement. This may be due to the constant exposure to the radiation of the x-ray tube in between

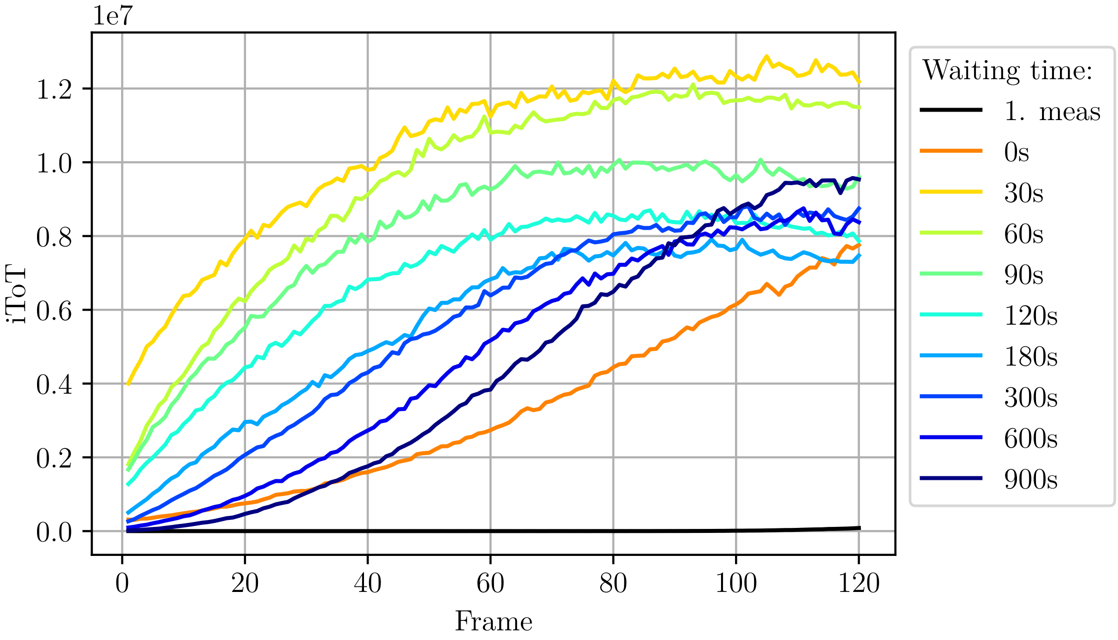

(a) Linear representation

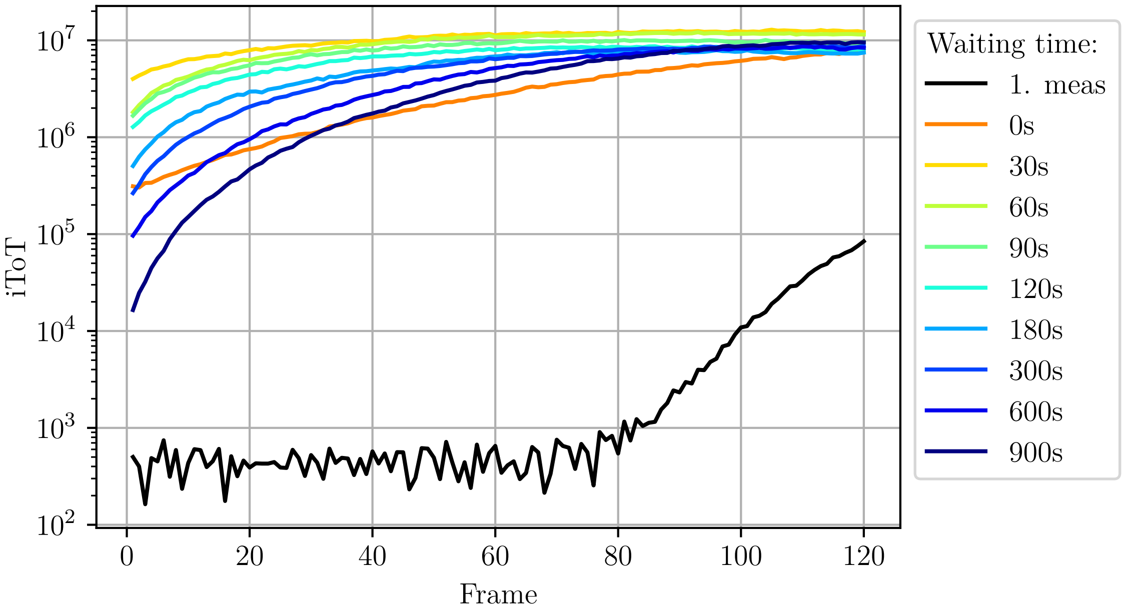

(b) Logarithmic representation

Figure 5.2.3: Time dependence of the iToT value for multiple measurements with different waiting times in between, which are illustrated by different colors. The measurements are taken in Integration-mode with a frame time of 0.5 s. (b) is the logarithmic representation of (a).

the measurements. The iToT value increases further for the whole measurement. After a waiting time of 30 s, the iToT value of the first frame is smaller than the iToT value of the last frame of the previous measurement. This is due to the fact that the radiation was switched off between the measurements, and the number of electrons collected on the ASIC decreased again. Potential reasons for this decrease are repulsion and recombination with ambient air. The iToT value increases, but reaches saturation. Curves of similar shape are observed for further measurements. The first iToT value becomes smaller with bigger waiting times since the population of collected electrons on the insensitive parts on the ASIC decreases with increasing time between the measurements. Furthermore, the curves show saturation at smaller iToT values with increasing waiting time. This is discussed in the following.
In contrast to the electrons getting accelerated towards Dosepix, the ionized atoms are accelerated towards the copper plate, which leads to a compensation of the electric field, causing it to decrease. Because of the decreased electric field, the probability for recombination rises, and the event rate decreases. For a waiting time of 300 s and longer, the value of the saturation increases again because the charge on the copper plate decreases with time because of repulsion and recombination with ambient air. Another interesting point is that even after 900 s the Dosepix-ionization-chamber is not reset to its initial state again since the iToT value of the first frame is larger than the iToT of the first frame of the first measurement. Additionally, the iToT value starts to rise instantly. It is possible to measure the secondary electrons produced by the radiation, but challenging to extract knowledge from the data because of the strong time dependency. In figure 5.2.4, the iToT value from the whole measurement series from figure 5.2.3 is shown again as a function of time in order to see the development of the iToT value.

Furthermore, the time development of the iToT values for long radiation times is investigated by taking a measurement with 1200 frames with a frame time of 0.5 s. The measurement is performed 900 s after the previous one. The previous measurement is the one corresponding to a waiting time of 900 s in figure 5.2.3. Figure 5.2.5 shows the course of the measurement. The iToT value rises until it reaches a maximum. Instead of saturation, the iToT value decreases again with time. The point of maximal iToT occurs when there is an optimal ratio of electrons deflecting the incoming particles and the compensating electric field caused by the ionized atoms on the copper plate. After the maximum is reached, the opposing electric field dominates the effect of deflection of secondary electrons toward the sensitive pixel areas, and the iToT value decreases. For huge irradiation times, the iToT value saturates. The saturation occurs when there is an equilibrium between the electric field produced by applying a voltage and the opposing electric field produced by the collection of electrons on the ASIC and ions on the copper plate.

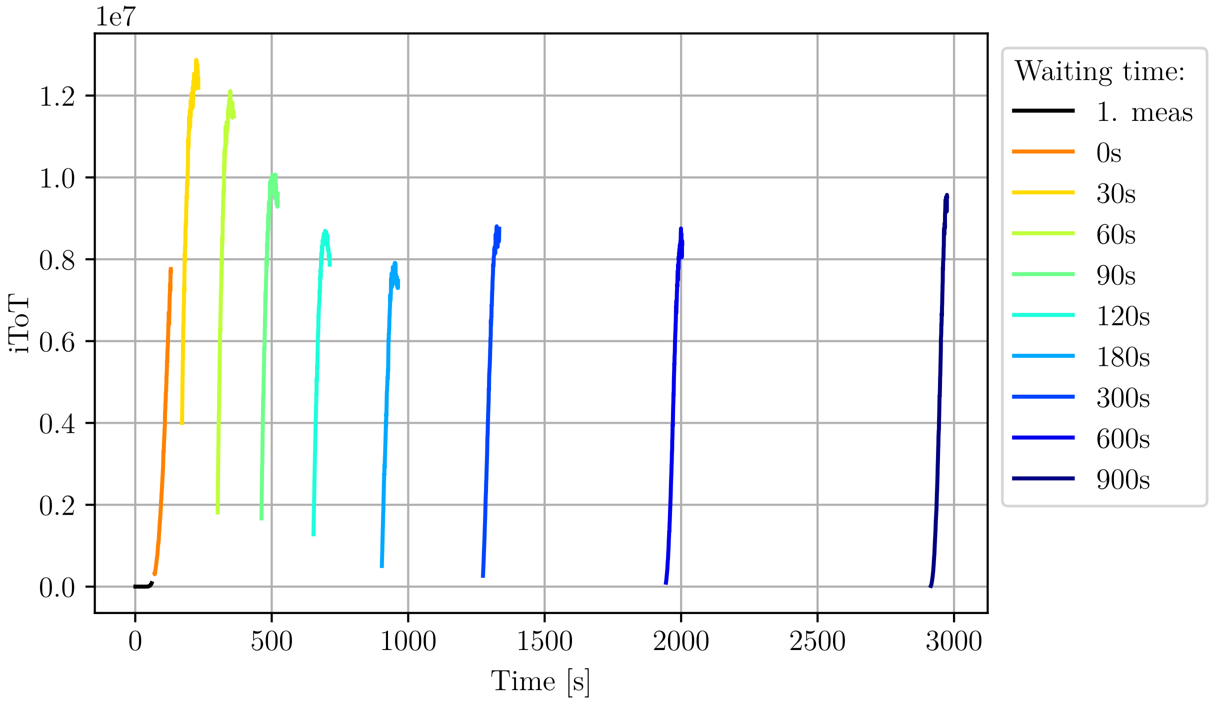

Figure 5.2.4: Illustration of figure 5.2.3 in real-time, including the duration of the detector exposure and the waiting time on the x-axis and the iToT on the y-axis. Each color represents a measurement with a different waiting time.

The last investigation regarding time dependency is switching the radiation off and on during a single measurement. The taken data is shown in figure 5.2.6. The iToT value drops immediately after switching off the radiation. After some time, the radiation is switched on again, which leads to an instant increase in the iToT value. The iToT value when switching off the radiation is not reached directly again. This is explainable by the decreasing number of deflecting electrons on the ASIC without radiation. However, the curve displays the same behavior as shown in figure 5.2.5 since the iToT value reaches a maximum and then decreases again. As a conclusion, it was shown that the data taken with the Dosepix-ionization-chamber is strongly dependent on the exposure time resulting in a severe problem in the reproducibility and the ability to extract knowledge from the data. Therefore, methods must be determined to deal with this issue which is discussed in the next chapter.

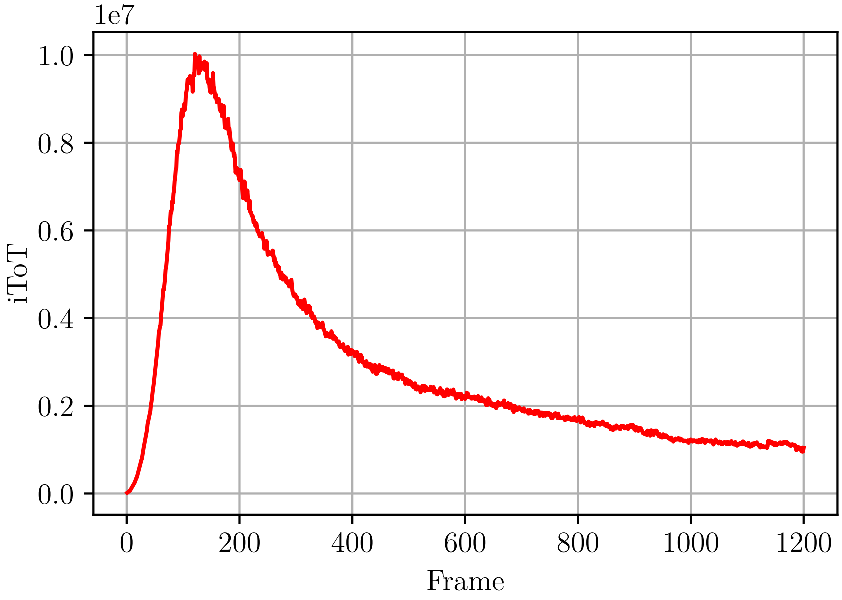

Figure 5.2.5: Development of the iToT value with time, represented by the frame index, at constant radiation conditions. The bias voltage is set to 2 kV. The duration between this and the previous measurement is 900 s. The frame time is 0.5 s. The course reaches a maximum, followed by a decrease of iToT.

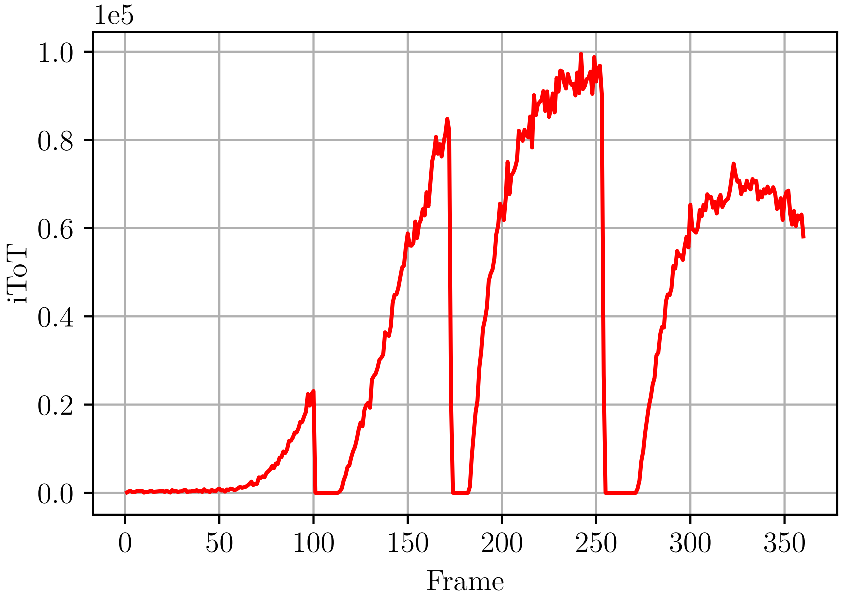

Figure 5.2.6: Integrated ToT value as a function of time, corresponding to the frame index, when switching the radiation off and on. The frame time is 0.5 s.

5.3 Attempts to suppress time dependency

In the previous section, it was demonstrated that the time dependency of the Dosepix-ionization-chamber poses a huge challenge to its operation. Therefore, two different methods are tested to overcome this issue. The first one is turning off the voltage supply, and the second one is turning off the voltage supply together with removing the USB plug from the Dosepix-board. For both approaches, measurements were performed before and after the procedure. Dosepix was operated in Integration-mode with an amount of 120 frames and a frame time of 0.5 s. The mean iToT value as a function of time, represented by the frame index, is shown in figure 5.3.1. Figure 5.3.1(a) shows the data for turning off the power supply. The mean iToT value is smaller after switching the power supply off and on again. Nevertheless, the Dosepix-ionization-chamber is not in its initial state, and the measurement shows a similar course as before. Figure 5.3.1(b) shows the data for turning off the power supply and additionally removing the USB plug. The measurement before and after are also similar and do not give any indications for a solution. The curves are even more alike than the ones in figure 5.3.1(a) which does not match the expectation since turning off the power supply was done in both approaches, whereas in the second approach an additional step was performed by removing the USB plug. All of the curves do not start at zero mean iToT since they are all affected by time dependency, since each measurement was preceded by another one.

Unfortunately, no approach solved the problem of the time dependency of the Dosepix-ionization-chamber. Nevertheless, the response of the Dosepix-ionisation-chamber on different radiation conditions was investigated by changing different parameters of the x-ray tube. The measurements are shown in the next section.

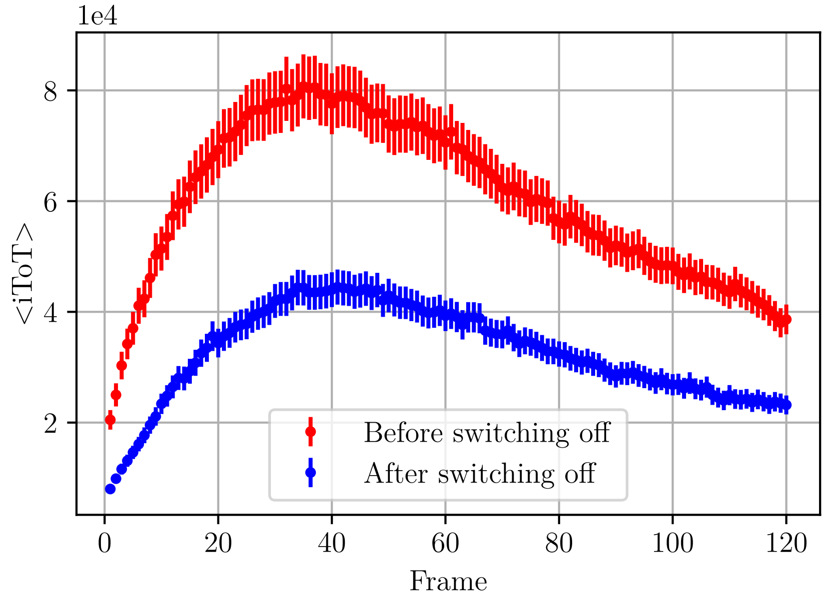

(a) Before and after switching off the power supply.

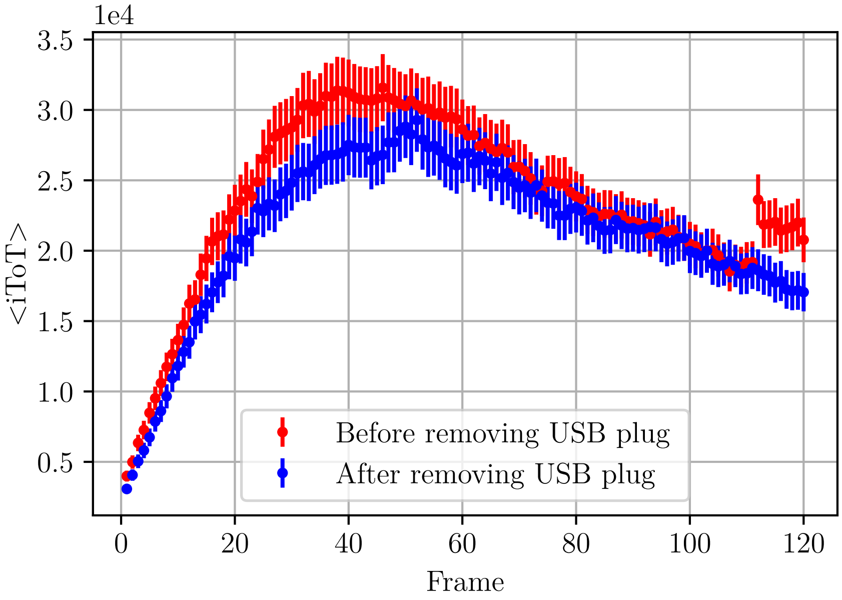

(b) Before and after removing the USB plug.

Figure 5.3.1: Time dependency of the mean iToT value. The time is represented by the frame index. The frame time is set to 0.5 s. (a) corresponds to the approach of turning off the voltage supply, and (b) corresponds to the approach of turning off the voltage supply and additionally removing the USB plug from the Dosepix-board. The uncertainties are calculated via the standard error of the iToT value over all pixels within each frame.

5.4 Tube current variation

In this section, the response of the Dosepix-ionization-chamber on varying tube currents is investigated. This is done by taking measurements in Integration-mode with a frame time of 0.5 s, a bias voltage of 2 kV, and a tube voltage of 40 kV. The used tube currents are 10 mA, 20 mA, 30 mA, 40 mA and 50 mA. Figure 5.4.1(a) shows the corresponding measurements which were taken directly after each other. Therefore, the data is affected by time dependency investigated in section 5.2. For the measurements carried out with a tube current of 40 mA and 50 mA, the iToT value starts to rise linearly from the beginning on. Subsequently, a decline in the slope is observed. Even a maximum is reached at a tube current of 50 mA, followed by a decrease of iToT. The iToT values corresponding to the other tube currents reach a linear course after an increase following a different function. The first measurement was taken at a tube current of 30 mA. Therefore, this measurement starts at a smaller iToT value than the measurements with smaller tube currents. The number of electrons collected on the ASIC increases linearly with time because of the constant flux of the x-ray tube. This explains the linear part of the course. The slope is determined by a linear fit applied to the linear part in each measurement (red lines) and shown in figure 5.4.1(b) as a function of the tube current. The slope of the linear part of each curve in figure 5.4.1(a) becomes larger with increasing tube current, which is explainable by the increase in flux with the tube current. The increased flux leads to faster growth of the electron population on the ASIC. It shows an exponential course. The observed dependency of the iToT value and the tube current shows a correlation between the measurements and reality. However, this could also result from the strong time dependency since a measurement influences the following one because of the collected electrons on the ASIC. This means that the Dosepix-ionization-chamber is not operated in its initial state. Therefore, the measurement series is repeated with multiple hours between the single measurements resetting the Dosepix-ionization-chamber to its initial state. The corresponding results are shown in figure 5.4.2(a). The frame time is 0.5 s. The curves start at a non-zero constant value and then start to rise compared to the measurements shown in figure 5.4.1(a). The iToT value of the measurement at a tube voltage of 30 mA starts to rise earlier than the one at 40 mA, which does not match the expectation since the particle flux rises with increasing tube currents leading to a faster collection of electrons on the ASIC. Linear fits are used to determine the slope. In figure 5.4.2(b), the slope is shown as a function of the tube current. It is not observed a exponential course as shown in figure 5.4.1(b), but from 10 mA until 30 mA, a linear course is observed. The slope at a tube current of 40 mA does not match the rest of the measurements. In conclusion, no clear trend of the measured data is observed which prevents reproducibility. Therefore, it is not possible to extraction of useful information from the data.

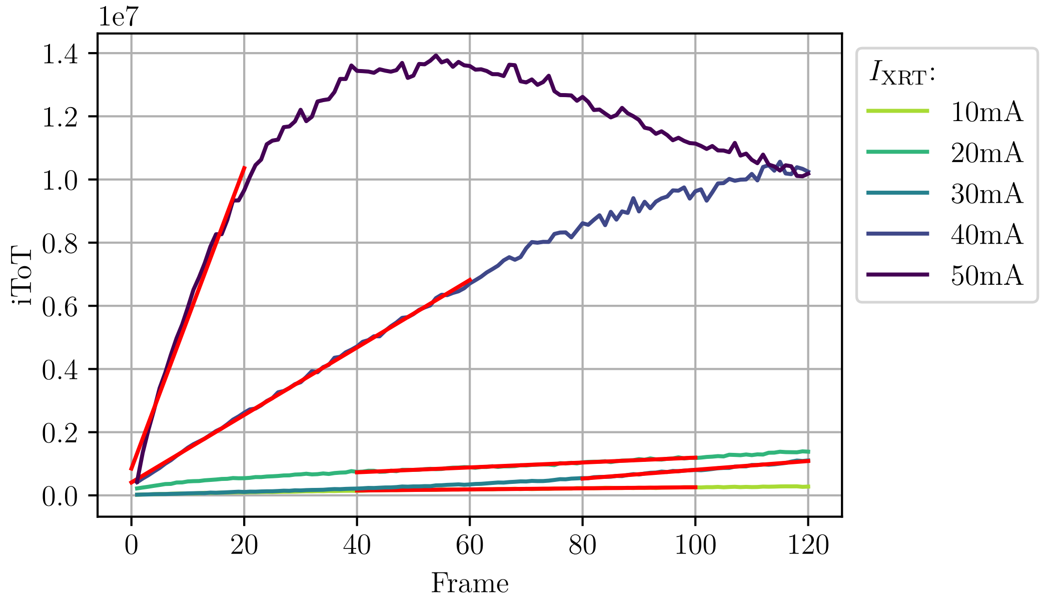

(a) Dependence of iToT development on the tube current.

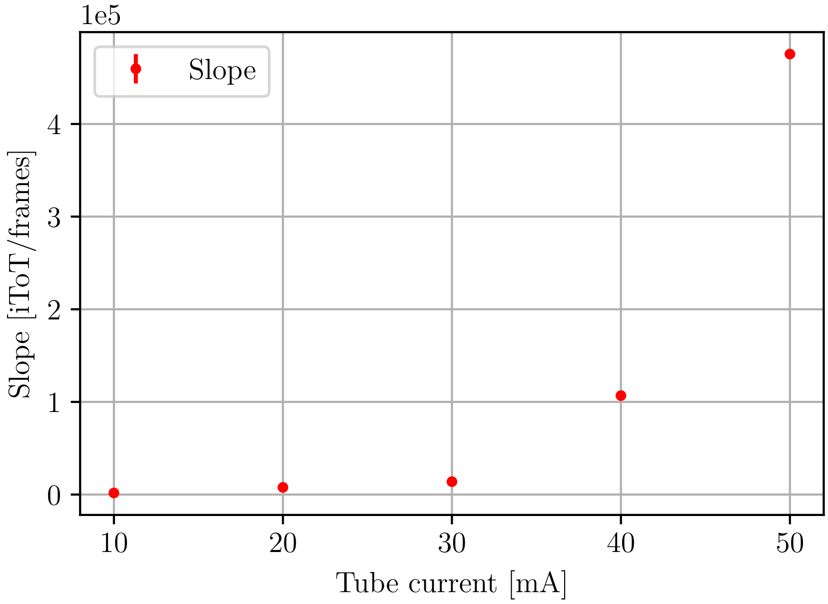

(b) Determined slops as a function of the tube current.

Figure 5.4.1: The iToT value of measurements at different tube voltages as a function of time, represented by the frame index is shown in (a) with a linear fit (red lines). (b) shows the slope of the linear part of the measurements as a function of the tube current. An exponential course of the slope as a function of the tube current is observed. The data is shown with uncertainties which are smaller than the size of the data points. The uncertainties were determined by the error of the fit parameters.

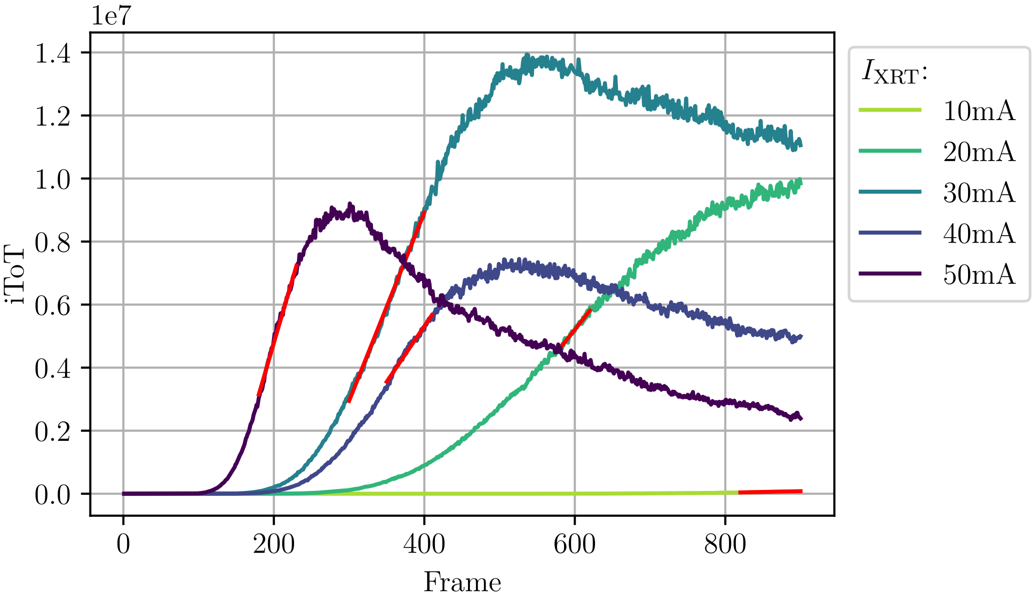

(a) Dependence of iToT development on the tube current.

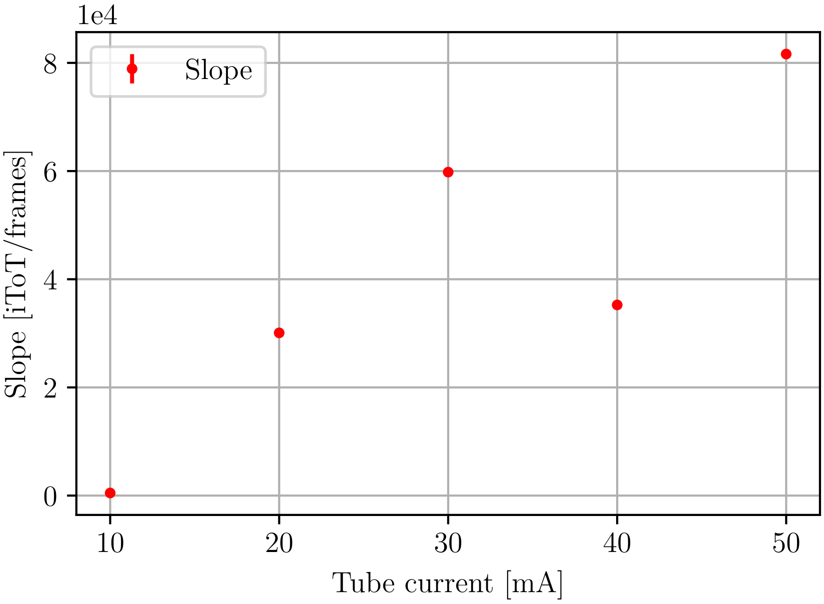

(b) Determined slops as a function of the tube current.

Figure 5.4.2: The iToT value of measurements, with the Dosepix-ionization-chamber in its initial state, at different tube voltages as a function of time, represented by the frame index, is shown in (a) with a linear fit (red lines). (b) shows the slope of the linear part of the measurement as a function of the tube current. The course of the slope dependent on the tube current differs from the one in figure 5.4.1(b). The data is shown with uncertainties which are smaller than the size of the data points. The uncertainties were determined by the error of the fit parameters.

5.5 Tube voltage variation

This section examines the response of the Dosepix-ionization-chamber to x-ray tube voltage variation. Data is taken in Integration-mode with a frame time of 0.5 s. The bias voltage is kept constant at 2 kV and the tube current is 20 mA. The used tube voltages are in the range between 40 kV and 100 kV in steps of 10 kV. Figure 5.5.1 shows the corresponding measurements which were taken directly after each other starting with the smallest tube voltage. The course of the data is similar to the one in figure 5.2.5, where the response of the Dosepix-ionization-chamber to long exposure times was investigated. The position of the maxima occurs after fewer frames with increasing tube voltage. This behavior can be explained by the higher flux increasing the number of deflecting electrons on the ASIC. The value of iToT increases until a tube voltage of 60 kV. For higher tube voltages, the iToT value decreases with increasing tube voltage. This is due to the time dependency, which was investigated in section 5.2. The maximum is reached very late for a voltage of 40 kV. For tube voltages 50 kV and above, the peak positions are determined

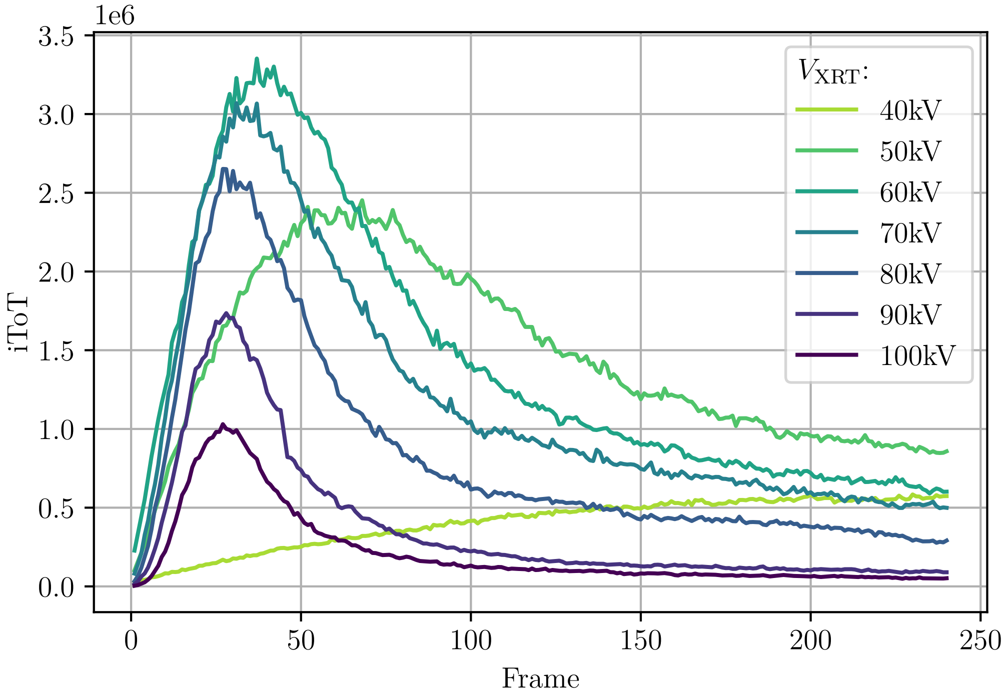

Figure 5.5.1: Integrated ToT value as a function of time, represented by the frame index, for different tube voltages. The tube current is 20 mA and the bias voltage 2 kV. The maximum is reached faster with increasing tube voltage. iToT becomes smaller with increasing tube voltage because of the time dependency.

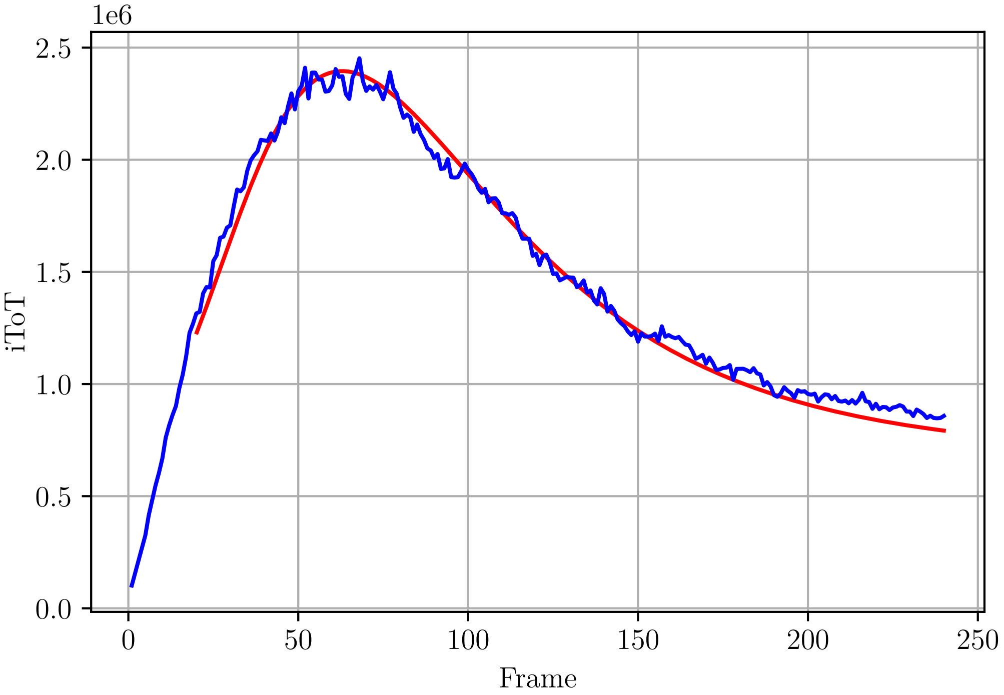

Figure 5.5.2: Moyal function fitted to the measurement at a tube voltage of 50 kV.

via a fit of a Moyal function onto the data to further investigate the dependency of the maximum on the tube voltage. Exemplary, figure 5.5.2 shows the fit for the measurement at a tube voltage of 50 kV. The Moyal-function is described via ([KW16]):

$$f(x) = a \cdot \exp\left(-\frac{1}{2}\left(\frac{x-b}{c} + \exp\left(-\frac{x-b}{c}\right)\right)\right) + d \tag{5.5.1}$$

Here, a corresponds to the amplitude, b is the peak position, c the width, and d the offset of the function. Figure 5.5.3 shows the peak positions of the curves as a function of the tube voltage. The peak for the measurement for a bias voltage of 50 kV appears after a long measurement time, for 40 kV, the maximum is not even clearly reached within 240 frames. However, this could also result from the time dependency of the measurements since it takes time for the electrons to gather on the ASIC. From 60 kV up to 90 kV, a nearly linear course is observed. The difference of the peak positions at 90 kV and 100 kV is marginal. It is also possible that the measured behavior of the peak positions dependent on the tube voltage results from the time dependency since the peak positions are expected earlier if more measurements were performed before because of more collected electrons on the insensitive part of the ASIC.

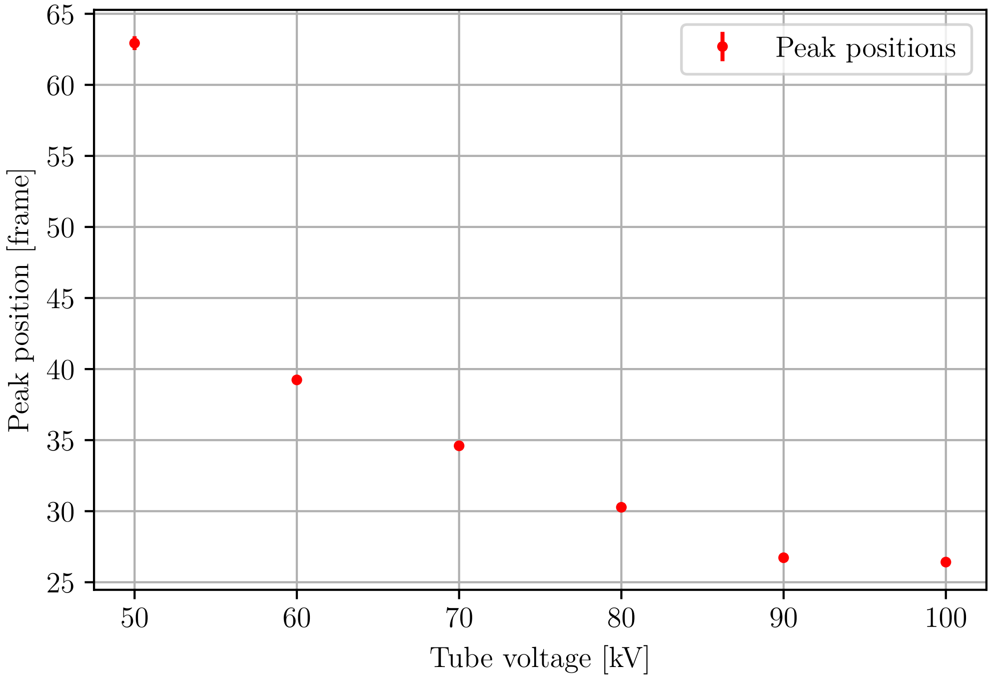

Figure 5.5.3: Peak positions of the measurements in figure 5.5.1 as a function of the tube voltage. The peak position appears quicker for increasing tube voltage. The uncertainties were determined by the error of the fit parameters.

Even though a dependency of the peak positions on the tube voltage is observed, it is difficult to extract valuable results because of the huge time dependency.

5.6 Response to clinical electrons

In this section, the response of the Dosepix-ionization-chamber to electrons is discussed. The measurements are performed with the VersaHD by Elekta ([Ver]) at the Strahlenklinik Erlangen ([Strb]). This LINAC uses the technique of traveling waves. The functionality of LINACs is explained in chapter 2.3.2. The electron energy is 6 MeV and the energy dose is 10 Gy per 100 monitor units (MU) in water at a distance of 1 m from the focus spot. The used dose rate is 250 MU/min. Measurements are performed with 50 MU. The distance between the focus spot and the Dosepix-ionization-chamber is approximately 110 cm. As for the measurements with the x-ray tube, they are performed from the side of the Dosepix-ionization-chamber, as shown in figure 5.0.2. A bias voltage variation measurement series is carried out as discussed in section 5.1. For this, the bias voltages 0 V, 200 V, 500 V,

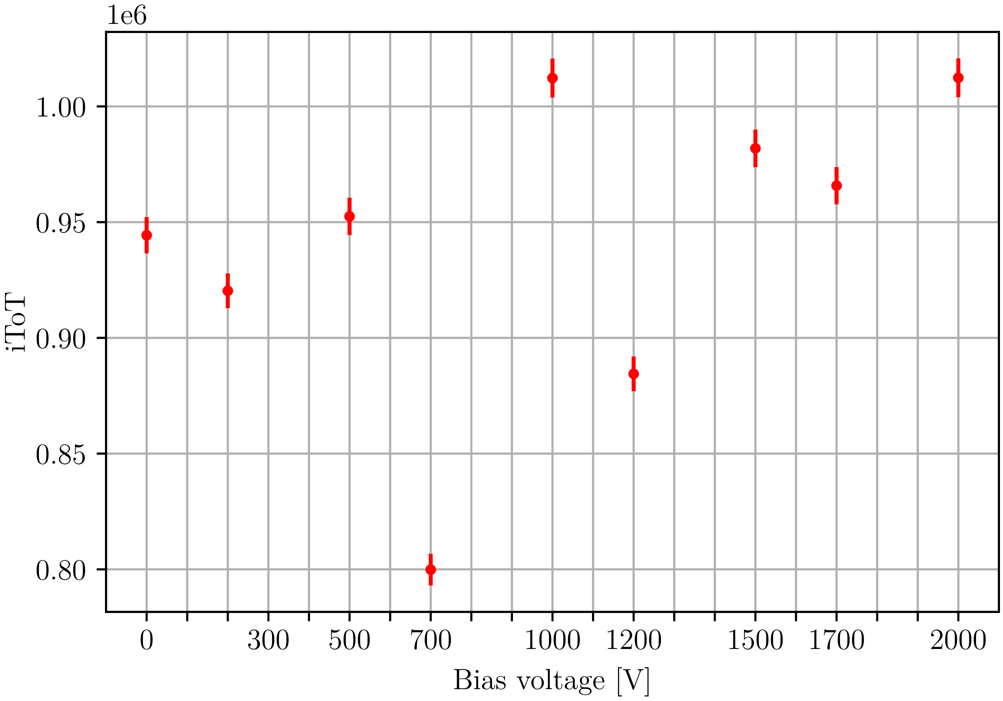

Figure 5.6.1: Value of iToT as a function of the bias voltage. No course is observed, and the iToT values are small. The Dosepix-ionization-chamber does not reach the state of registering events because of time dependency. The uncertainties are calculated by Gaussian error propagation of the standard deviation of the iToT value over all pixels within one frame.

700 V and the bias voltages between 1000 V, 1200 V, 1500 V, 1700 V and 2000 V are applied. Dosepix was utilized in Integration-mode with 40 frames with a frame time of 0.5 s. Since no events were measured the first time, the lead layer in front of the ASIC was removed as it might already cover too much of the air volume between the ASIC and the metal plate. Figure 5.6.1 shows the iToT values as a function of the bias voltage. The value of iToT is calculated by summing up all values registered within one measurement. For every pixel, the standard deviation is determined, yielding one value for each pixel. Subsequently, the uncertainties on the iToT value are determined by Gaussian error propagation. The iToT value does not rise with increasing bias voltages like observed in figure 5.1.1, and the measured iToT values are small. This leads to the assumption that the population of electrons on the insensitive part of the ASIC produced by the provided radiation is too small to register events, as it was investigated in section 5.2. Longer radiation times are not possible because of the technical limitations of the devices. Measured

events most likely result from radiation that hits the ASIC directly. It is shown that the Dosepix-ionization-chamber is not suitable for clinical applications since the registration of events only starts if enough electrons are collected on the surface of the ASIC.

5.7 Conclusion

In this chapter, the feasibility of an ionization chamber consisting of a Dosepix detector without sensor element was investigated. The Dosepix-ionization-chamber utilizes a Dosepix ASIC and a copper plate, at which a negative voltage is applied. Secondary electrons produced by the primary radiation are accelerated towards the ASIC and produce a charge signal.

At first, the response of the Dosepix-ionization-chamber to different bias voltages is investigated, yielding an exponential trend. All subsequent measurements were performed with a bias voltage of 2 kV. The time dependency of the iToT values was investigated, which showed that the values change with time. A possible reason for this behavior are electrons collected on the insensitive part of the ASIC, deflecting secondary electrons produced by the irradiation towards the sensitive part of the pixels resulting in changing iToT values with time. This causes severe problems in the reproducibility. Two trivial approaches were tested to solve the issue. The first one is turning off the voltage supply, and the second one is turning off the voltage supply and removing the USB plug from the Dosepix-board. Both approaches did not solve the problem. Additionally, the response of the Dosepix-ionization-chamber on different tube currents and tube voltages is investigated. For the tube current variation, it was found that the slope of the linear part of the curves showing the iToT value as a function of time, represented by the frame index, is steeper for increasing tube currents for most measurements. However, no reproducible results are obtained. For the tube voltage variation, the maximal iToT value was found to occur quicker for larger tube voltages. Finally, measurements were performed in the Strahlenklinik Erlangen [Strb]. No rise of the iToT value dependent on the bias voltage was observed leading to the assumption that the Dosepix-ionization-chamber only starts to measure secondary particles for long irradiation times.

Overall, it has to be concluded, that the Dosepix-ionization-chamber in its current state does not allow a proper functioning as an ionization chamber. Far more elaborate approaches must be considered. Electric field simulations and analysis must be conducted to construct a feasible design.

The strong time dependency prevents the operation of the Dosepix-ionization-chamber from execution of dosimetric tasks. Therefore, a different method to measure high-flux radiation is needed. In the following chapter, the effective sensor thickness is reduced in the conventional setup.

6 Reduction of the effective sensor thickness

Contents

In FLASH radiotherapy dose rates up to several Gy/s are used ([RSM+20]). Dose rates in the order of tens of Sv/h in pulsed photon fields already show a significant influence of pile-up in the Dosepix detector equipped with a 300 µm silicon sensor as presented in [HSH+22] and [ZAB+15]. For ultra large dose rates a neural network based analysis for the three Dosepix detector setup showed promissing results in dosimetry [Huf22]. A setup consisting of a single Dosepix detector is utilized for FLASH radiotherapy. In the following, different ways of operating the detector are analyzed.

A detector setting enabling the operation in high particle flux environments must be determined. One way to deal with this issue is to reduce the bias voltage of the silicon sensor of the Dosepix detector from the default value of 100 V for a three detector setup or 48 V for an one detector setup. Full depletion of the silicon sensor occurs at a bias voltage of 12 V as shown in [Ull21]. Therefore, applying a bias voltage below 12 V will result in an effective sensor thickness smaller than the actual 300 µm sensor thickness. A reduction of the effective thickness directly impacts the detection volume, hence, a reduction of the event rate is expected. This in turn reduces the pile-up occurrence rate.

At the beginning of this chapter, the choice of I_{krum} is examined. Then, the response of Dosepix as a function of the bias voltage is investigated for different kinds of particles. First, irradiation with photons is performed. The sources are a x-ray tube and ^{241}Am. Furthermore, ^{241}Am is also used to examine the detectors response to alpha particles. Finally, ^{90}Sr/^{90}Y is used for the irradiation with electrons.

6.1 Choice of I_{krum}

I_{krum} is an adjustable current proportional to the current which decreases the charge signal after the charge sensitive amplifier. Determining a suitable value for I_{krum} is necessary since I_{krum} has a direct impact on pile-up. For large values of I_{krum}, the charge signal of the CSA decreases faster. Consequently, the probability for pile-up increases for small values of I_{krum}. This leads to problems in FLASH radiotherapy since dose rates of several Gy/s are used ([RSM^{+}20]). ToT-spectra of the detector response to the gamma decay line of ^{241}Am with an energy of 59.54 keV ([Nuc]) are recorded to investigate the impact of I_{krum}. The peak in the spectra corresponds to the full-energy-peak of the ^{241}Am-photons. The peaks are shifted to smaller ToT-values with increasing I_{krum} because of the faster decrease of the charge signal

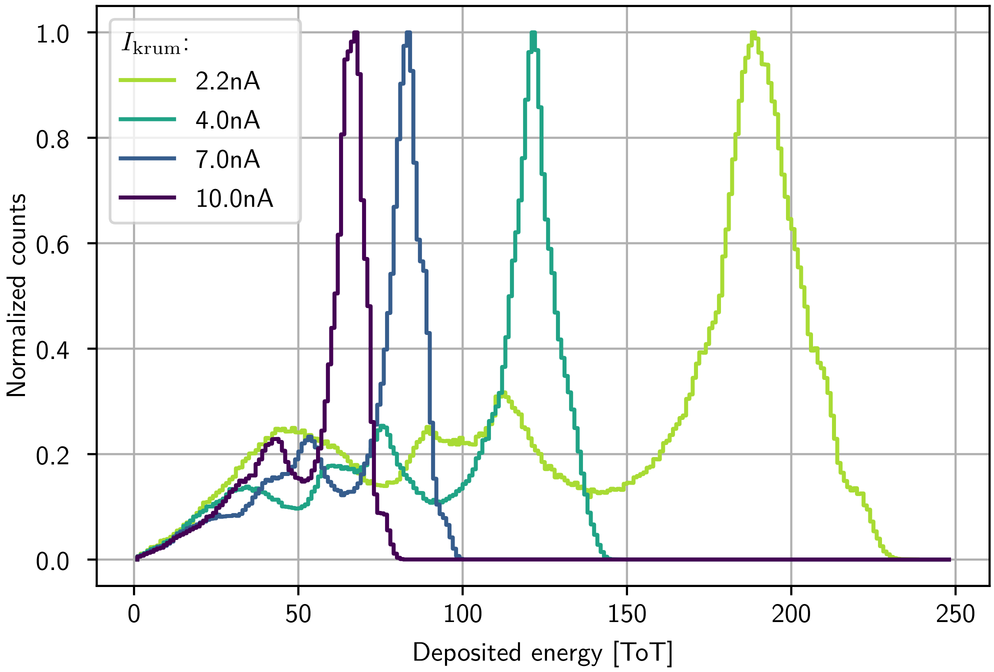

Figure 6.1.1: Energy deposition spectra recorded in ToT-mode at different values of I_{krum}. The source is ^{241}Am emitting monoenergetic photons with an energy of 59.54 keV. The ToT-values decrease with rising I_{krum} which suppresses pile-up. However, the energy resolution becomes worse at high values of I_{krum}.

of the charge sensitive amplifier. For all investigated values of I_{krum}, all important features of the energy deposition spectrum is visible so a choice of a relatively high I_{krum} is justified. In all following measurements, I_{krum} is set to 7 nA.

6.2 Detector response to photons

In this section, the response of Dosepix to photons is investigated. Two different photon sources are used: a x-ray tube and a ^{241}Am-source. First, Dosepix' response to x-rays is examined.

6.2.1 Detector response to x-rays

Dosepix' response to x-rays under variation of bias voltage and the photon flux is investigated in the following. Irraditions are performed with the MEGALIX CAT PLUS 125/20/40/80-122GW ([MEG]). The x-ray tube current is varied resulting in different photon fluxes where the photon flux is proportional to the tube current ([Stra]). The applied tube currents are 1 mA, 2 mA, 5 mA, 10 mA, 20 mA, 30 mA, 40 mA and 50 mA. The tube voltage is held constant at 40 kV. I_{krum} is set to 7 nA. The smallest applied bias voltage V_{bias} is 300 mV. The bias voltages up to $V_{\mathrm{bias}} = 20\,\mathrm{V}$ are used, for voltages $V_{\mathrm{bias}} < 1\,\mathrm{V}$ in steps of $\Delta V_{\mathrm{bias}} = 100\,\mathrm{mV}$ and for voltages $V_{\mathrm{bias}} > 1\,\mathrm{V}$ in steps of $\Delta V_{\mathrm{bias}} = 1\,\mathrm{V}$. An energy calibration is required for every bias voltage, which is discussed in section 4.2. The distance between the detector and the focus spot of the x-ray tube is about 60 cm.

Dosepix is operated in ToT-mode allowing the investigation on the change of the shape of the energy deposition spectra with respect to variation of the bias voltage. Figure 6.2.1 shows measurements for different bias voltages. Each panel of the figure demonstrates a measurement series with different tube currents. For high bias voltages, at which the sensor is fully depleted, the maximum of the spectra is dependent on the tube current I_{XRT}. At high tube currents, the maxima are shifted towards smaller energies in comparison to small tube currents. A threshold shift occurs at high photon fluxed as demonstrated in [Sch21]. The maximum energy of the photons is 40 keV since a tube voltage of 40 kV is applied. Pile-up is investigated at entries in the histograms of the energy deposition spectra above 40 keV. It has to be noted that photons with the maximal energy of 40 keV can also be registered at higher energies because of the energy resolution of Dosepix. The standard deviation of the energy resolution is approximately 1.2 keV under the assumption of Gaussian smearing ([Cora]). For small bias voltages, the energy deposition spectra do not change with different tube currents. Here, pile-up is suppressed because of the smaller effective sensor thickness resulting in less detected

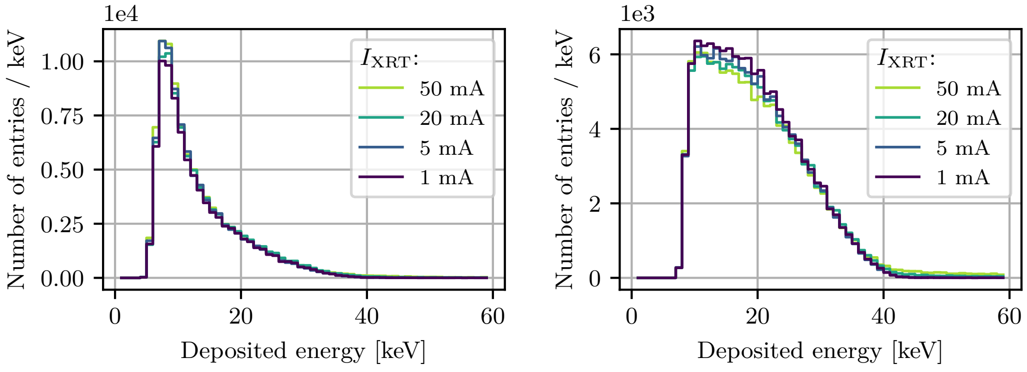

(a) $V_{\mathrm{bias}} = 0.3\,\mathrm{V}$ (b) $V_{\mathrm{bias}} = 1\,\mathrm{V}$

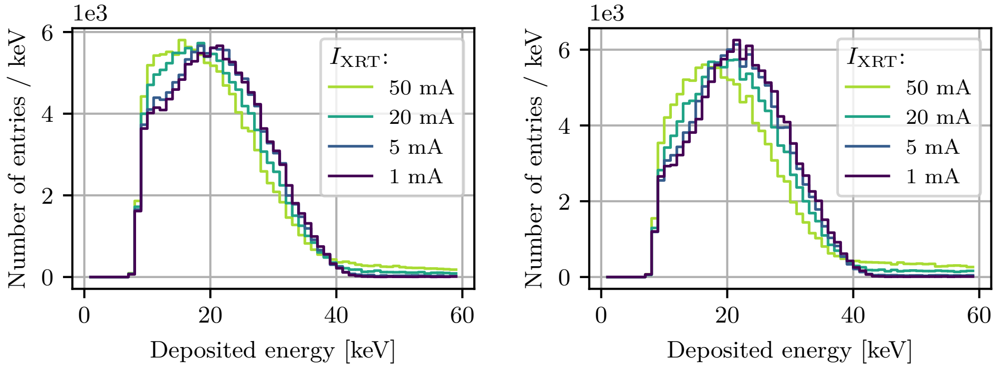

(c) $V_{\mathrm{bias}} = 6\,\mathrm{V}$ (d) $V_{\mathrm{bias}} = 20\,\mathrm{V}$

Figure 6.2.1: Comparison of measurements with different tube currents in ToT-mode for the bias voltages (a): 0.3 V, (b): 1 V, (c): 6 V and (d): 20 V. I_{krum} is set to 7 nA and the tube voltage is 40 kV. A change of the bias voltage shows differences in the shape of the energy deposition spectra. Additionally, an increase of the tube current also leads to a change of the shape of the energy deposition spectra.

particles.
Figure 6.2.2(a) shows measurements with a tube current of 1 mA at varying bias voltages. The shape of the energy deposition spectra show a dependence on the applied bias voltage to the sensor. Additionally, a shift of the maximum of the energy deposition spectra to smaller energies with decreasing bias voltage is observed. Figure 6.2.2(b) corresponds to the data with a tube current of 50 mA at varying bias voltages. Also at high tube voltages, the dependence of the shape of the energy deposition spectra as a function of the bias voltage is observed. For small bias

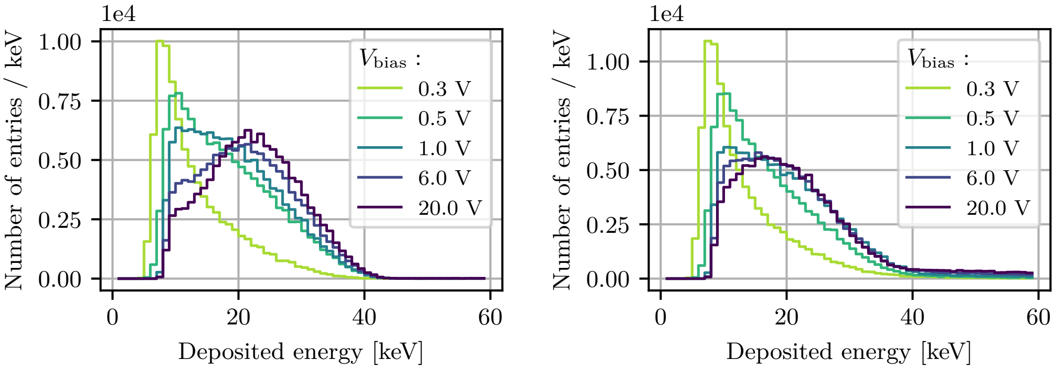

(a) $I_{\mathrm{XRT}} = 1\,\mathrm{mA}$

(b) $I_{\mathrm{XRT}} = 50\,\mathrm{mA}$

Figure 6.2.2: Comparison of measurements with different bias voltages in ToT-mode for the tube currents (a): 1 mA and (b): 50 mA. I_{krum} is set to 7 nA and the tube voltage is 40 kV. The deposition spectra are dependent on the bias voltage.

voltages up until 1.0 V, the spectra look similar to the ones in figure 6.2.2(a). The shape of the energy deposition spectra change at higher bias voltages in comparison to figure the data at a tube current of 1 mA as already shown in figure 6.2.1. Pile-up is visible at high tube voltages as events are registered above 40 keV. Pile-up is reduced at small bias voltages since the number of events decreases with decreasing bias voltages. The dependence of the shape of the energy deposition spectra on the applied bias voltage can be corrected by conversion factors for dosimetric applications. The shape of the spectra is dependent on the bias voltage. In figure 6.2.2(b), the tail of the spectra at high energies show a stronger pile-up for large bias voltages. As a first result, pile-up is strongly reduced by applying small bias voltages to the sensor which could be a method to measure radiation with high fluxes.

Next, Dosi-mode is utilized to record energy deposition spectra in 16 energy bins allowing the investigation of the count rate dependency. The measurement time is approximately 110 s. The used bin edges are chosen from 10 keV until 85 keV in steps of 5 keV. In figure 6.2.3, each panel shows measurements for different bias voltages at the same tube current. For a better overview, only a few bias voltages are shown and the regarded tube currents are 1 mA and 50 mA. Figure 6.2.3(b) and (d) show the logarithmic representation of figures 6.2.3(a) and (c), respectively. The event rate is lower for smaller bias voltages since the effective sensor thickness is reduced. Additionally, the shape of the energy deposition spectrum depends on the bias voltage which was already seen in figure 6.2.2. Especially for the measurements

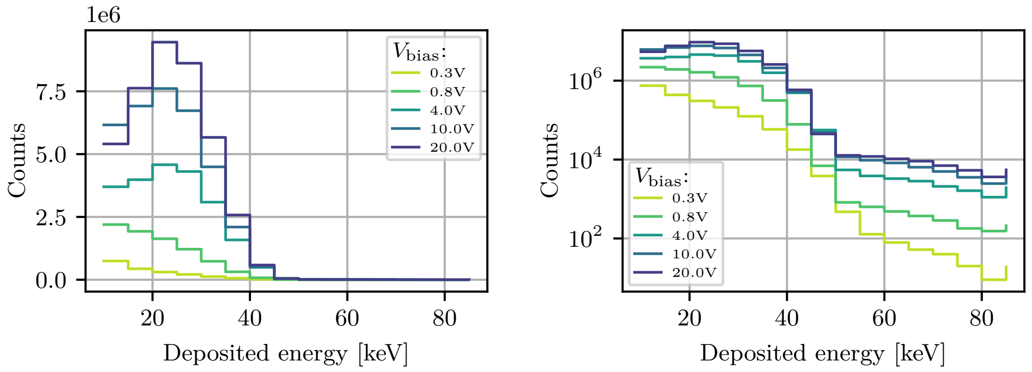

(a) $I_{\text{XRT}} = 1\,\text{mA}$

(b) $I_{\text{XRT}} = 1\,\text{mA}$

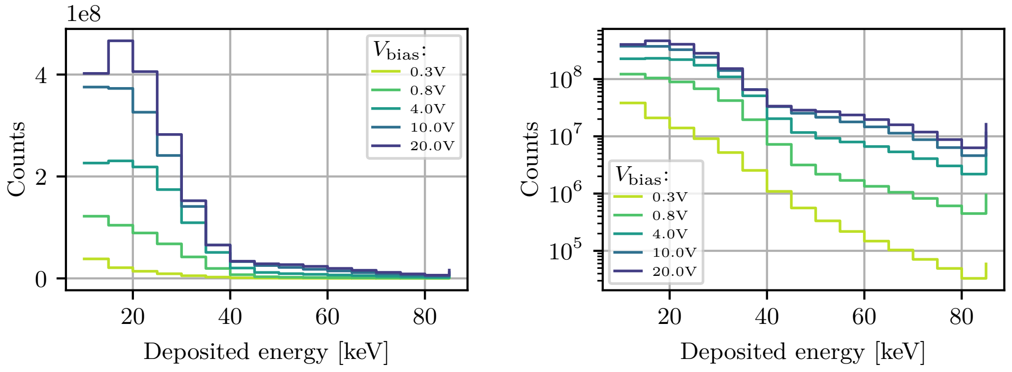

(c) $I_{\text{XRT}} = 50\,\text{mA}$

(d) $I_{\text{XRT}} = 50\,\text{mA}$

Figure 6.2.3: Comparison of measurements with different bias voltages in Dosi-mode for the tube currents (a): 1 mA and (c): 50 mA. Plots (b) and (d) show the logarithmic representation of (a) and (c), respectively. I_{krum} is set to 7 nA and the tube voltage is 40 kV. Pile-up and the event rate are reduced at small bias voltages.

with a tube current of 50 mA, pile-up is reduced at small bias voltages, since the count rate above 40 keV is much smaller than at high bias voltages. In figure 6.2.4, each panel shows measurements at different tube currents at a fixed bias voltage. Figures 6.2.4(b) and (d) are the logarithmic representations of figures 6.2.4(a) and (c), respectively. Comparing figure 6.2.4(a) and 6.2.4(c), the measured spectra change with different bias voltages. Figures 6.2.4(b) and 6.2.4(d) show that the ratio between the event rate of different tube currents at high energies exceeding 40 keV is higher for bigger bias voltages than for small ones. This means that pile-up is suppressed stronger for small bias voltages in comparison to large ones. In order to investigate the reduction of pile-up at small bias voltages compared to large ones, the ratio between the registered events above 40 keV and the total number of events within one measurement is calculated for the bias voltages of 0.8 V and 20 V at all investigated tube currents. A bias voltage of 0.8 V was chosen for this investigation since at smaller bias voltages, the energy calibration becomes inaccurate. The uncertainty is calculated via Gaussian error propagation of the uncertainties of the number of events determined by Poisson statistics. Figure 6.2.5 shows the calculated ratios as a function of the tube current. A linear fit of the form $f(x) = a \cdot x + b$ is applied to the measured ratios. The measurement series with a bias voltage of 20 V shows a larger fraction of pile-up as the measurements at 0.8 V. The difference of the calculated ratios between the two investigated bias voltages increases at higher tube currents, i.e. higher photon fluxes. At a tube current of 50 mA, the ratio between pile-up events and the total number of events is almost 10% at a bias voltage of 20 V, compared to approximately 4% at 0.8 V. It must be mentioned that measured events which are not influenced by pile-up are potentially stored in the energy bin with the range of 40 keV to 45 keV because of the standard deviation of the energy resolution of the detector of about 1.2 keV at assumption of Gaussian smearing ([Cora]). The determined fit parameters are $a = (0.00064 \pm 0.00005)\,1/\text{mA}$ and $b = 0.0094 \pm 0.0013$ for a bias voltage of 0.8 V and $a = (0.00158 \pm 0.00006)\,1/\text{mA}$ and $b = 0.0170 \pm 0.0014$ for a bias voltage of 20 V.

The total number of registered events for the large pixels is calculated via the sum of entries over all pixels for different bias voltages. An analysis of the curve allows the investigation of the saturation of the event rate. This is done for multiple tube currents in figure 6.2.6(a). The measurements were performed in the following way. At was started with the highest bias voltage of 20 V and the highest tube current of 50 mA. First, the tube current was varied to smaller values. When the measurement at the smallest tube current of 1 mA was finished, the bias voltages was changed to the next smaller value. Subsequently, the tube current was varied from large to small values again.
No clear saturation is observed until a bias voltage of 20 V. The measurements at

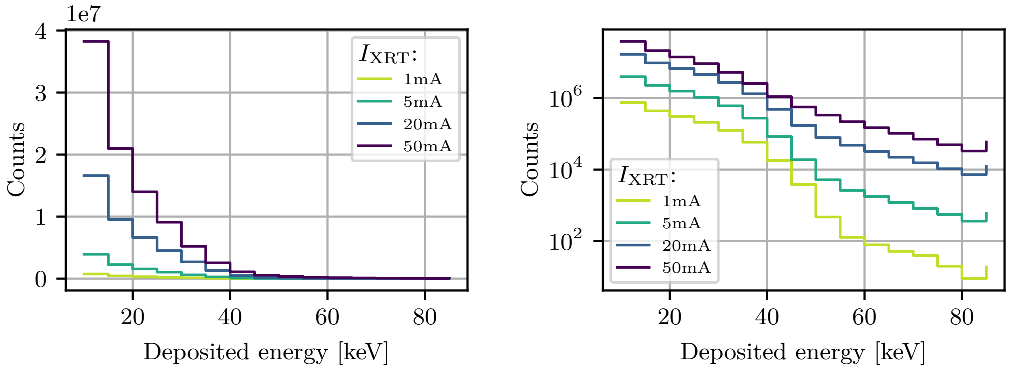

(a) $V_{\mathrm{bias}} = 0.3\,\mathrm{V}$ (b) $V_{\mathrm{bias}} = 0.3\,\mathrm{V}$

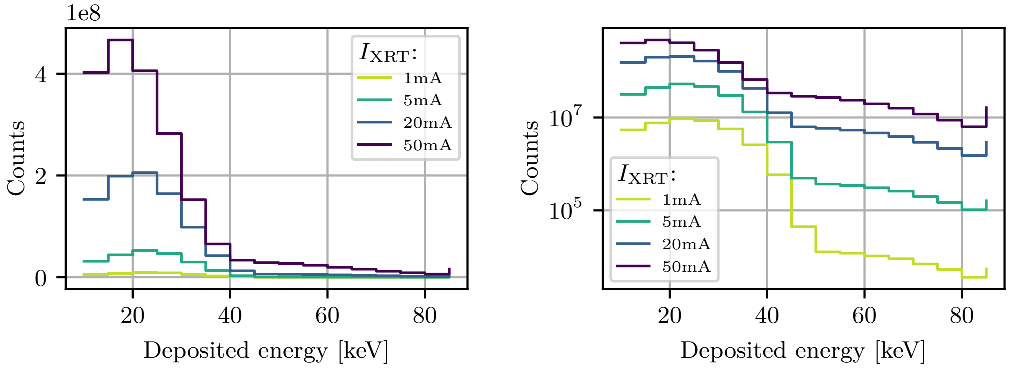

(c) $V_{\mathrm{bias}} = 20\,\mathrm{V}$ (d) $V_{\mathrm{bias}} = 20\,\mathrm{V}$

Figure 6.2.4: Comparison of measurements with different tube currents in Dosimode for the bias voltages (a): 0.3 V and (c): 20 V. Plots (b) and (d) show the logarithmic representation of (a) and (c), respectively. I_{krum} is set to 7 nA and the tube voltage is 40 kV. Pile-up and the event rate are reduced at small bias voltages.

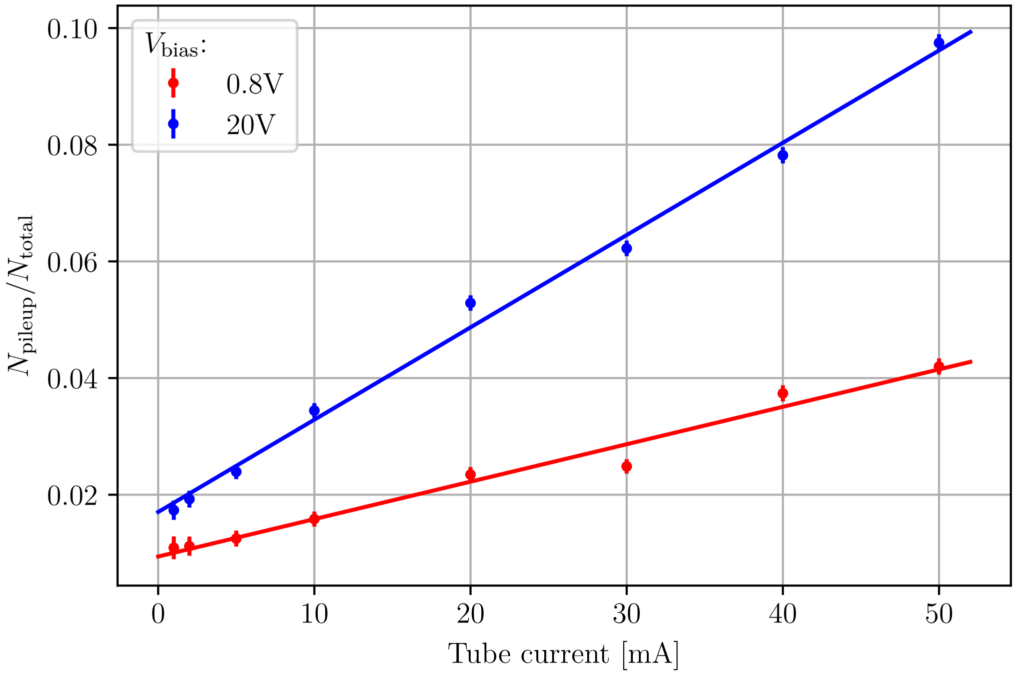

Figure 6.2.5: Determined ratios between the registered events above 40 keV (N_{pileup}) and the number of total events (N_{total}) for the bias voltages 0.8 V and 20 V. Pile-up is reduced at small bias voltages, especially for large photon fluxes. The uncertainties are determined by Gaussian error propagation of the uncertainties of the number of events determined by Poisson statistics.

9 V do not match the rest of the curve. However, these are the first data taken on that day, so it may be possible that the x-ray tube applies a higher current as in the settings and adjusts the current via the tube current regulation in the next measurements. Another disagreement is visible at 15 V. Here, the total counts are less than expected.

In figure 6.2.6(b), the total counts are shown as a function of the tube current. A linear course is expected. The results show a curve with two visible slopes with a change at 20 mA. A reasonable explanation is that a change of settings of the x-ray tube occurs at 20 mA. So, it can also be seen in Dosi-mode that for measurements with high flux radiation better results can be gained with small bias voltages because of the reduced event rate which suppresses pile-up.

The Integration-mode is used in the following. The frame time is set to 1 s and 60

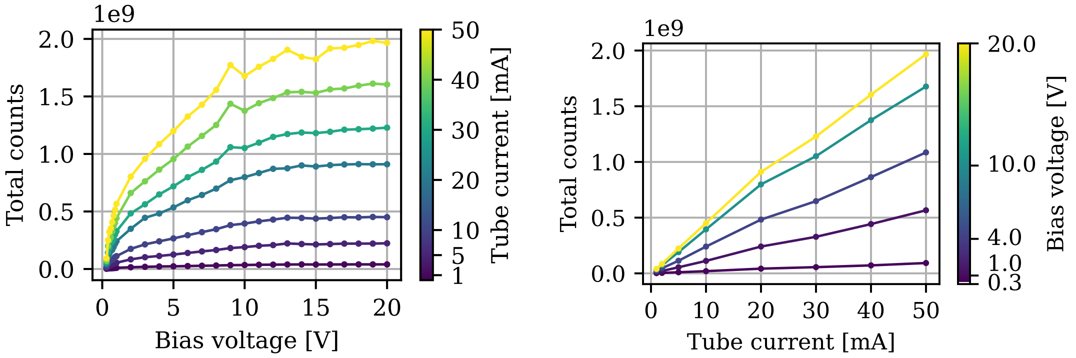

(a) Total counts as a function of the bias voltage (b) Total counts as a function of the tube current

Figure 6.2.6: Number of registered events summed over all large pixels as a function of (a) the bias voltage and (b) the tube current. The measurements are performed in Dosi-mode. Complete depletion of the sensor cannot be observed. Change in course occurs at 9 V in (a) and at 20 mA in (b).

frames are taken per measurement. In figure 6.2.7, the iToT values are shown as a function of the bias voltage and the tube current, respectively. The uncertainties are calculated by the standard error over all frames for each pixel, followed by an Gaussian error propagation over all pixels. The courses look similar to the ones obtained in Dosi-mode. The total number of registered events rise with increasing bias voltage and no clear saturation occurs. Again, a change in course is observed at a bias voltage of 9 V. For the investigation of the total number of events as a function on the tube voltage, a change in slope is observed at 20 mA. For smaller and larger tube currents, the expected linear course holds.

In the following, the disagreement at 9 V is further investigated. Therefore, five measurements are taken at $V_{\mathrm{XRT}} = 40\,\mathrm{kV}$ and $I_{\mathrm{XRT}} = 50\,\mathrm{mA}$ directly after starting the x-ray tube. The measurements were performed in Integration-mode with a measurement time of approximately 30 s. The bias voltage was set to 100 V. In figure 6.2.8, all iToT values are summed up over all pixels and shown as a function on the measurement index. The iToT values are nearly the same for the first two measurements but then clearly decrease for the next ones. This means that the x-ray tube produces larger particle fluxes in its first shots. This is a possible explanation for the change in course at $V_{\mathrm{bias}} = 9\,\mathrm{V}$. To validate this, another measurement series from $V_{\mathrm{bias}} = 8\,\mathrm{V}$ until $V_{\mathrm{bias}} = 10\,\mathrm{V}$ at $V_{\mathrm{XRT}} = 40\,\mathrm{kV}$ and $I_{\mathrm{XRT}} = 50\,\mathrm{mA}$ is performed. At all three bias voltages, a measurement is performed in Integration-mode with a measurement time of approximately 30 s. The result is shown in figure 6.2.8(b). It can be observed that there is no peak at 9 V, so

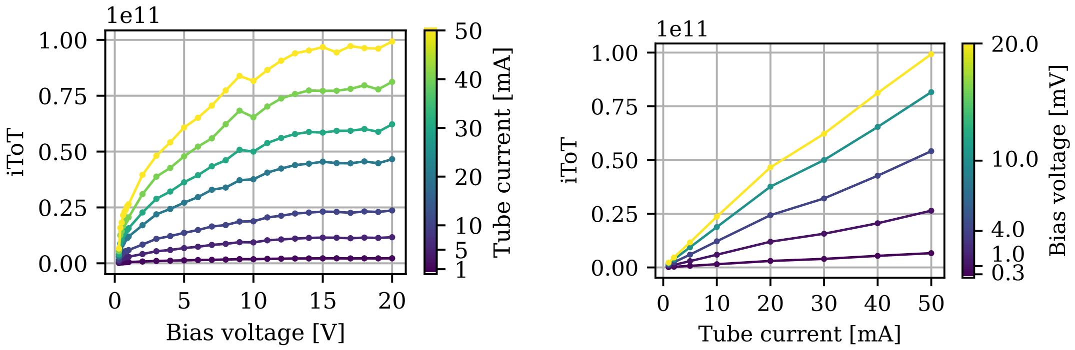

(a) iToT as a function of the bias voltage

(b) iToT as a function of the tube current

Figure 6.2.7: Value of iToT as a function of (a) the bias voltage and (b) the tube current. The measurements are performed in Integration-mode. Complete depletion of the sensor cannot be observed. Change in course occurs at 9 V in (a) and at 20 mA in (b). The uncertainties are calculated by the standard error over all frames for each pixel, followed by an Gaussian error propagation over all pixels.

it can be concluded that the peak at 9 V in figure 6.2.6(a) and in figure 6.2.7(a) result from a problem in the x-ray tube leading to decreased particle fluxes with increasing measurement index. This might also be the reason for the saturation not to clearly occur since the measurements series were started at the highest bias voltage, proceeding to smaller ones.

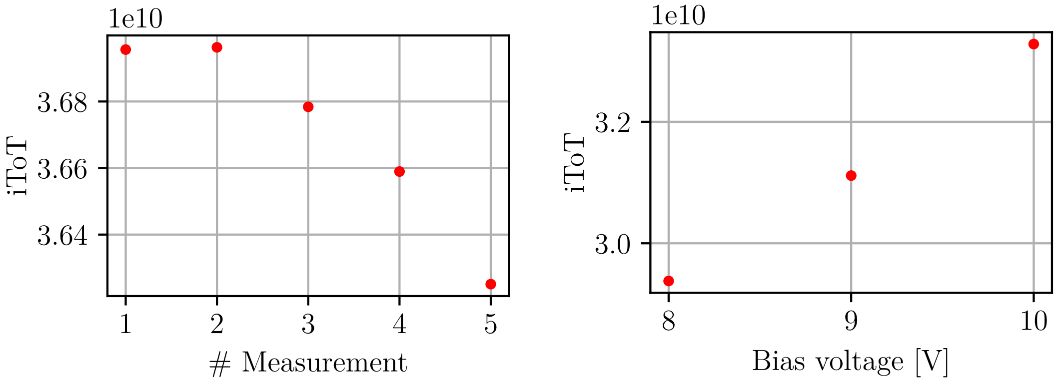

(a) Measurement taken after each other

(b) Course around $V_{\text{bias}} = 9\,\text{V}$

Figure 6.2.8: (a) shows the iToT value as a function on the measurement index. Five measurements were performed after each other after starting the x-ray tube. (b) shows the iToT value of the measurements at the bias voltages 8 V, 9 V, 10 V measured directly after each other. The measurements are performed in Integration-mode with a measurement time of approximately 30 s. The iToT values start to decrease after the second measurement which is probably the reason for the change in course at a bias voltage of 9 V because of different measurement days between 9 V and 10 V. This change in course vanished when the measurements between 8 V and 10 V are performed directly after each other. The uncertainties are calculated by the standard error over all frames for each pixel, followed by an Gaussian error propagation over all pixels. The uncertainties are smaller than the size of the data points.

6.2.2 Detector response to monoenergetic photons

In addition to the investigation of the response of Dosepix to x-ray spectra when varying the bias voltage, irradiation is performed with an ^{241}Am-source. The key difference between both sources is the shape of the incident spectra. X-ray spectra are broad in nature while gamma decay results in monochromatic radiation. The ^{241}Am radionuclide is shielded at its exit window, resulting in the full stoppage of alpha particles. Subsequently, only photons resulting from the corresponding gamma decays, predominantly at 59.54 keV, are observed. Deposition spectra are investigated with ToT-mode whereas Dosi-mode is used to investigate the event rate as a function of the bias voltage. The exposure time is 10 minutes for every measurement. The applied bias voltages are in the range between 0.3 V and 30 V. Between $V_{\text{bias}} = 0.3\,\text{V}$ and $V_{\text{bias}} = 1\,\text{V}$ a step size of $\Delta V_{\text{bias}} = 100\,\text{mV}$ is chosen. Between $V_{\text{bias}} = 1\,\text{V}$ and $V_{\text{bias}} = 20\,\text{V}$, the step size is $\Delta V_{\text{bias}} = 1\,\text{V}$. Additionally, bias voltages 25 V and 30 V are used. I_{krum} is set to 7 nA. Figure 6.2.9 shows the deposition spectra of the ^{241}Am-source for different bias voltages. The deposition spectra after the energy calibration look very similar for the bias voltages 5 V and 20 V. However, at 0.5 V, the peak is not as sharp as for larger bias voltages. At a bias voltage of 0.3 V, the peak is additionally shifted to smaller energies. The bad energy resolution at small bias voltages is caused by the neural network, as described in [Sch21], not finding the optimal parameters for the energy calibration. Figure 6.2.9(a) shows the deposition spectra in ToT. Especially, between 50 and 100 ToT, the deposition spectra show differences at different bias voltages. However, the full-energy peak at a bias voltage of 300 mV is clearly visible. Also, it can be recognized that the ratio between the amplitude of the photo peak to the rest of the spectrum becomes larger with bigger bias voltages. Figure 6.2.10 shows the ratio between the amplitudes of the full-energy peak and the mean amplitude of the whole spectrum from 10 keV to 70 keV as a function of the bias voltage. The amplitude of the full-energy peak is determined by a Gaussian function, without consideration of background radiation, fitted to the data. The function is:

$$f(x) = a \cdot \exp\left(-\frac{(x-b)^2}{c^2}\right) \tag{6.2.1}$$

Here, a corresponds to the amplitude, b and c are the position and width of the peak, respectively. The fit was fitted to the data between 57 keV and 80 keV. The uncertainties are determined by the error of the fit parameters. Since the energy calibration does not determine the optimal values below 0.7 V, the values are not shown for these voltages. For bias voltages up to 5 V, the ratio increases steeply. For higher bias voltages, the slope is smaller but the ratio further rises. The uncertainties were obtained by the error of the fit. In order to explain this behavior, it must be considered that the sensor is depleted from the side of the ASIC. This means that if the sensor is not depleted completely, particles first traverse the part of the sensor that is not depleted before they reach the depleted part where they are detected. If photons interact in the part of the sensor that is not depleted, they lose energy. The probability for small energy contributions in the spectrum rises for smaller bias voltages since the particles traverse more non-detecting material in the sensor. This results in a smaller full-energy peak. This however would lead to the result that the sensor is not fully depleted at 20 V yet. Another possible explanation is charge sharing. The drift velocity rises with increasing bias voltages. This leads to a reduced spread of the radius of the charge cloud. Therefore charge sharing is reduced. The probability that only parts of the full energy of the photons are detected by multiple pixels is higher for small bias voltages which leads to a reduced amplitude.

Next, Dosepix is utilized in Dosi-mode in order to measure the total number of registered events. The exposure time is 10 minutes. All events over all bins were summed up to obtain the total number of events. Figure 6.2.11 shows the number of registered events as a function of the bias voltages. The uncertainties were determined by Poisson statistics, i.e. the square root of the number of registered events. Until 1 V, the event rate rises steeply. The slope becomes smaller at higher bias voltages until saturation occurs at about 13 V implying the sensor to be fully depleted at this bias voltage. This result is in good agreement with [Ull21].

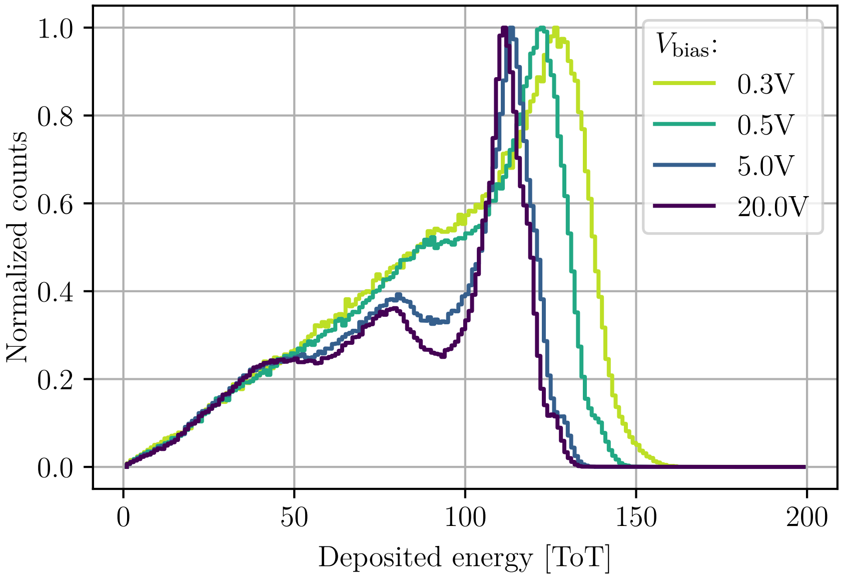

(a) ToT-measurement

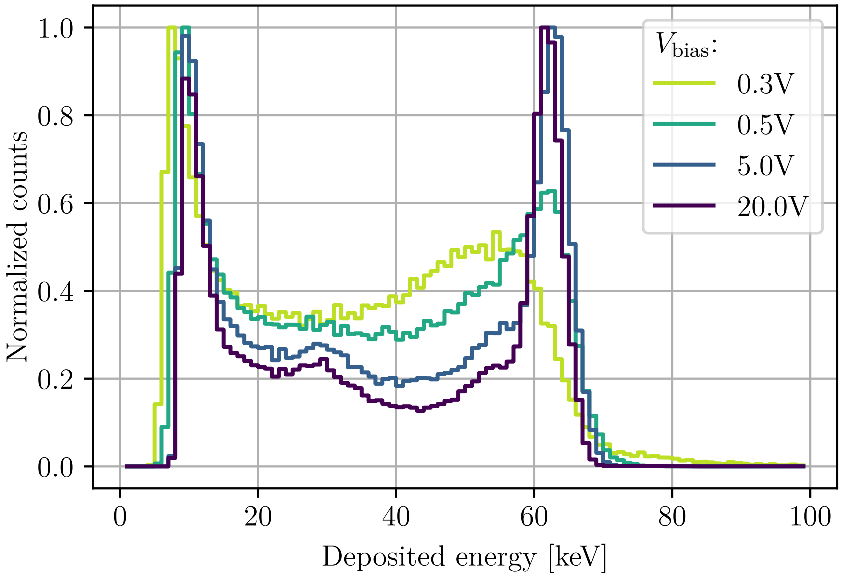

(b) Energy deposition spectra after energy calibration

Figure 6.2.9: ToT-measurements (a) and energy deposition spectra after the energy calibration (b) of the ^{241}Am-gamma source for the bias voltage of 0.3 V, 0.5 V, 5 V and 20 V. I_{krum} is set to 7 nA. The exposure time is 10 minutes. In (a) the full energy peak of the ^{241}Am-photons at a bias voltage of 0.3 V is visible. In (b), the deposition spectra at 0.3 V does not match the real deposition spectra since the neural network did not find the optimal parameters.

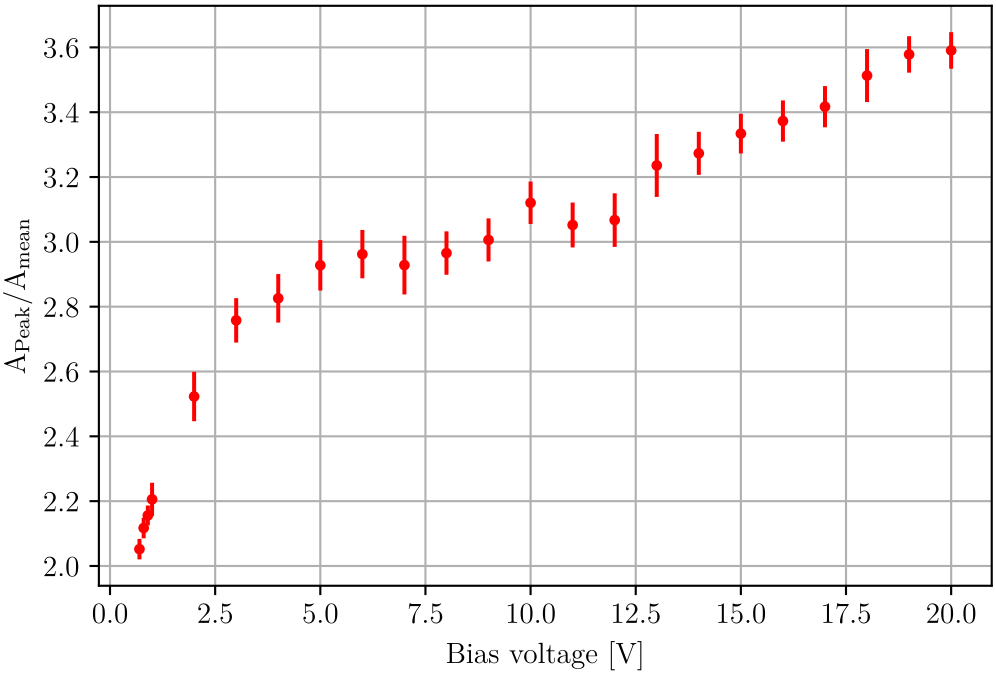

Figure 6.2.10: Ratio between the amplitude of the full-energy peak and the mean amplitude of the whole spectrum as a function of the bias voltage. The ratio increases with larger bias voltages. The uncertainties are determined by the error on the fit parameters.

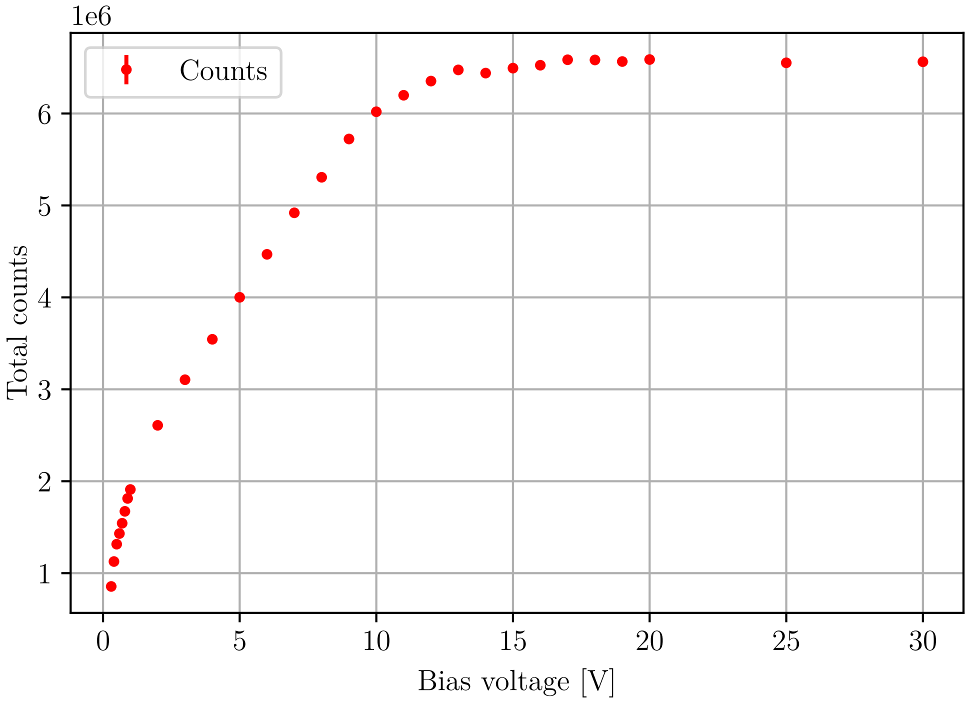

Figure 6.2.11: Number of registered events summed over all large pixels of the ^{241}Am-photon source as a function of the bias voltage. Saturation occurs at about 13 V which corresponds to the bias voltage of full depletion of the sensor. The uncertainties are determined by Poisson statistics.

6.3 Detector response to alpha particles

Since FLASH radiotherapy also uses massive particles, meaning particles with a non-zero rest mass, it is necessary to investigate the response of Dosepix on the irradiation with massive particles. The first massive particles that were used are alpha particles. For this, measurements with an ^{241}Am-source are shown. The variation of the bias voltage is performed in a range from $V_{\text{bias}} = 0.2\,\text{V}$ to $V_{\text{bias}} = 1.1\,\text{V}$ in steps of $\Delta V_{\text{bias}} = 0.1\,\text{V}$. The smallest applied bias voltage is 0.173 V. In the range from $V_{\text{bias}} = 2\,\text{V}$ to $V_{\text{bias}} = 25\,\text{V}$ steps of $\Delta V_{\text{bias}} = 1\,\text{V}$ are used. Additionally, a bias voltage of $V_{\text{bias}} = 30\,\text{V}$ is applied.

ToT-mode is utilized to record an energy deposition spectrum at a bias voltage of 100 V. The measurement time is approximately 14 h and I_{krum} is set to 7 nA. The long exposure time was chosen in order to achieve good statistics. The spectrum is shown in figure 6.3.1. The maximal energy deposited in the detector is about 3 MeV. The initial energy of the alphas is 5.486 MeV. However, the distance between the detector and the source is about 0.7 cm which means that the alphas

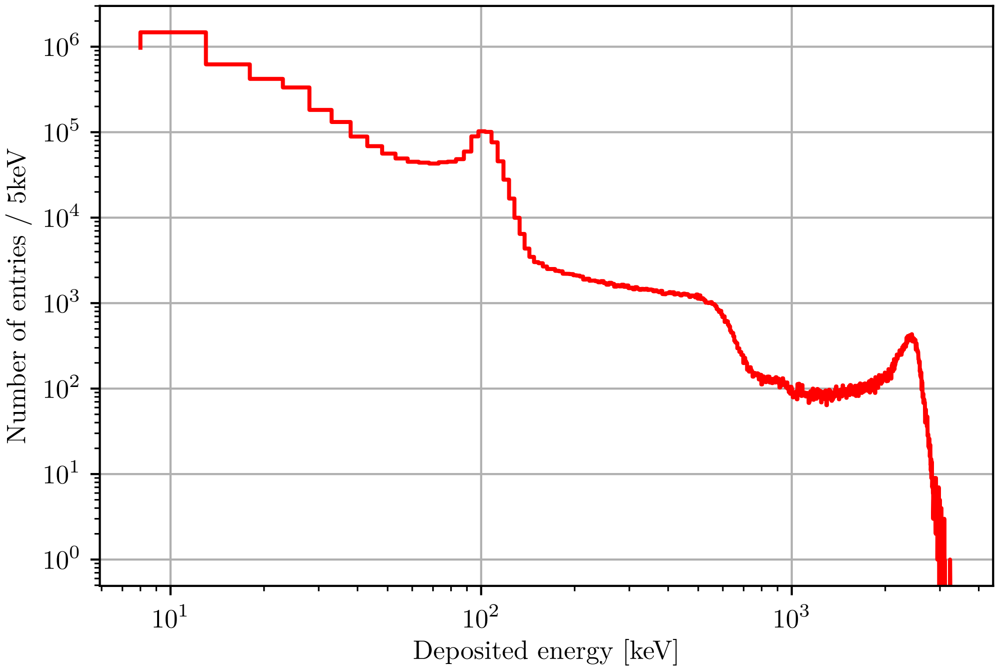

Figure 6.3.1: Deposition spectrum of the ^{241}Am-alpha source at $V_{\text{bias}} = 100\,\text{V}$ and $I_{\text{krum}} = 7\,\text{nA}$. The maximum energy is approximately 3 MeV. Two peaks are visible in the spectrum: At about 2 MeV and at approximately 100 keV. The peak at 2 MeV results most likely from the full energy of the alpha particles.

lose approximately 0.6 MeV on their way to the detector ([NIS]). In this calculation, constant stopping power was assumed. For these measurements, a cover with a hole is used, so the medium between the source and Dosepix is air. This results in an energy of arrival of about 4.9 MeV. Since the alphas are entirely stopped in the silicon sensor, the deposited energy should be 4.9 MeV. A reason as to why no events with this energy are measured could be charge sharing which means that the charge cloud that is produced by the alphas is too large to be registered by only one but by multiple pixels. So each pixel measures only a part of the total deposited energy. Another reason could be that the energy calibration holds no longer true for energies of this order. The calibration is only performed until 60 keV since this is the energy of the used photons. It was not investigated how the relation of ToT and energy behaves in energies of MeV yet. So, it is possible that the relation between the energy and the ToT-values differs with respect to the standard calibration function (see equation 4.2.1) as it was investigated in [SGKP22] which found another dependence on each other in this energy region for Timepix.

Next, the energy deposition spectra of the ^{241}Am-alpha source at different bias voltages are investigated. For every bias voltage, an energy calibration is performed. Figure 6.3.2 shows the recorded energy deposition spectra of the ^{241}Am-alpha source. For this measurement series, no additional bias voltages as the ones shown were used. The ToT spectra were recorded over a time period of 10 minutes. This is sufficient to investigate the dependence of the energy deposition spectra as a function of the bias voltage. The shape of the spectra differs for different bias voltages as it was already seen in figures 4.2.4 and 6.2.2. The dependence of the energy deposition spectra on the bias voltage results from the energy loss of the alpha particles in the part of the sensor that is not depleted which the particles traverse before reaching the sensitive sensor material. So, the change of the deposition spectra is not comparable to the ones of photons because the deposition spectra of photons are primarily affected by charge sharing when changing the bias voltage, whereas alpha particles experience a huge energy loss in the undepleted part of the sensor. Events above an energy of 1 MeV start to be detected at a bias voltage between 2 V and 5 V. Additionally, at rather small bias voltages, there is a peak at about 300 keV which vanishes at higher bias voltages. At $V_{\text{bias}} = 20\,\text{V}$, a kind of plateau can be observed at about 60 keV to 80 keV. This plateau is already visible at smaller bias voltages at smaller energies. However, this plateau corresponds most likely to the peak at about $V_{\text{bias}} = 100\,\text{keV}$ in figure 6.3.1. The expectation would be that the spectra at $V_{\text{bias}} = 20\,\text{V}$ and $V_{\text{bias}} = 100\,\text{V}$ look similar since the sensor is fully depleted or at least nearly fully depleted at $V_{\text{bias}} = 20\,\text{V}$ already as shown in figure 6.3.3. A plausible explanation for this could be that charge sharing is reduced at large bias voltages since the secondary particles are accelerated faster in the sensor which reduces the broadening of the radius of the charge cloud produced by the alpha particles. So, for smaller bias voltages the energy is split up in more energy contributions than for high bias voltages which results in smaller registered energies for smaller bias voltages. Also, in figure 6.3.1, a peak is observed at about 2 MeV which does not occur in figure 6.3.2(f). However, this results from statistics since it is a huge difference in the measurement time between these two measurements. In figure 6.3.2(f), only about 10 events per 7 keV are measured at energies above 1 MeV.

Energy-binning mode spectra are recorded for each bias voltage over the time period of 10 minutes. The total counts are calculated by summing up the number of events registered by the large pixels. The number of registered events as a function of the bias voltage is shown in figure 6.3.3. The uncertainties were calculated via Poisson statistics. Irradiation of the Dosepix detector with alpha particles shows a different course of the total counts compared to irradiations with photons (see figure 6.2.11). The total counts rise very steeply for bias voltages of up to 300 mv. Above that, the course changes at first to an exponential rise. At about 10 V, the rise becomes linear. The total counts start to saturate at about 14 V and is nearly fully saturated at about 17 V. However, the number of events is still slightly rising implying no full depletion of the sensor yet. A reason for the different course of the total counts in comparison to photons could result from the larger effect of charge sharing since the charge cloud produced by alphas is bigger than the one of photons. Besides, in comparison to photons, a different energy deposition is present for alpha particles. Photons interact with the material and produce free electrons which deposit energy in the sensor material whereas alpha particles itself deposit energy in the sensor.

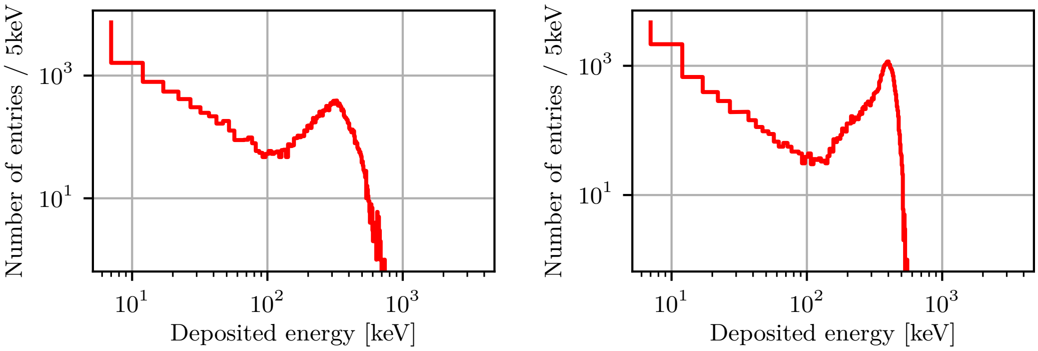

(a) $V_{\text{bias}} = 0.3\,\text{V}$ (b) $V_{\text{bias}} = 1\,\text{V}$

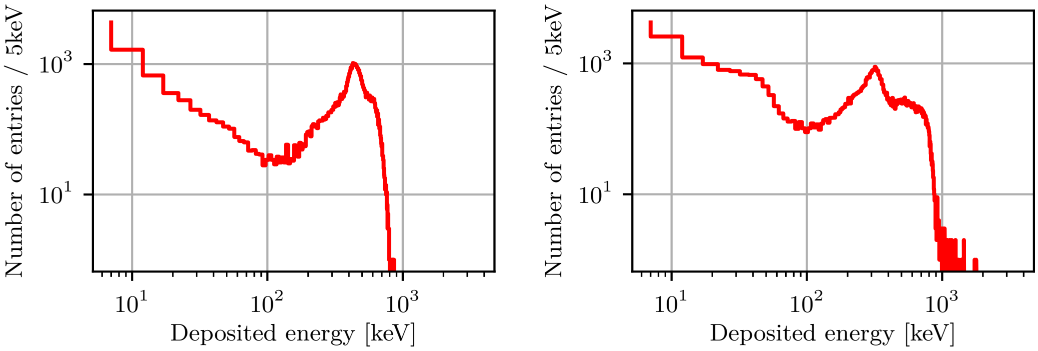

(c) $V_{\text{bias}} = 2\,\text{V}$ (d) $V_{\text{bias}} = 5\,\text{V}$

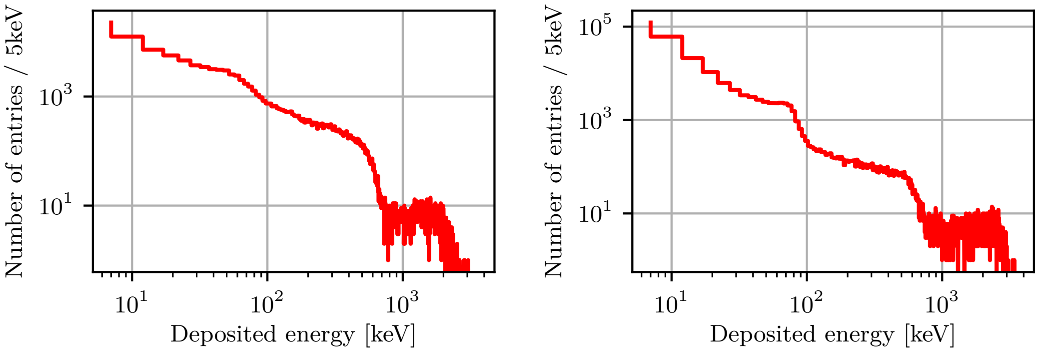

(e) $V_{\text{bias}} = 10\,\text{V}$ (f) $V_{\text{bias}} = 20\,\text{V}$

Figure 6.3.2: Deposition spectra of the ^{241}Am-alpha source for (a) $V_{\text{bias}} = 0.3\,\text{V}$, (b) $V_{\text{bias}} = 1\,\text{V}$, (c) $V_{\text{bias}} = 2\,\text{V}$, (d) $V_{\text{bias}} = 5\,\text{V}$, (e) $V_{\text{bias}} = 10\,\text{V}$, (f) $V_{\text{bias}} = 20\,\text{V}$. I_{krum} is set to 7 nA. The shape of the deposition spectra change with different bias voltages. For bias voltages higher than 5 V, events with energies above 1 MeV are observed.

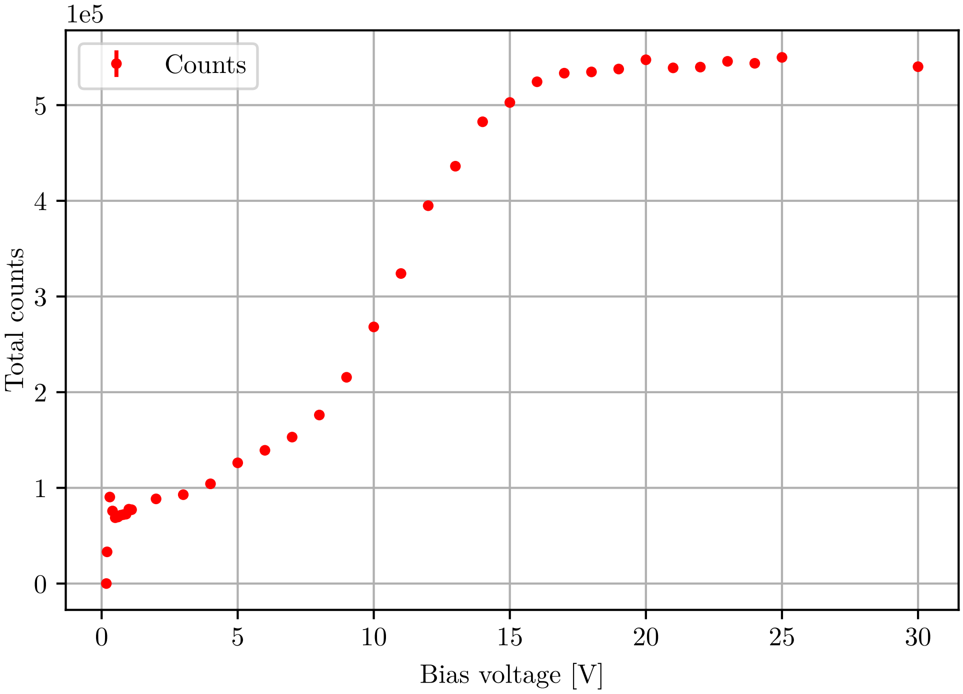

Figure 6.3.3: Number of registered events in the Dosi-mode summed over all large pixels depending on the applied bias-voltage. The irradiation was performed with a ^{241}Am-alpha source. I_{krum} is set to 7 nA. A clearly different course in comparison to photons (figure 6.2.11) is observed. The uncertainties were calculated via Poisson statistics.

6.4 Detector response to electrons

A ^{90}Sr/^{90}Y beta minus source is used to study the detector response to electrons with respect to bias voltage variation. 90Sr decays into 90Y. Latter one has a small half life of 2.67 d [[Eckb]]. Therefore, a 90Sr beta spectrum is always accompanied by a 90Y spectrum. The average energies of the electrons emitted by ^{90}Sr and ^{90}Y are 196 keV and 934 keV, respectively ([Ecka]). ToT and Dosi-Mode are used separately for investigation of the influence of the bias voltage on the shape and the total counts of the measured energy deposition spectra. The used bias voltages are in the range between $V_{\text{bias}} = 300\,\text{mV}$ and $V_{\text{bias}} = 30\,\text{V}$. From $V_{\text{bias}} = 300\,\text{mV}$ up until $V_{\text{bias}} = 1\,\text{V}$, the bias voltages are regarded in steps of $\Delta V_{\text{bias}} = 100\,\text{mV}$. Between $V_{\text{bias}} = 1\,\text{V}$ and $V_{\text{bias}} = 20\,\text{V}$, the step between the investigated bias voltages is $\Delta V_{\text{bias}} = 1\,\text{V}$. Additionally, bias voltages $V_{\text{bias}} = 25\,\text{V}$ and $V_{\text{bias}} = 30\,\text{V}$ are used. I_{krum} is set to 7 nA. The exposure time for each measurement is 10 minutes.

At first, the influence of the bias voltage variation of the shape of the spectrum is investigated. Figure 6.4.1 shows a few spectra of the ^{90}Sr-source. The energy deposition spectra of the electrons are following a Landau distribution convolved with a Gaussian, which results from the detector resolution. The Landau distribution results from the passage of an electron of sufficient energy through a thin material - here the silicon sensor. However, the peak of this Landau distribution shifts with different bias voltages. Because the sensor is not entirely depleted at small bias voltages and therefore the effective sensor thickness becomes smaller with decreasing bias voltages, the electrons deposit less energy in the corresponding detection volume. In order to investigate this shift in energy, the Moyal-function which is an approximation of the Landau-distribution is fitted to every spectrum which is shown as a red line in figure 6.4.1. The formula of the Moyal-function is ([KW16]):

$$f(x) = a \cdot \exp\left(-\frac{1}{2}\left(\frac{x-b}{c} + \exp\left(-\frac{x-b}{c}\right)\right)\right) + d \tag{6.4.1}$$

Here, a corresponds to the amplitude, b is the peak position, c the width and d the offset of the function. In order to investigate how the spectra shift, the fit parameter b which represents the position of the peak is plotted as a function of the bias voltage which is shown in figure 6.4.2. The uncertainties are calculated via the error of the fit parameters. From 300 mV up until 1 V, the slope is very steep. At higher bias voltages, the course changes and the slope becomes smaller. A saturation can be observed at 12 V implying that the sensor is fully depleted at $V_{\text{bias}} = 12\,\text{V}$. This is consistent with the result in [Ull21] but in conflict with the result from figure 6.3.3 since full depletion of the sensor seems not to occur at a bias voltage of 12 V yet for alpha particles. By the interaction of photons with the sensor material, electrons are produced which deposit energy. So, for both types of particles, photons and electrons, the energy is deposited by electrons which explains the comparable courses of the total counts as a function of the bias voltage. However, for alphas particles, the alpha particles itself deposit energy in the sensor material. So, it is a different energy deposition, which could be the reason for the different course.

Dosi-Mode is utilized to investigate the dependence of the event rate with respect to bias voltage variation which is shown in figure 6.4.3. The uncertainties are calculated from Poisson statistics. The course is similar to the one in figure 6.4.2. The saturation also occurs at a bias voltage of approximately 13 V which is in good agreement with the depletion voltage gained from the peak positions. However, the event rate decrease again at higher bias voltages. A reason for this could be that charge sharing is suppressed at high bias voltages because of the larger drift velocity which reduces the spread of the radius of the charge cloud. By comparing figures 6.3.3 and 6.4.3, it is clearly visible that Dosepix responds very differently to the different kinds of particles.

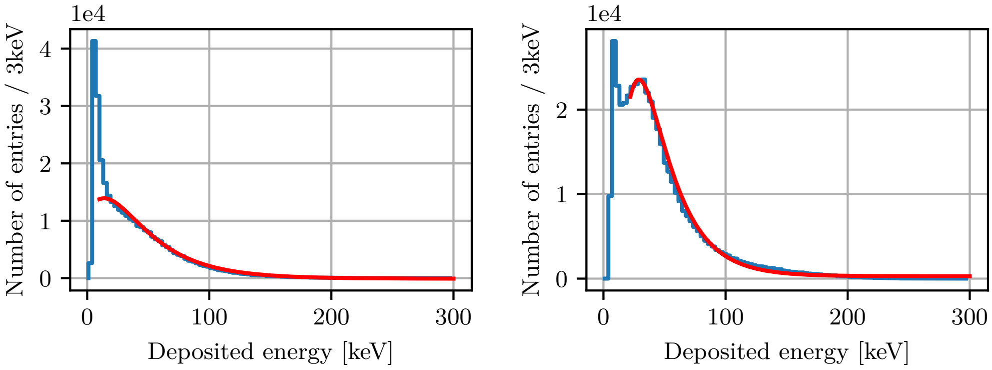

(a) $V_{\text{bias}} = 0.3\,\text{V}$

(b) $V_{\text{bias}} = 0.7\,\text{V}$

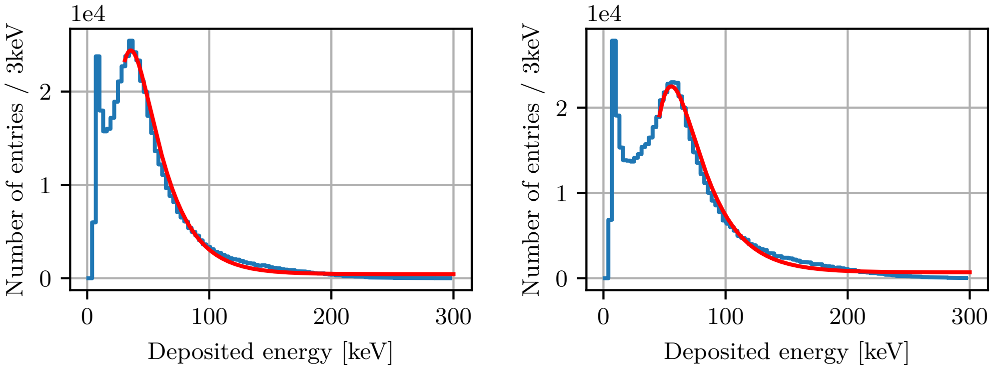

(c) $V_{\text{bias}} = 1\,\text{V}$

(d) $V_{\text{bias}} = 4\,\text{V}$

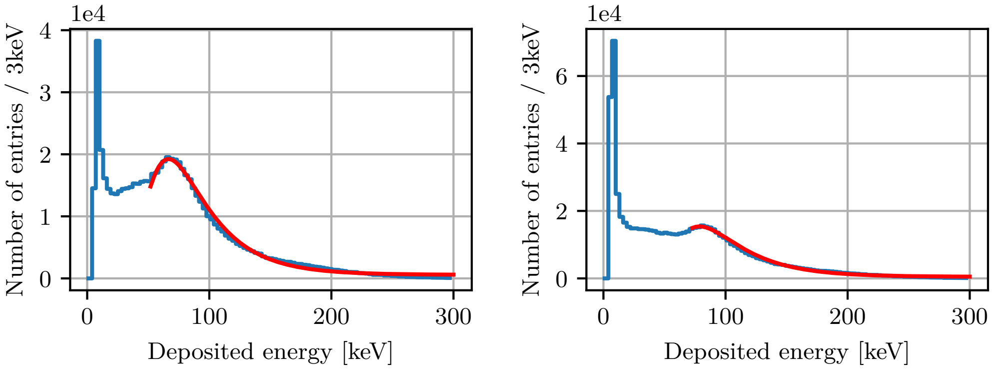

(e) $V_{\text{bias}} = 7\,\text{V}$

(f) $V_{\text{bias}} = 20\,\text{V}$

Figure 6.4.1: Deposition spectra of the ^{90}Sr-electron source at the bias voltages (a) 0.3 V, (b) 0.7 V, (c) 1 V, (d) 4 V, (e) 7 V and (f) 20 V. I_{krum} is set to 7 nA. The landau distribution moves to higher energies with increasing bias voltage. The red curves show a Moyal fit to the data.

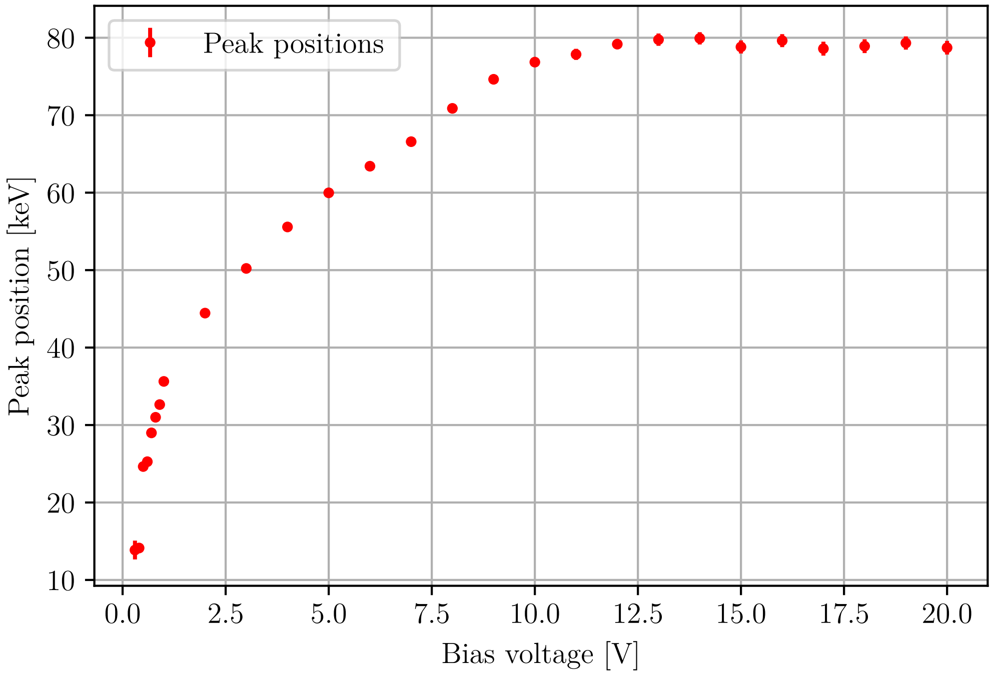

Figure 6.4.2: Peak positions as a function of the bias voltage. Saturation occurs at about 13 V. The uncertainties are determined by the error of the fit parameters.

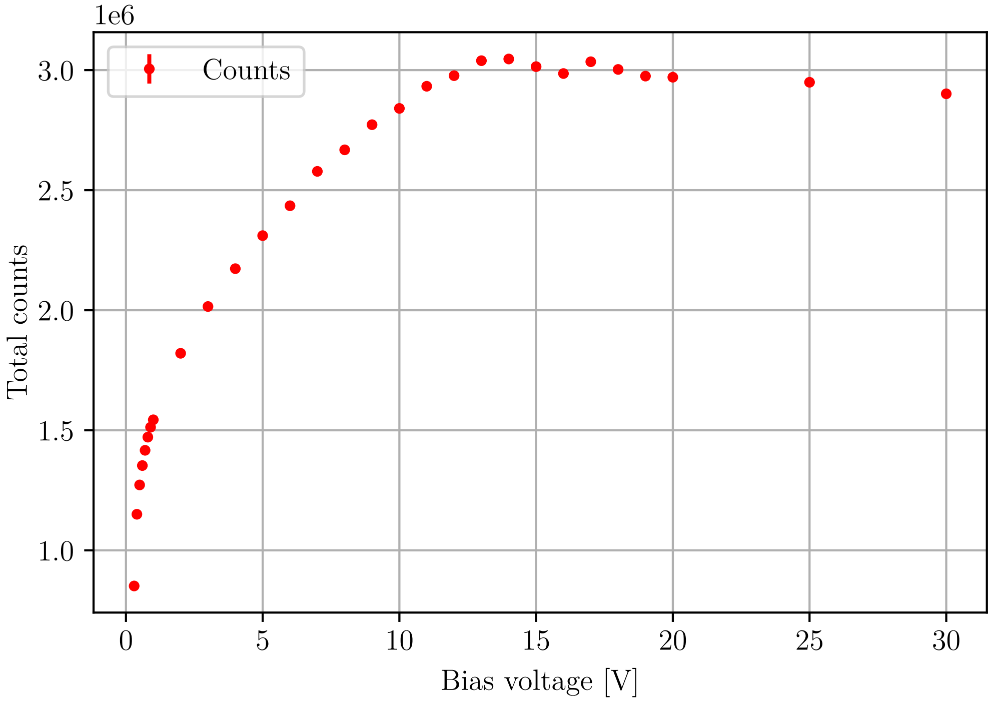

Figure 6.4.3: Number of registered events in Dosi-mode summed over all large pixels depending on the applied bias voltage. The irradiation was performed with a ^{90}Sr-source. I_{krum} is set to 7 nA. Saturation occurs at about 13 V which is in accordance with figure 6.4.2. The uncertainties are calculated from Poisson statistics.

6.5 Conclusion

In this chapter, the effective sensor thickness was reduced by applying a smaller bias voltage than the default one of 100 V for the three-detector-setup and 48 V for the single-detector-setup. Different particles types were used, including photons, alpha particles and electrons. The investigations focused on the reduction of pile-up and the behavior of Dosepix at different bias voltages.

It is shown that the event rate is significantly reduced by lowering the bias voltage which reduces the pile-up for high dose radiation which is important to measure radiation that is used in FLASH radiotherapy. The reason for the reduced event rate is the smaller effective sensor thickness since the sensor is not entirely depleted at small bias voltages. By lowering the bias voltage, a calibration with the corresponding bias voltage is needed since the deposition spectra are dependent on the bias voltage. The investigation of the behavior of Dosepix on different kinds of particles lead to the result that photons and electrons show a similar behavior. The determined bias voltage at which the sensor is completely depleted is about $V_{\text{bias}} = 12\text{V}$ which is in agreement with [Ull21]. However, for alpha particles this determined value is at about $V_{\text{bias}} = 17\,\text{V}$ or even higher. Also, the total counts as a function of the bias voltage show a different course as for photons and electrons.

7 In-phantom measurements

Contents

In this chapter, an investigation with respect to a clinical application of Dosepix is conducted. For this purpose, Dosepix is placed at different positions within a self-constructed water phantom. The total deposited energy within Dosepix is used as an estimate of the dose at the corresponding depth in water. The aim is to measure depth dose distributions, allowing conclusions of the sort and energy of the primary particle. The dose rates applied in this chapter are not in the range of FLASH radiotherapy since these investigations are a feasibility study for application of Dosepix. In the following, the setup will be presented. Afterwards simulations of the setup are conducted to deliver an expectation for the measurements. Then, measurements at the Strahlenklinik Erlangen ([Strb]) are presented.

7.1 Setup

Figure 7.1.1 illustrates a scheme of the water phantom from the top view. The dark blue regions are the walls of the water phantom. They are made out of polymethyl methacrylate (PMMA) and have a thickness of 8 mm, except for the entrance window on the right side, which is 3 mm thick. The bottom part of the phantom consists of 8 mm PMMA while the top part is open. The phantom has an external dimension of 300 mm x 307 mm x 526 mm, where the axis of the long side is perpendicular to the plane of the entrance window and 307 mm is the hight of the phantom. Aluminum rails with stepper motors are mounted outside the water phantom. One stepper motor is positioned on the rail perpendicular to the entrance window and is connected to the rail parallel to the entrance window. The second stepper motor moves a plate connected to an electric cylinder on top and a PMMA cylinder positioned inside the water. The height of said PMMA cylinder is with 38.8 cm larger than the water level to ensure that no water can enter. The PMMA cylinder is hollow and has a diameter of 50 mm with a wall strength of 2 mm. The bottom has a thickness of 6 mm. Dosepix is connected to the electric cylinder, which adjusts the position of the Dosepix detector on the axis parallel to the electric cylinder. Overall, this setup allows 3D movement of Dosepix within the water phantom. Figure 7.1.2 shows a photograph of the water phantom. The used stepper motors are the LA421S07-B-TJCA ([Ste]) from Nanotec ([Nan]), and the electric cylinder is the DSZY1-POT ([Ele]) from MSW Motion Control GmbH ([MSW]). The electric cylinder has a total range of 300 mm and is driven via an Arduino Uno Rev3 ([Ard]). In contrast, the two stepper motors are driven by the

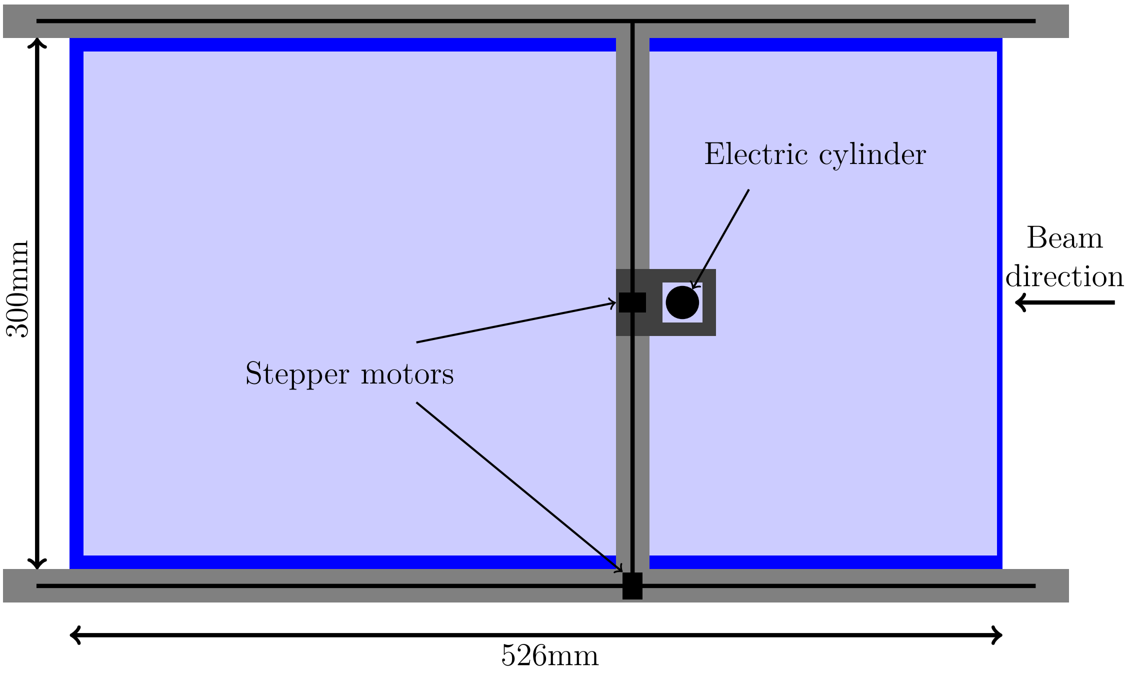

Figure 7.1.1: Scheme of the water phantom. Dosepix is located within a PMMA cylinder which is connected to stepper motors allowing arbitrary positions within the water phantom. Dosepix is connected to an electric cylinder which adjusts the position of the detector parallel to the axis of the electric cylinder within the PMMA cylinder.

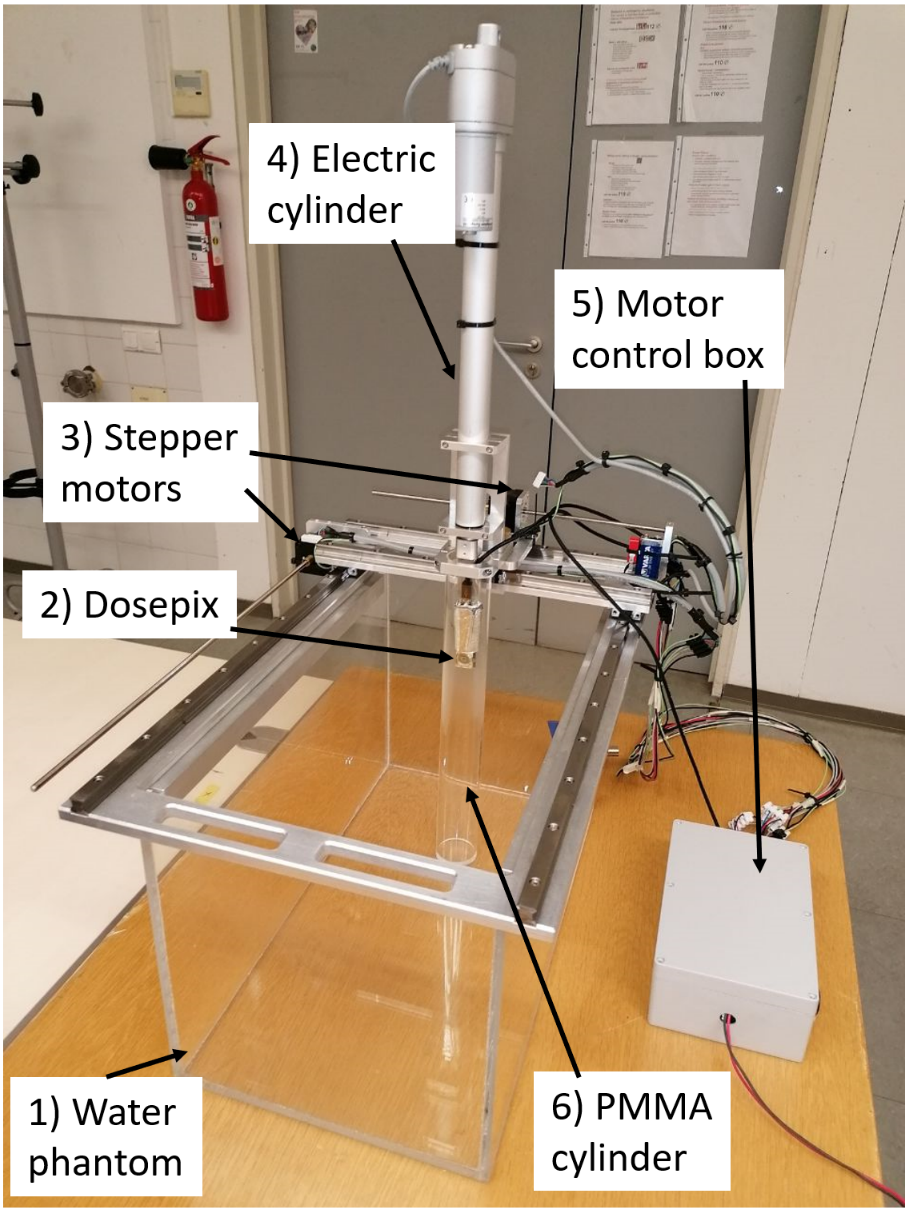

Figure 7.1.2: Photograph of the water phantom setup. 1) is the water phantom itself, 2) the Dosepix detector. 3) shows the two stepper motors, which move the electric cylinder (4), together with the PMMA cylinder (6) along the plane parallel to the bottom of the phantom. Dosepix is connected with the electric cylinder which adjusts the position of Dosepix inside the PMMA cylinder. The boards controlling the stepper motors and the electric cylinder are positioned inside the motor control box (5).

stepper motor controller TMCM-6110 ([TMC]) from Mocontronic System GmbH ([Moc]). The commands of both boards are executed via a python script. The minimal distance between the outer side of the PMMA cylinder and the inner side of the entrance window of the water phantom is 2 mm. The minimal distance of Dosepix to the bottom plate is 3 cm.
A single Dosepix detector setup is used for measurements inside the water phantom. A 300 µm thick silicon sensor is attached to the ASIC and the applied bias voltage is 48 V.

7.2 Simulations

The setup described in the previous section is simulated via Geant4 ([Gea]), a toolkit simulating the interaction of particles with matter. The geometries, sources, and target material can be selected as required. The water phantom, excluding the aluminum rails, stepper motors and electric cylinder, is constructed in the simulation. Depth dose curves in water are simulated first, before including the hollow PMMA cylinder with the Dosepix detector in the simulation. The particles of interest are electrons and protons. These simulations are followed up with simulations including the PMMA cylinder and the detector, i.e., depth dose curves with the energy deposited in Dosepix' sensor. This is realized by utilizing Allpix^2 ([All]), a simulation framework for pixel detectors. Allpix^2 is a simulation framework for silicon detectors, including the interaction of ionizing radiation with the sensor [SSW23]. Allpix^2 allows the implementation of the whole construction of the Dosepix detector, yielding deposited charges in the sensor.

7.2.1 Depth dose distribution in water

As mentioned before, first, simulations determining the depth dose distribution of different particle types in the water phantom are performed. The water inside the phantom is divided into slices with a thickness of 1 mm perpendicular to the entrance window. Geant4 yields particle tracks with a certain energy deposited within the track range. For simplicity, it is assumed that the complete deposited energy within one track is deposited at an arbitrary point on the track. The total energy deposited in each slice is determined yielding the depth dose distribution. It is performed for electron as well as proton radiation. The used physics list in the simulations is "FTFP_BERT_EMY", which is a reference physics list provided by Geant4.

Simulations with electrons

The first simulated particle type are electrons. Two electron energies were investigated: 6 MeV and 15 MeV. These two energies were chosen, since these energies are the upper and lower limit of the provided electron energies in the Strahlenklinik Erlangen [Strb]. The number of simulated events is 1 million. The distance between the entrance window and the focal spot of the accelerator is 1 m. The geometry of the simulated source is a quadratic plane 5 cm x 5 cm field aligned parallel to the entrance window of the water phantom. The entrance window of the water phantom is irradiated centrally. The curves of depth dose distributions are illustrated by considering the relative dose. Therefore, it is sufficient to determine the deposited energy in each water slice, since the mass of the water slices is a constant factor. The determined depth dose distributions for both energies are shown in figure 7.2.1. The determined relative doses per slice are shown as a function of the corresponding water depth. The relative dose is obtained dividing the curve by its maximal value. For 6 MeV electrons, the dose rises until it reaches its maximum at about 10 mm water depth, followed by a steep decrease of the dose. Similar behavior is observed for simulations with 15 MeV electrons. The dose rises until its maximum at approximately 40 mm water depth, followed by a decrease of dose.

The increase of dose at small water depth is explained by the dose build-up effect. The electrons scatter with the atoms of the water, resulting is oblique flight directions compared to their original direction. Additionally, the primary electrons produce further secondary electrons, increasing the particle fluence. This leads to an increasing dose at small water depths. It is visible that the relative dose at the entrance into the water phantom is higher for 15 MeV electrons compared to 6 MeV electrons. For smaller energies, the probability for electrons to scatter at higher angles in increased. This causes a quicker increase of the dose. [SPO]

In the following, the practical range R_p of electrons in water is determined. The practical range is defined as the depth at which a linear interpolation of the decreasing dose intersects the background radiation produced by bremsstrahlung ([SPO]). In the simulations, the depth dose distribution at large water depth is not zero, but a certain amount of dose is still observed. This corresponds to the bremsstrahlung background. In order to gain a value for this background, the mean of the relative dose values near the steep decrease is calculated, since the background in this region is similar to the one at the practical range. This is performed for water depth between 30 mm and 40 mm for 6 MeV electrons and between 80 mm and 90 mm for 15 MeV electrons. The uncertainties on the background are determined by the standard error, which is the standard deviation on the mean value divided by the square root of the number of regarded measurements. The steep decrease in dose is fitted via a linear function. The determined practical range for 6 MeV electrons is 24.5 ±0.7 mm and for 15 MeV electrons 69.5±0.6 mm. Uncertainties are determined

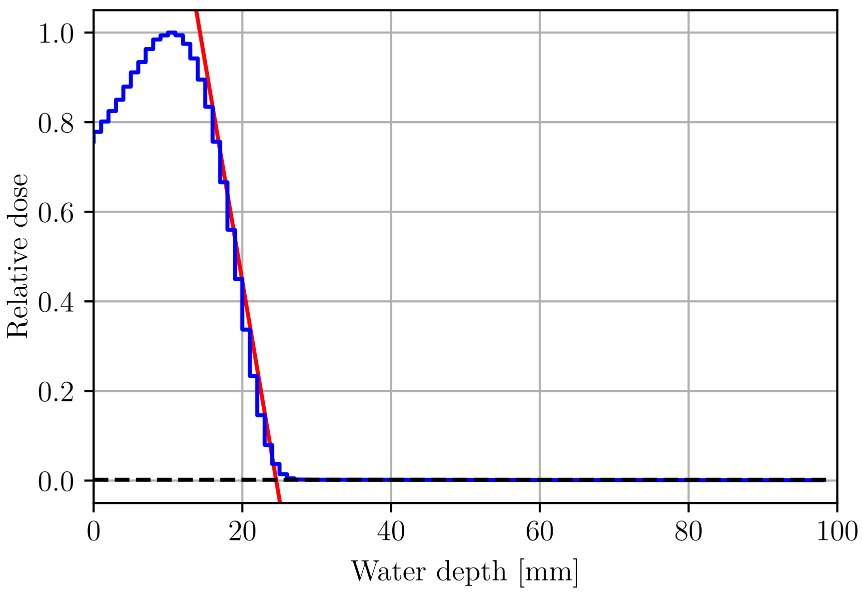

(a) 6 MeV electrons

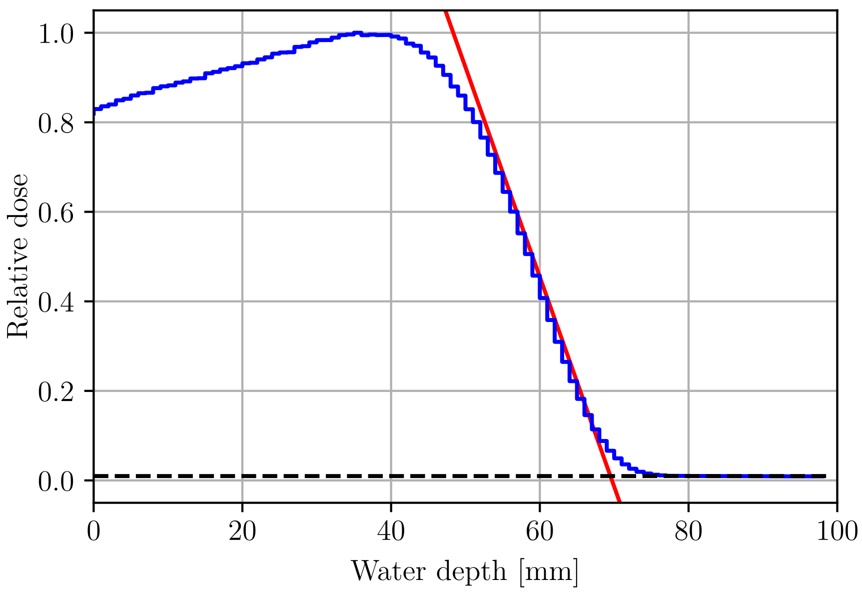

(b) 15 MeV electrons

Figure 7.2.1: Simulated depth dose distributions of 6 MeV electrons (a) and 15 MeV electrons (b). The number of simulated events is 1 million. The dashed black line shows the level of bremsstrahlung background. The practical range is determined by the intersection of the bremsstrahlung background with a linear function fitted to the decrease of relative dose.

by Gaussian error propagation with the uncertainties on the background and the fit function. The procedure is illustrated in figure 7.2.1. The dashed black lines show the level of background resulting from bremsstrahlung and the red lines are the linear function, where the simulated data at steep decrease in dose is fitted to. The practical range of electrons in water is determined by the intersection of the background level and the linear fit. The simulations were performed in order to gain information about the development of deposited energy of electrons within the water phantom and the practical range of the particles in water.

Simulations with protons

Protons are also potential candidates for FLASH radiotherapy [SHF$^+$20]. Therefore, simulations were performed with protons with an energy of 150 MeV, which is within the range for typical energies of proton therapy of 60 MeV to 250 MeV ([SHF$^+$20]). The geometry and analysis are the same as for the simulations with electrons. The depth dose distribution is shown in figure 7.2.2. The absorbed dose shows a slight decrease at small water depths, leading to the Bragg peak, which appears for heavy charged particles at their stoppage. The exact position of the Bragg peak was determined by fitting a function of the following form to the simulated data ([Lam15]):

$$D(d_{\mathrm{W}}) = \alpha \exp\left(\frac{\tau^2\sigma^2}{2} + \tau(d_{\mathrm{W}} - \mu)\right) \cdot \mathrm{erfc}\left(-\frac{\mu - d_{\mathrm{W}}}{\sigma\sqrt{2}} + \frac{\tau\sigma}{\sqrt{2}}\right) \tag{7.2.1}$$

Here, $D(d_{\mathrm{W}})$ is the dose at a certain water depth d_{W}. The parameter μ corresponds to the peak position, which is used to determine the range of protons in water. The applied fit to the simulated data is shown in figure 7.2.2 as a dashed red line. The determined range of 150 MeV protons in water is 154.120 ± 0.023 mm. In this thesis, no measurements with protons were performed, but because of the large size of the water phantom, this setup can be used for future investigations with proton radiation. Additionally, the obtained data can be used for dose estimations.

7.2.2 Simulations including Dosepix

In this section, simulations with Dosepix within the water phantom are performed. For this, Allpix^2 is used. The Dosepix detector was implemented, allowing the simulation of deposited energy within Dosepix' sensor. Allpix^2 determines the response of the detector to ionizing radiation. The deposited charge in the pixels are stored for each event. In Allpix^2, the value for the required energy to produce an electron-hole pair is set to 3.64 eV ([SM69]). From this value, the deposited energy is calculated. The simulations are performed with electrons of an energy of 6 MeV as well as 15 MeV. The distance between the focal spot of the accelerator and the

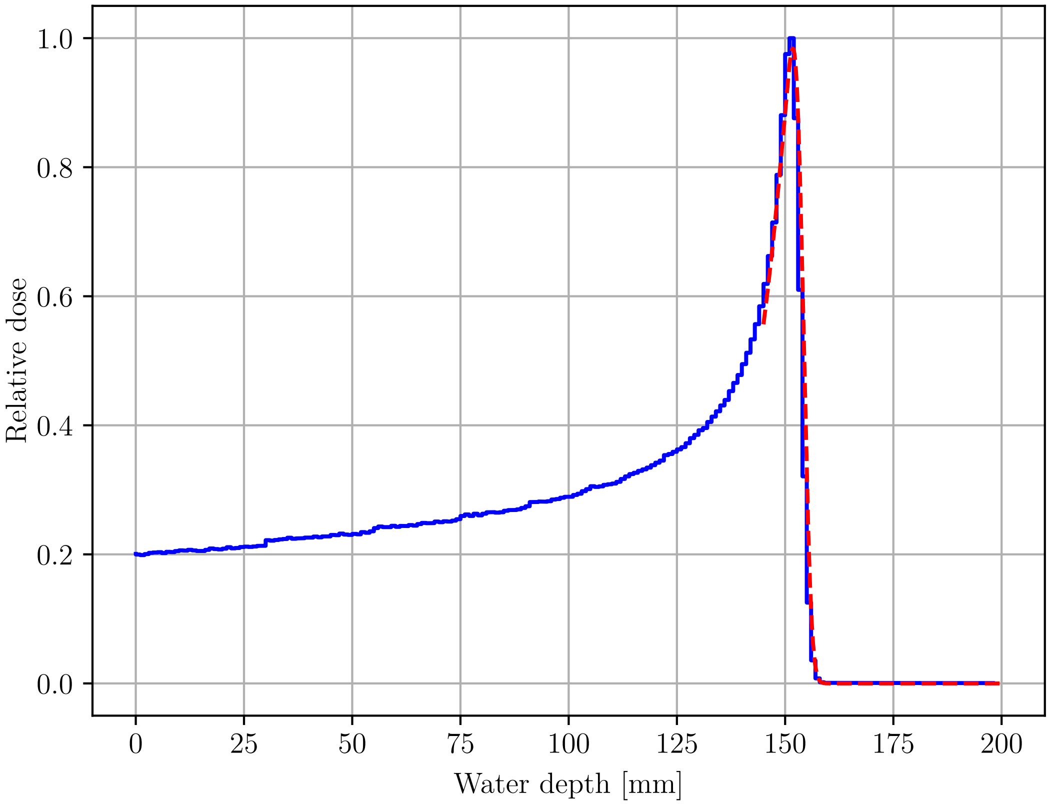

Figure 7.2.2: Simulated depth dose distribution of 150 MeV protons with Geant4. The number of simulated events is 1 million. The position of the Bragg peak is determined via a fit shown as a dashed red line, yielding the range of the protons of approximately 154 mm in water.

entrance window is 1 m. The beam has a dimension of 5 cm x 5 cm, parallel to the entrance window of the water phantom which is irradiated centrally. The number of simulated particles is 10 million for the simulations with 15 MeV electrons and 50 million for 6 MeV electrons. The determined energy deposition spectra for different positions of Dosepix in the water phantom are shown in figure 7.2.3. The number of counts were histogramed. The energy deposition spectra are normalized to the largest value determined at 2 mm water depth in the regarded energy range. The water depth is the distance between the inner side of the phantom and the outer side of the PMMA cylinder. A Landau distribution is observed for all water depths and both electron energies with the peak at about 75 keV. However, the ratio between the number of counts corresponding to the peak of the Landau distribution and the total number of counts over the whole spectrum decreases with increasing water depths because of background bremsstrahlung. Furthermore, the probability for electrons not to impinge on the detector perpendicularly rises, since the number of interactions for the single electrons increases with increasing water depth. This results in different track lengths through the sensor, leading to contributions at smaller energies since multiple pixels register the deposited energy.
The deposition spectrum for 15 MeV electrons was also binned for the used energy bins listed in table 7.3.1 since they are used for the measurements in Dosi-mode described in section 7.3.2. The deposition spectra with the Dosi-mode bins is shown in figure 7.2.4.

In the following, the absorbed dose dependent on the water depth is investigated. The dose at a certain water depth is determined by summing up the deposited energy of all events. The relative dose is investigated, therefore it is sufficient to determine the deposited energy in the sensor material since the sensor's mass is only a constant factor. The resulting depth dose distributions are shown in figure 7.2.5. The relative dose is calculated by dividing all dose values by the largest one. It is observed that the absorbed dose stays constant for small water depths for both curves. The relative dose starts to decrease at a water depth of 4 mm for 6 MeV electrons, whereas for 15 MeV, the relative dose starts to decrease at a water depth of approximately 18 mm. Subsequently, a decrease of relative dose is observed. The relative dose drops near to zero at water depths matching the determined practical ranges from section 7.2.1.
Additionally, figure 7.2.6 shows the normalized number of counts dependent on the water depth. The number of counts increases with the water depth at small penetration depths. A reason for this behavior is the rising number of photons produced by the interaction of electrons with water, which is explained by the dose build-up effect.
The number of counts starts to decrease at a water depth of approximately 4 mm

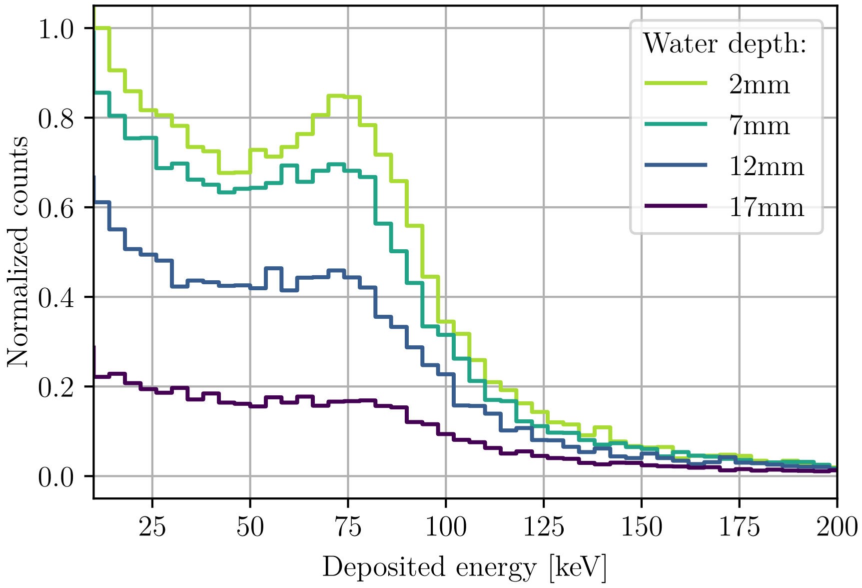

(a) 6 MeV electrons

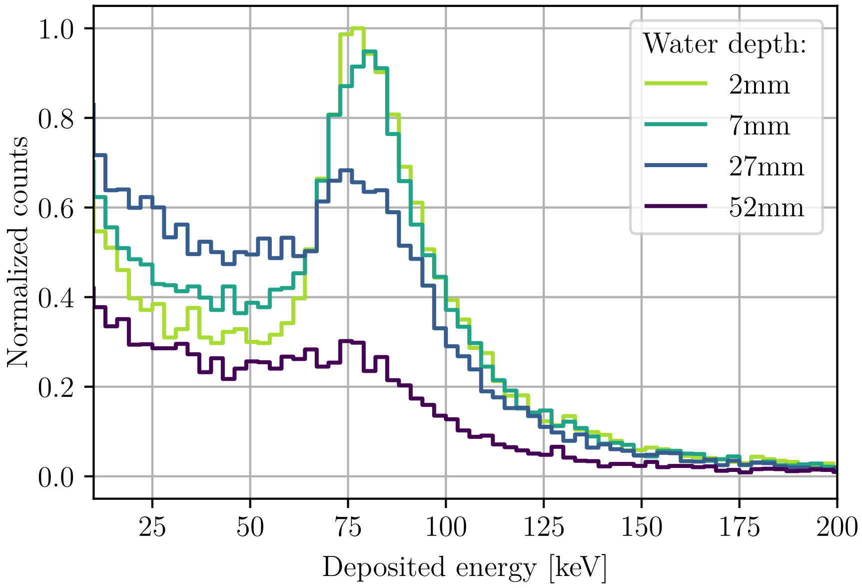

(b) 15 MeV electrons

Figure 7.2.3: Simulated energy deposition spectra with Allpix^2 for electrons with an energy of (a) 6 MeV and (b) 15 MeV at different water depths within the water phantom. A Landau distribution is observed with the peak at approximately 75 keV. The ratio between the number of counts in the peak of the Landau distribution and the total number of counts over the whole spectrum decreases with increasing water depths.

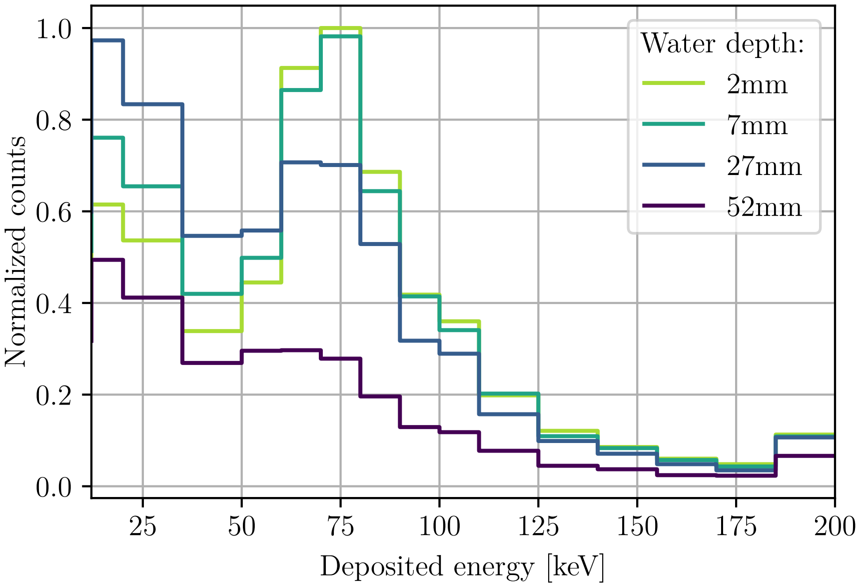

Figure 7.2.4: Simulated energy deposition spectra for 15 MeV electrons shown in 7.2.3(b) binned according to Dosi-mode measurements discussed in section 7.3.2 with the energy bin ranges listed in table 7.3.1.

for 6 MeV electrons and 19 mm for 15 MeV electrons. The curves are similar to the depth dose distributions shown in figure 7.2.5. The simulations at 15 MeV correspond to the measurements performed at the Strahlenklinik Erlangen. The simulated data provides a rough expectation for measurements performed with Dosepix. However, also deviations from the simulations are expected since every event is simulated separately in Allpix^2, so no pile-up is considered. Nevertheless, the effect of pile-up can be investigated by comparing the simulations to the measured data.

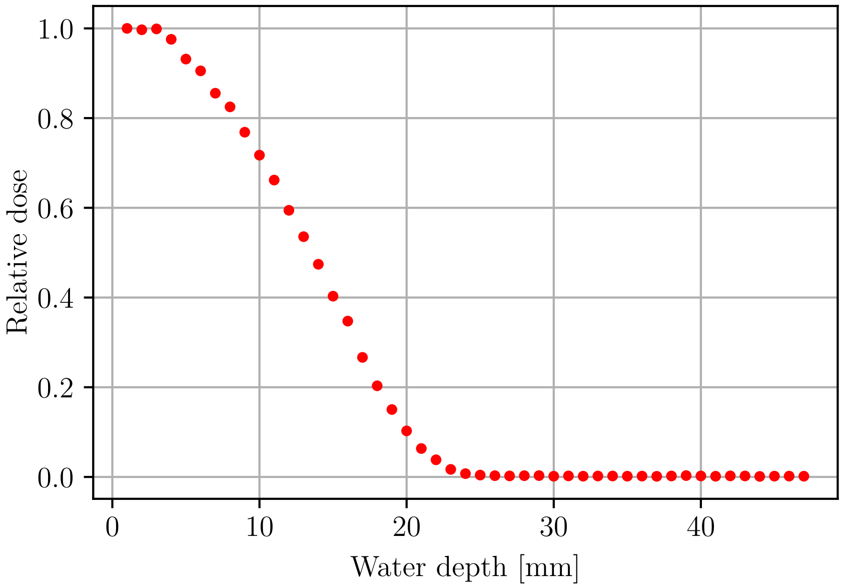

(a) 6 MeV electrons

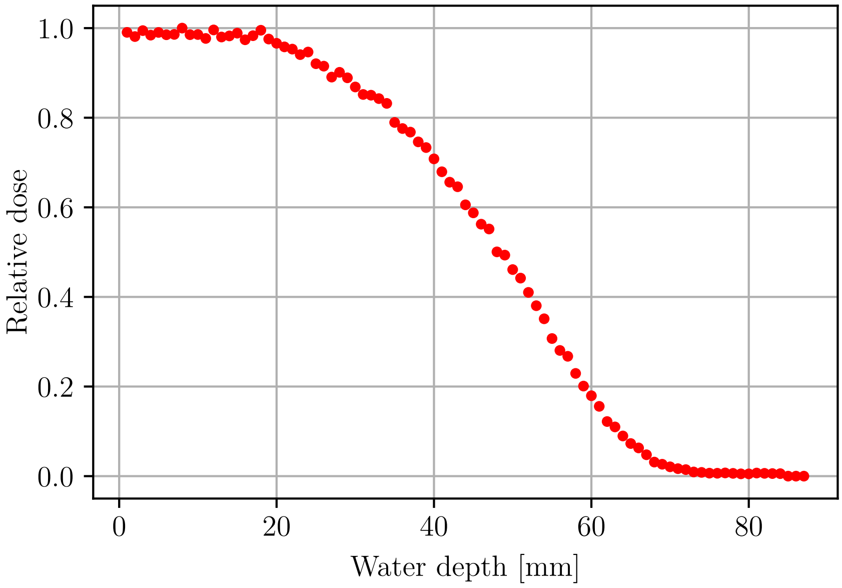

(b) 15 MeV electrons

Figure 7.2.5: Simulated depth dose distributions for electrons with an energy of (a) 6 MeV and (b) 15 MeV. The water depth is the distance between the inner side of the water phantom and the outer side of the PMMA cylinder. The relative dose stays nearly constant for small water depths and subsequently decreases.

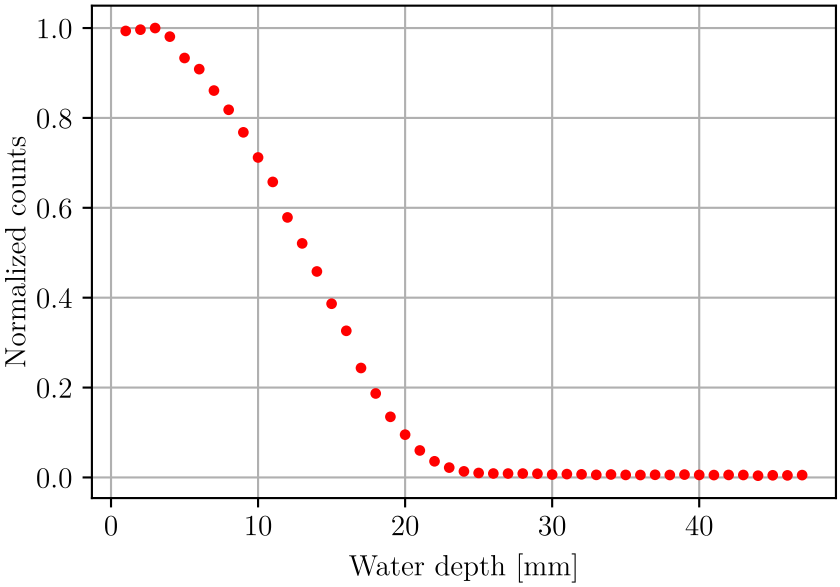

(a) 6 MeV electrons

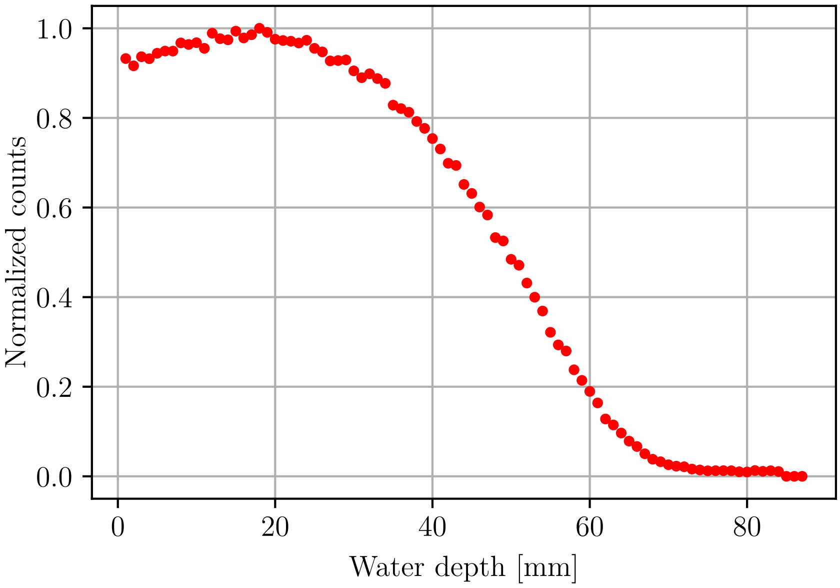

(b) 15 MeV electrons

Figure 7.2.6: Stored number of events normalized to the maximum number of events as a function of the water depth for (a) 6 MeV and (b) 15 MeV electrons. The water depth is the distance between the inner side of the water phantom and the outer side of the PMMA cylinder. The number of counts increases with rising water depth at small penetration depths. The rest of the curves are similar to the depth dose distributions shown in figure 7.2.5.

7.3 Measurements at Strahlenklinik

Corresponding to the simulations performed with electrons, measurements at the Strahlenklinik Erlangen ([Strb]) were performed with 15 MeV electrons. The used LINAC is a VersaHD by Elekta ([Ver]). This LINAC uses the technique of traveling waves. A pulse dose rate of 500 MU per minute is used where 100 MU corresponds to an applied energy dose to water of 1 Gy. The applied dose per pulse is approximately 0.4 mGy ([Corb]), which lies in the range of conventional radiotherapy. The pulse duration is 3 µs. The distance between the focal spot of the accelerator and the outer side of the water phantom was approximately 1 m. The beam has a dimension of 5 cm x 5 cm at the exit window of the accelerator. Said exit window is parallel to the entrance window of the water phantom. Laser-light was emitted from the gantry of the accelerator, which can influence the measurements since a high optical photon flux can cause registration of events because of pile-up. Single optical photons do not produce a charge signal exceeding the threshold level of Dosepix. However, for high photon fluxes, pile-up of many events produces a measurable signal. Therefore, a piece of paper was placed between the gantry and the water phantom in order to shield the light. However, a fraction of the light still passed the piece of paper. The readout board is covered by approximately 1 mm of lead to shield it from radiation. Dosi-mode is utilized to measure the depth dose distribution and the deposition spectra. The energy range of each bin is shown in table 7.3.1. The data acquisition time is approximately 10 s.

7.3.1 Reference measurements

At first, reference measurements without radiation were performed at three different water depths. The water depth is the distance between the phantom's inner side and the PMMA cylinder's outer side. The energy histograms gained from measurement utilizing Dosepix in Dosi-mode are shown in figure 7.3.1. Mainly, most events are registered in the first and the last energy bin. The number of counts decreases with increasing water depth, indicating that the measured events result from optical light emitted from the gantry. The threshold energy is much higher than the energy of optical photons, but pile-up of many thousands of optical photons leads to charge signals exceeding the threshold voltage. However, the large amount of registered events in the last energy bin is not typical for the influence of optical photons, so another unclear origin could be the reason. No overflow of the energy bins occurred. Reference also influences the measurements with electron radiation. However, the influence of the background radiation is negligible compared to the main signal caused by the primary electron beam. The deposition spectra of the electron radiation are determined next.

Bin number	Energy range
1	12 – 20 keV
2	20 – 35 keV
3	35 – 50 keV
4	50 – 60 keV
5	60 – 70 keV
6	70 – 80 keV
7	80 – 90 keV
8	90 – 100 keV
9	100 – 110 keV
10	110 – 125 keV
11	125 – 140 keV
12	140 – 155 keV
13	155 – 170 keV
14	170 – 185 keV
15	185 – 200 keV
16	$>$ 200 keV

Table 7.3.1: Used energy ranges of the Dosi-mode bins for measurements of electrons in the Strahlenklinik Erlangen.

7.3.2 Electron measurements

Dosepix is utilized in Dosi-mode to obtain energy histograms for electron irradiation at different water depths in the water phantom. The water depth was varied from 2 mm to 58 mm in steps of 2 mm and from 65 mm to 80 mm in steps of 5 mm. Additionally, a measurement at a water depth of 100 mm was performed. The obtained energy histograms at different water depths are shown in figure 7.3.2. All measurements show a large amount of registered events in the highest energy bin. This results from pile-up, caused by the high dose rate. Pile-up results in a distortion of the deposited energy and a reduced number of registered events. As a comparison, in the simulated energy deposition spectra binned corresponding to the bin edges in Dosi-mode, illustrated in figure 7.2.4, all high energetic simulated events were included in the highest energetic bin. For the simulated data, the last energy bin is much less dominant than in the measured data. In the simulations, no pile-up is included.

The spectra remain similar up until a water depth of about 40 mm. According to the simulation, a Landau distribution occurs at approximately 75 keV for all water depths if no pile-up occurs. A Landau distribution is observed at a water depths between 2 mm and 40 mm in the measurements. This peak moves from small to high energies in a range of approximately 40 keV to 70 keV with increasing

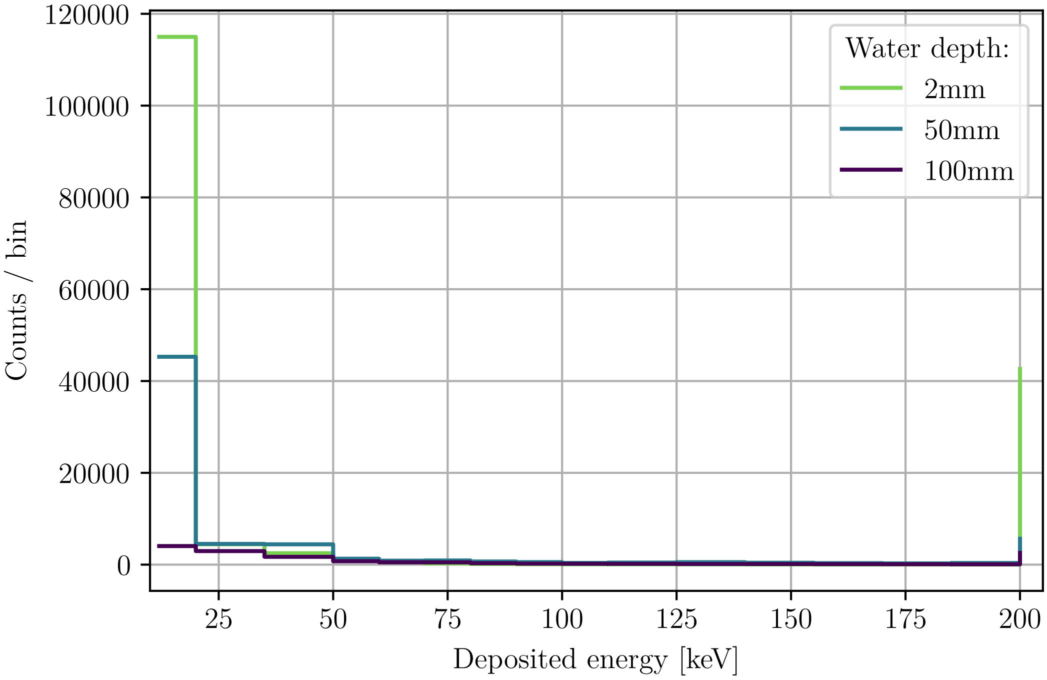

Figure 7.3.1: Reference measurements without electron radiation. Events are registered because of optical light emitted from the gantry. The number of total counts decreases with increasing water depth.

water depths. This could be explained by a shift of the threshold at high particle fluxes, which was investigated in [Sch21]. The observed peak does not appear as a Landau distribution at larger water depths and further moves to higher energies. At a water depth of 65 mm, the peak has moved into the last energy bin. Between 40 mm and 58 mm, many events are registered in the smallest energy bin. Pile-up and the shift of the peak cause severe problems for dosimetry since no accurate dose calculation is possible.

In order to investigate the energy deposition at higher energies, the bin ranges were changed to the ones listed in table 7.3.2. The remaining measurement parameters are the same as for the measurement with the bin ranges listed in table 7.3.1. The energy histograms are shown in figure 7.3.3. It has to be mentioned that the energy calibration is performed until 60 keV, resulting in inaccuracies determining the deposited energies of the events. Events with deposited energies of up to 2 MeV are registered contradicting the simulated data which shows maximum energy depositions at approximately 300 keV. These high energy events result from pile-up because of the large particle flux. The deposited spectra remain similar

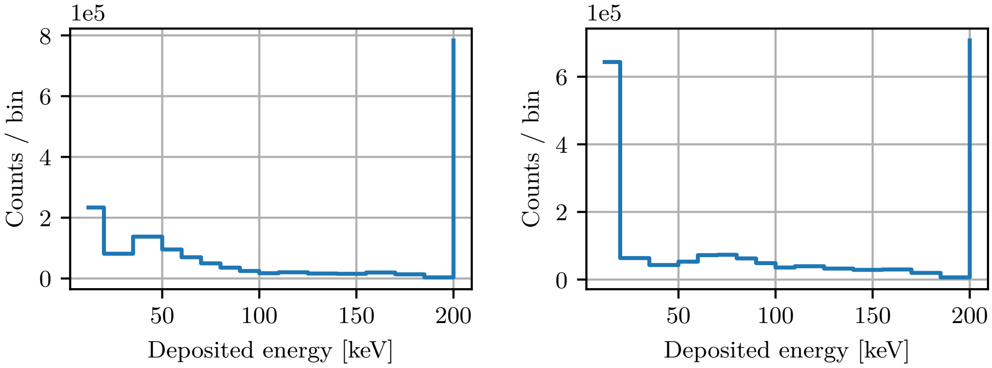

(a) $d_{\mathrm{W}} = 2\,\mathrm{mm}$

(b) $d_{\mathrm{W}} = 40\,\mathrm{mm}$

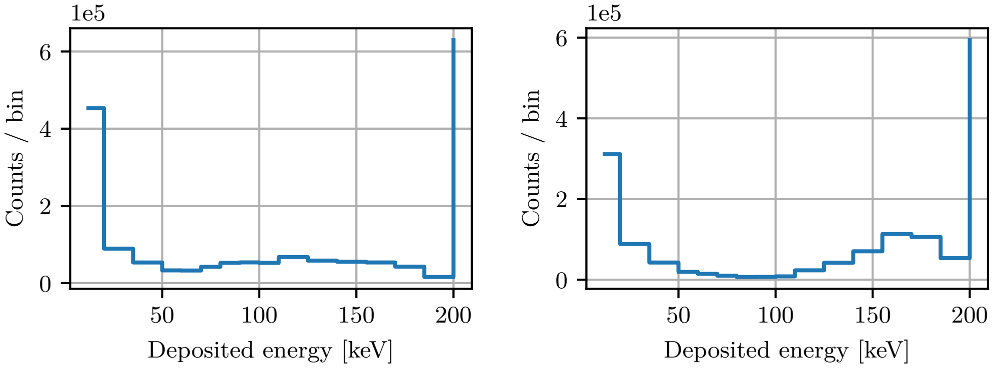

(c) $d_{\mathrm{W}} = 48\,\mathrm{mm}$

(d) $d_{\mathrm{W}} = 54\,\mathrm{mm}$

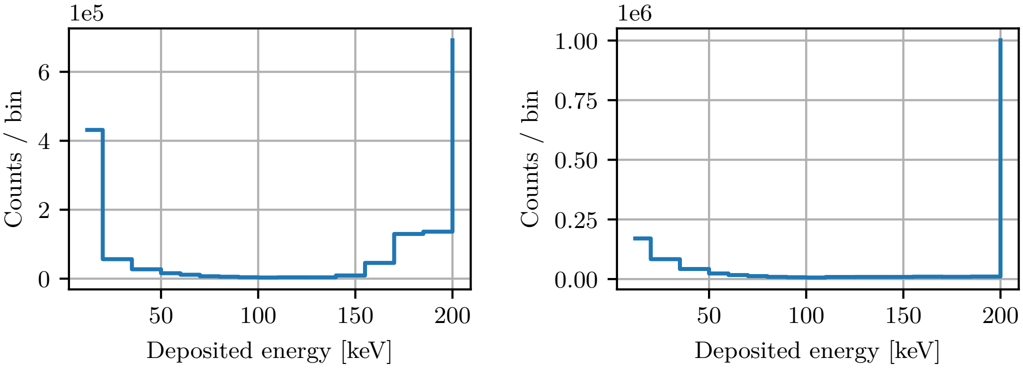

(e) $d_{\mathrm{W}} = 58\,\mathrm{mm}$

(f) $d_{\mathrm{W}} = 65\,\mathrm{mm}$

Figure 7.3.2: Energy histograms of electron radiation recorded in Dosi-mode at different water depths d_{W}. The huge amount of events in the last energy bin results from pile-up. The Landau peaks move to higher energies with increasing water depths.

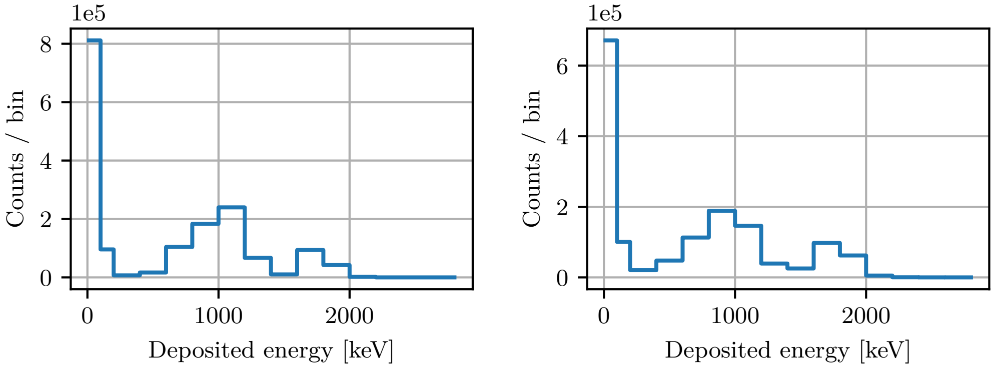

(a) $d_{\mathrm{W}} = 2\,\mathrm{mm}$

(b) $d_{\mathrm{W}} = 5\,\mathrm{mm}$

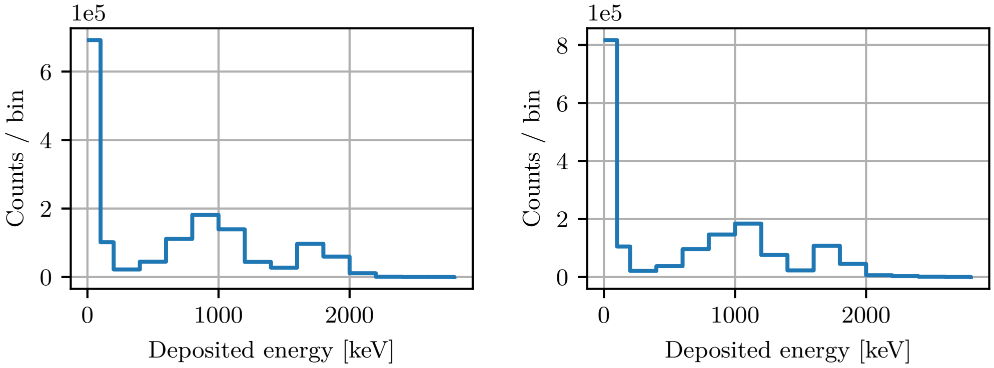

(c) $d_{\mathrm{W}} = 10\,\mathrm{mm}$

(d) $d_{\mathrm{W}} = 20\,\mathrm{mm}$

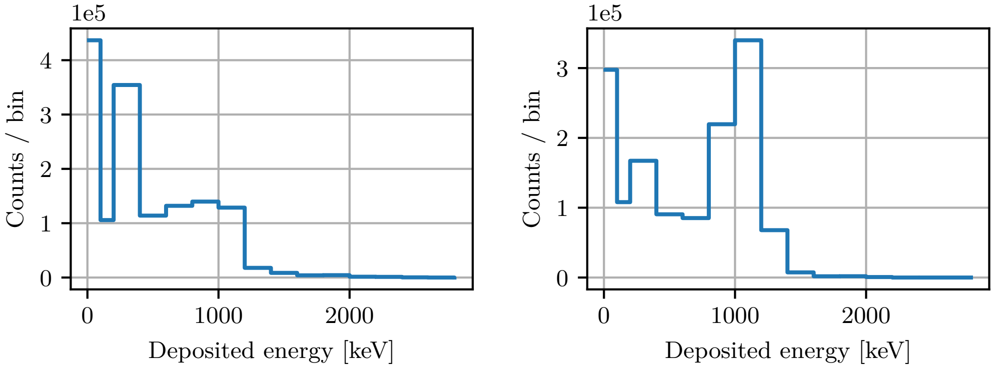

(e) $d_{\mathrm{W}} = 60\,\mathrm{mm}$

(f) $d_{\mathrm{W}} = 80\,\mathrm{mm}$

Figure 7.3.3: Energy histograms of electron radiation recorded in Dosi-mode with bigger bins up until 2.8 MeV. Up until 20 mm water depth d_{W}, the energy deposition spectra look similar. Peaks are observed at approximately 1 MeV and 1.7 MeV. In the deposition spectra at 60 mm and 80 mm water depths, the peak at 1.7 MeV vanishes and one appears at approximately 300 keV.

Bin number	Energy range
1	12 – 100 keV
2	100 – 200 keV
3	200 – 400 keV
4	400 – 600 keV
5	600 – 800 keV
6	800 – 1000 keV
7	1000 – 1200 keV
8	1200 – 1400 keV
9	1400 – 1600 keV
10	1600 – 1800 keV
11	1800 – 2000 keV
12	2000 – 2200 keV
13	2200 – 2400 keV
14	2400 – 2600 keV
15	2600 – 2800 keV
16	> 2800 keV

Table 7.3.2: Used energy ranges of the Dosi-mode bins for measurements of electrons in the Strahlenklinik Erlangen.

for the water depths of 2 mm to 20 mm. Two peaks are observed at approximately 1 MeV and 1.7 MeV. The peak at 1.7 MeV vanishes at a water depth of 60 mm and an additional peak appears at about 300 keV. At 80 mm water depth, the peak at approximately 1 MeV becomes bigger and the peak at about 300 keV smaller.

Next, measurements using ToT-mode were performed to determine the energy deposition spectra at different water depths in the phantom. The frame time of these measurements is set to 0.01 s. The total exposure time is approximately 10 s. The energy deposition spectra are shown in figure 7.3.4. At a water depth of 2 mm, a peak is visible at about 1 MeV. This peak still occurs at a water depth of 80 mm. However, the number of energy contributions at energies between approximately 100 keV and 500 keV increases and the amplitude of the peak at 1 MeV decreases. At a water depth of 100 mm, the peak at 1 MeV nearly vanishes, and the contribution of events between 100 keV and 500 keV become more dominant in comparison to smaller water depths. The reason for this behavior could be that pile-up is reduced at large water depths since the particle flux decreases, resulting in a smaller probability for events registered at very high energies.

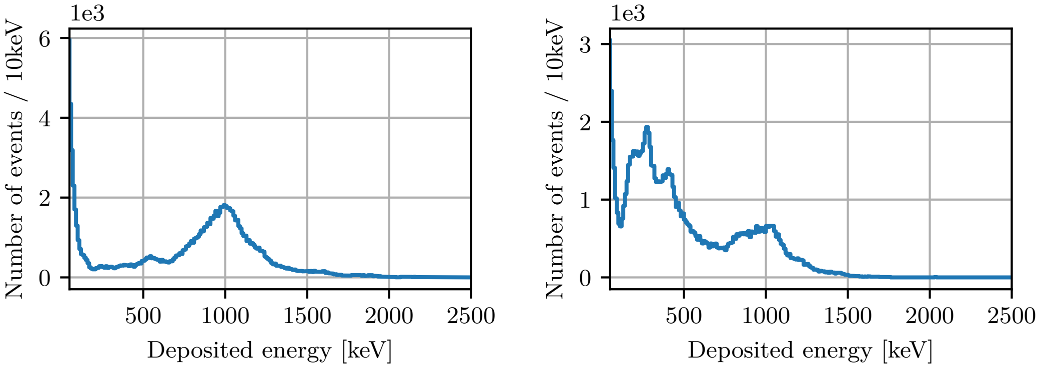

(a) $d_W = 2\,\mathrm{mm}$

(b) $d_W = 80\,\mathrm{mm}$

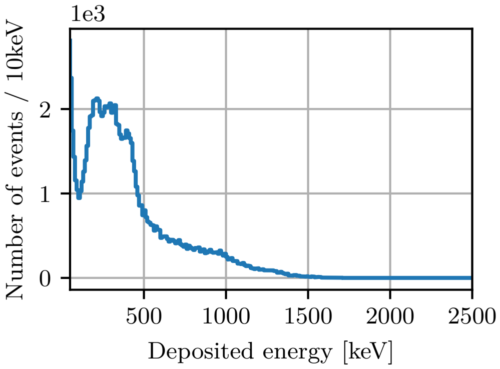

(c) $d_W = 100\,\mathrm{mm}$

Figure 7.3.4: Energy deposition spectra recorded in ToT-mode with a frame time of 0.01 s. The total exposure time is 10 s. The measurements were performed at different water depths d_W in the water phantom.

7.3.3 Depth dose distribution

The measurements with the energy bin ranges shown in table 7.3.1 are used to determine the number of events as a function of the water depth and the depth dose distribution. The number of events is calculated by summing up all registered events of all pixels within the measurement time except for the first and the last energy bin. The first energy bin, corresponding to the least energetic energy bin, is taken out from the evaluation because of the huge influence of optical light. The last energy bin, corresponding to the most energetic energy bin, is also influenced by optical light but also by pile-up. Pile-up results in measured numbers of events that do not match the actual amount of impinging particles since many particles contribute to a single registration. The effect of pile-up depends on the water depth. Therefore this energy bin is also excluded from the evaluation. The total number of counts dependent on the water depth is shown in figure 7.3.5. The uncertainties are determined by the Poisson error. The number of total counts experience a slight increase between 2 mm and 50 mm. This can be explained by the increasing number of particles at small water depths. The number of registered events steeply decreases until about 70 mm. This corresponds to the range of the electrons in water, matching the result from the simulation in figure 7.2.6(b). The course of the measurements series is explainable by pile-up. Pile-up results in a reduced amount of registered events, since multiple particles contribute to a single event. The number of events at large water depths cannot result only from the background since much less events were registered in the reference measurements. Therefore, these events result from photons produced by bremsstrahlung. Additionally, the threshold level is shifted at high particle flux which also has an influence on the number of registered events.

Compared to the simulated data shown in figure 7.2.6(b), the number of counts starts to decrease at a larger water depth, and the slope of this decrease is steeper than in the simulations. This is also expected, since pile-up is reduced at the range of the electrons leading to a sharper edge. However, the number of counts rises at small water depths, which matches the simulations.

The data recorded in Dosi-mode with the energy bins listed in table 7.3.1 is also used in order to determine the depth dose distribution. Again, the first energy bin is excluded from the calculation. The last energy bin is also not included since all events more energetic than the last energy bin edge are registered in this bin. Therefore, no borders for the deposited energy can be determined. For all other bins, the mean energy of each bin is multiplied by the number of registered events in the corresponding bins. This yields the energy registered in each energy bin. All energies are summed up for each measurement at a specific water depth. The values are normalized to the largest value. This yields the relative dose since the mass of the sensor is a constant factor. The corresponding data is visualized in figure

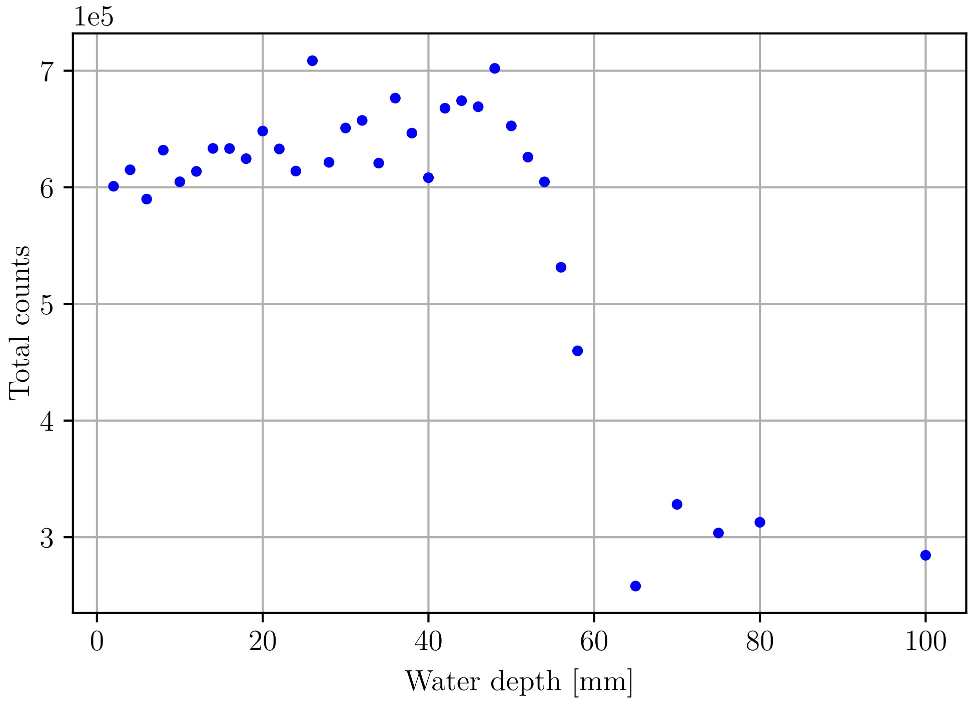

Figure 7.3.5: Total number of registered counts as a function of the water depth. The measurements in Dosi-mode with the bin edges shown in table 7.3.1 are used. The first and last energy bins are not included. The exposure time is 10 s. Between 2 mm and 50 mm, the number of counts slightly increases. At 50 mm water depth, the number of counts decreases steeply and remains at a nearly constant value for water depths higher than 75 mm. The statistical errors determined by the Poisson error are smaller than the data points.

7.3.6. The uncertainties of measured energy in each bin are determined via Poisson errors on the number of registered counts multiplied by the mean energy of the bins. The uncertainty on the deposited energy over all energy bins in then calculated by Gaussian error propagation. The deposited energy rises until a water depth of about 50 mm. This results from the shift of the Landau peak observed in figure 7.3.2 from small to high energies at increasing water depths. The practical range is calculated by the intersection of the background bremsstrahlung and a linear fit to the part of decreasing dose. The background level is calculated by the mean value of the data points corresponding to the five largest water depths. The uncertainties on the background level is calculated by Gaussian error propagation. A linear function was fitted to the deposited energy values at the water depths of 56 mm, 58 mm and 65 mm. Since only three data points belong to the linear part of the curve, the gained uncertainties are large. The determined range is 64 ± 5 mm. The uncertainties are calculated via Gaussian error propagation. Figure 7.3.6 illustrates the determination of the practical range. Compared to the simulated data shown in figure 7.2.5(b), the curves differ at small water depths, and the dose starts to decrease at a much higher water depth than in the simulation which results from the shift of the threshold level and pile-up. However, the determined range of the electrons in water is similar to the expected value from the simulation.

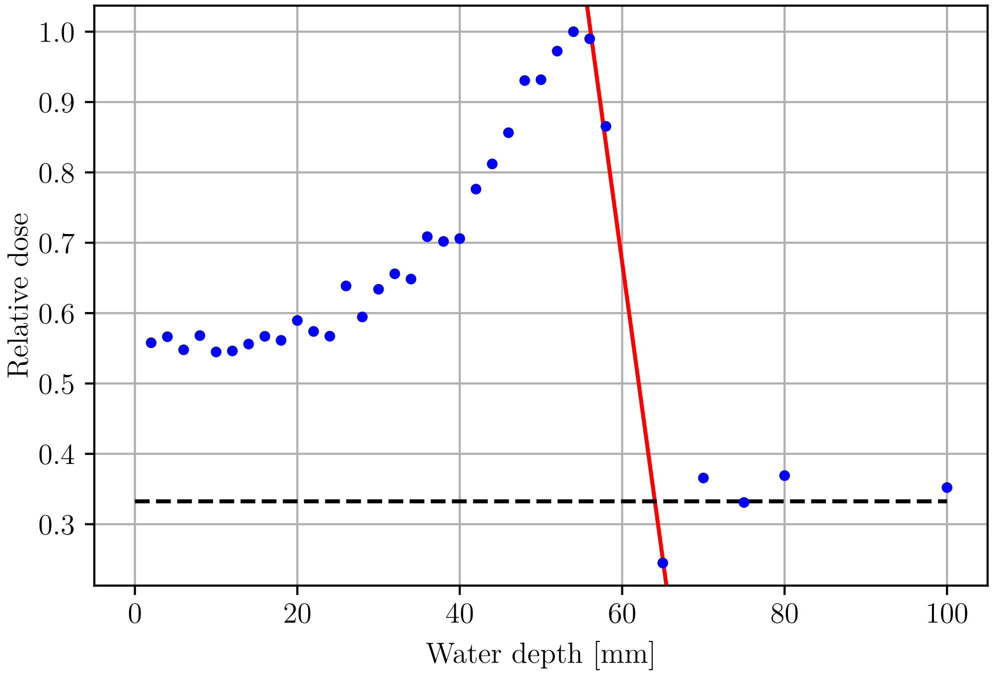

Figure 7.3.6: Measured dose depth distribution of 15 MeV electrons as a function of the water depth. The deposited energy is calculated by summing up the measured energies of all bins, excluding the first and last energy bin. The energies in each bin are determined by the multiplication of the mean energy and the number of measured events. The uncertainties are calculated via Gaussian error propagation over all uncertainties of the deposited energy in each energy bin, determined by the multiplication of the mean energy with the Poisson error on the number of measured events. The exposure time is 10 s. The deposited energy increases until a water depth of approximately 50 mm, followed by a steep decrease. The deposited energy stays nearly constant for water depths above 65 mm. The statistical errors are smaller than the data points. The practical range was determined via the intersection of the bremsstrahlung background (dashed black line) and a linear function (red line) fitted to the decrease of relative dose, yielding approximately 64 mm.

7.4 Conclusion

In this section, a water phantom was used to take measurements with Dosepix of clinical electrons at different water depths. At first, simulations were performed in Geant4, using 6 MeV and 15 MeV electrons in order to determine the depth dose distribution of these particles in matter. Additionally, the same was done for 150 MeV protons. Subsequently, simulation including the Dosepix detector were performed using Allpix^2. It yields the deposited energies in the sensor material, from which the energy deposition spectrum is determined. Additionally, the depth dose distribution was simulated. Measurements were performed at the Strahlenklinik Erlangen ([Strb]) using 15 MeV electrons. Dosepix was used to take measurements at different water depths in order to determine the depth dose distribution. Pile-up was observed leading to very different energy deposition spectra than yielded from the simulations. Additionally, the high particle flux leads to a shift of the threshold level, which prevents accurate dose measurements with Dosepix. In order to gain additional knowledge about the observed effects, simulations including pile-up are needed. Nevertheless, the depth dose distributions showed similarities with the simulated data.
All in all, Dosepix is not suitable for high dose radiation in the primary beam since pile-up and the shift of the threshold level results in wrong dose measurements. In order The used dose rates are not in the range of FLASH but conventional radiotherapy. Simulations including pile-up are needed to disentangle measured data from pile-up. Additionally, measurements in Integration-mode, as performed in [Huf22] could provide more valuable information. Different methods must be tested. Placing Dosepix outside the primary beam, measuring stray radiation, is a promising method. Another ansatz is the reduction of the effective sensor thickness, as investigated in chapter 6, together with the usage of the water phantom for dose measurements in the primary particle beam.

8 Summary and Outlook

This thesis deals with investigations on the suitability of dosimetry with the Dosepix detector at high dose rates, especially FLASH radiotherapy. For this kind of cancer therapy, high doses per beam pulse in the order of several Gy/s are used ([RSM$^+$20]), resulting in the so called FLASH effect. The surrounding healthy tissue is spared, while the induced tumor damage is similar to conventional radiotherapy at comparable total doses applied ([SHF$^+$20]). This makes FLASH radiotherapy a promising tool for future cancer therapies. Because of the high dose rates, dosimetry of FLASH radiotherapy is accompanied by challenges ([RSM$^+$20]). The aim of this thesis is to find ways to deal with high dose rate radiation for measurements with the Dosepix detector.

First, a Dosepix-ionisation-chamber was built. It is realized by gluing a copper plate into the cover of Dosepix, which is utilized without a sensor. This allows the application of a negative voltage to the copper plate, resulting in the formation of an electric field between the copper plate and the detectors' ASIC. The Dosepix-ionisation-chamber is placed into the primary beam with the plane of the ASIC parallel to the beam axis. Secondary electrons are produced by the interaction of the primary particles with the air between the copper plate and the ASIC. These electrons are accelerated towards the ASIC, where the deposited charge is measured.
The Dosepix-ionisation-chamber showed the best results at the maximal applicable bias voltage of 2 kV, limited by the voltage supply. A huge time dependency of the measured signal is observed, resulting probably from the collection of electrons on the unsensitive part of the ASIC. This time dependency leads to problems in the reproducibility, prohibiting the extraction of knowledge from the measurements. No valuable information was obtained at investigations with an x-ray tube and clinical electrons provided by the Strahlenklinik Erlangen ([Strb]).

Next, the effective sensor thickness was reduced, resulting in a decreased event rate. This is done by applying a smaller bias voltage than the default of 100 V. A measurable signal still occurs at a bias voltage of 300 mV. The investigations deal with the reduction of pile-up and the behavior of Dosepix at reduced bias voltages. The particles of interest are photons, monoenergetic as well as polyenergetic, alpha particles and electrons. For all particle types, the shape of the energy deposition spectra changed by applying different bias voltages. For dosimetric tasks, corrections via conversion factors are possible. A significant decrease of the event rate is observed for lowered bias voltages resulting in decreased pile-up. The event rate as a function of the bias voltage show similar courses for photons and electrons. In comparison, alpha particles show a differences to the other particles.

In the last chapter of this thesis, a water phantom was used to investigate the response of the Dosepix detector at different water depths. Simulations were performed in order to deliver information about the depth dose distribution and energy deposition spectra. Geant4 and Allpix Squared were used for the simulations. Measurement were performed at the Strahlenklinik Erlangen ([Strb]) using 15 MeV electrons. Within the measurement time of about 10 s, a dose of approximately 0.8 Gy is applied, corresponding to conventional radiotherapy. Pile-up is heavily influencing the energy deposition spectra resulting in large energy depositions up to several MeV. Additionally, a shift in energy is observed which may result from a shift of the threshold level at high particle fluxes. The range of the electrons is water was roughly determined correctly. The simulation yielded a practical range of 69.5 ± 0.5 mm, whereas the practical range determined from measurements is 64 ± 5 mm. However, dose measurements cannot be performed at the investigated conditions.

All in all, it was not achieved to create useful methods to measure the dose of high dose rates. The used dose rates applied at the Strahlenklinik correspond to conventional radiotherapy. Therefore, the presented methods are not suitable for dosimetry for FLASH radiotherapy. Different setups must be investigated. A possible method are measurements outside of the primary particle beam, measuring stray radiation. Additionally, the response of Dosepix to clinical radiation at a reduced effective sensor thickness was not investigated in this thesis. This could also provide a suitable method for dose measurements at high dose rates since pile-up is reduced.

Bibliography

[ADV] *ADVACAM.* https://advacam.com,

[All] *Allpix Squared.* `https://gitlab.cern.ch/allpix-squared/allpix-squared`,

[Ard] *Data sheet Arduino Uno Rev3.* `https://docs.arduino.cc/resources/datasheets/A000066-datasheet.pdf?_gl=1*vcm9j0*_ga*OTUyNjgwNjgwLjE2NzU2OTEzNTA.*_ga_NEXN8H46L5*MTY3NTY5MTM1MC4xLjAuMTY3NTY5MTM1MC4wLjAuMA..`,

[BCRM19] Bourgouin, Alexandra ; Cojocaru, Claudiu ; Ross, Carl ; McEwen, Malcolm: Determination of W_{air} in high-energy electron beams using graphite detectors. In: *Medical Physics, vol. 46, 11* (2019), S. 5195–5208

[BHF⁺14] Berry, Roger J. ; Hall, Eric J. ; Forste, David W. ; Storr, Thomas H. ; Goodman, Michael J.: Survival of mammalian cells exposed to X rays at ultra-high dose-rates. In: *British Journal of Radiology, vol. 42, 494* (2014)

[Boo] *Siemens Healthineers - Booneweb.* `https://bps.healthcare.siemens-healthineers.com/booneweb/index.html`,

[BR08] Behrens, R. ; Röttger, S.: Characterisation of Three High-energy Photon and Fast Neutron Reference Radiation Fields. In: *Radiation Protection Dosimetry 132(3)* (2008), S. 283–296

[BSH⁺20] Bourgouin, Alexandra ; Schüller, Andreas ; Hackel, Thomas ; Kranzer, Rafael ; Poppinga, Daniela ; Kapsch, Ralf-Peter ; McEwen, Malcolm: Calorimeter for Real-Time Dosimetry of Pulsed Ultra-High Dose Rate Electron Beams. In: *Frontiers in Physics, vol.8, 567340* (2020)

[CER] *CERN.* `https://home.cern/`,

[CHU] *CHUV.* https://www.lausanneuniversityhospital.com/home,

[Cora] *Personal correspondence with Dennis Haag on 13 February 2023*

[Corb] *Personal correspondence with Elekta on 16 February 2023*

[Dem17] Demtröder, Wolfgang: *Experimentalphysik 2 - Elektrizität und Optik - 7. Auflage.* Springer-Verlag Berlin Heidelberg, 2017

[Dem18] Demtröder, Wolfgang: *Atoms, Molecules and Photons - An Introduction to Atomic-, Molecularand Quantum Physics - Third edition.* Springer-Verlag Berlin Heidelberg, 2018

[Dur08] Durst, Jürgen: *Modellierung und Simulation physikalischer Eigenschaften photonenzählender Röntgenpixeldetektoren für die Bildgebung.* 2008

[EBT] *Gafchromic EBT.* `http://www.gafchromic.com/gafchromic-film/radiotherapy-films/EBT/index.asp`,

[Ecka] *Eckert & Ziegler - Beta sources BF-type.* `https://www.ezag.com/home/products/isotope_products/isotrak_calibration_sources/reference_sources/planchet_disk_sources/beta_sources_bf_type/`,

[Eckb] *Eckert & Ziegler - Special Isotopes.* `https://www.ezag.com/home/products/isotope_products/isotrak_calibration_sources/general_technical_information/special_isotopes/`,

[Ele] *Data sheet electric cylinder DSZY1-POT.* `https://www.msw-motion.de/wp-content/uploads/elekrozylinder/dszy1/dokumente/linearactuator_dszy1_pot.pdf`,

[EMP] *EMPIR - European Metrology Programme for Innovation and Research.* `https://www.euramet.org/research-innovation/research-empir`,

[Gab12] Gabor, Thomas: *Simulation und Experimente zur Anwendung eines neuartigen spektroskopischen Pixeldetektors in der Personendosimetrie*, Friedrich-Alexander Universität Erlangen-Nürnberg, PHD Thesis, 2012

[Gea] *Geant4 - A Simulation Toolkit.* `https://geant4.web.cern.ch/`,

[GGCF+22] Gómez, Faustino ; Gonzalez-Castaño, Diego M. ; Fernández, Nicolás G. ; Pardo-Montero, Juan ; Schüller, Andreas ; Gasparini, Alessia ; Vanreusel, Verdi ; Verellen, Dirk ; Felici, Giuseppe ; Kranzer, Rafael ; Paz-Martín, Jose: Development of an ultra-thin parallel plate ionization chamber for dosimetry in FLASH radiotherapy. In: *Medical Physics 49* (2022), S. 4705–4714

[GM18] Gross, Rudolf ; Marx, Achim: *Festkörperphysik - Dritte Auflage.* Walter de Gruyter GmbH Berlin/Boston, 2018

[Haa18] Haag, Dennis: *Active personal dosimetry with the hybrid pixelated DOSEPIX detector*, Friedrich-Alexander Universität Erlangen-Nürnberg, Master's Thesis, 2018

[HSH+22] Haag, Dennis ; Schmidt, Sebastian ; Hufschmidt, Patrick ; Anton, Gisela ; Ballabriga, Rafael ; Behrens, Rolf ; Campbell, Michael ; Eberle, Franziska ; Fuhg, Christian ; Hupe, Oliver ; Llopart, Xavier ; Roth, Jurgen ; Tlustos, Lukas ; Wong, Winnie ; Zutz, Hayo ; Michel, Thilo: Personal Dosimetry in Direct Pulsed Photon Fields with the Dosepix Detector. In: *IEEE TRANSACTIONS ON NUCLEAR SCIENCE* (2022)

[Huf22] Hufschmidt, Patrick: *Dosimetry with the Dosepix detector in pulsed high dose rate photon fields*, Friedrich-Alexander Universität Erlangen-Nürnberg, PHD Thesis, 2022

[IBA] *IBA Dosimetry.* `https://www.iba-dosimetry.com/`,

[IL08] Ibach, Harald ; Lüth, Hans: *Festkörperphysik - Einführung in die Grundlagen - 7. Auflage.* Springer-Verlag Berlin Heidelberg, 2008

[JCH+08] Jakubek, Jan ; Cejnarova, Andrea ; Holy, Tomas ; Pospisil, Stanislav ; Uher, Josef ; Vykydal, Zdenek: Pixel detectors for imaging with heavy charged particles. In: *Nuclear Instruments & Methods in Physics Research, vol. 591, 1* (2008), S. 155–158

[KDM+17] Krzyżanowska, A. ; Deptuch, G. ; Maj, P. ; Gryboś, P. ; Szczygieł, R.: Characterization of the Photon Counting CHAS Jr. Chip Built in a 40nm CMOS Process with a Charge Sharing Correction Algorithm Using a Collimated X-ray Beam. In: *IEEE Transactions on Nuclear Science, vol. 64, no. 9* (2017), S. 2561–2568

[Kno00] Knoll, Glenn F.: *Radiation Detection and Measurement - Third edition.* 2000

[KPW+21] Kranzer, Rafael ; Poppinga, Daniela ; Weidner, Jan ; Schüller, Andreas ; Hackel, Thomas ; Looe, Hui K. ; Poppe, Björn: Ion collection efficiency of ionization chambers in ultra-high dose-per-pulse electron beams. In: *Medical Physics 48 (2)* (2021)

[Kri17] Krieger, Hanno: *Grundlagen der Strahlungsphysik und des Strahlenschutzes.* Springer-Verlag Berlin Heidelberg, 2017

[Kri18] Krieger, Hanno: *Strahlungsquellen für Technik und Medizin.* Heidelberg, Berlin : Springer, 2018

[KSB+20] Kokurewicz, Karolina ; Schüller, Andreas ; Brunetti, Enrico ; Subiel, Anna ; Kranzer, Rafael ; Hackel, Thomas ; Meier, Markus ; Kapsch, Ralf-Peter ; Jaroszynski, Dino A.: Dosimetry for New Radiation Therapy Approaches Using High Energy Electron Accelerators. In: *Frontiers in Physics, vol.8, 568302* (2020)

[KSB+22] Kranzer, R. ; Schüller, A. ; Bourgouin, A. ; Hackel, T. ; Poppinga, D. ; Lapp, M. ; Looe, H. K. ; Poppe, B.: Response of diamond detectors in ultra-high doseper-pulse electron beams for dosimetry at FLASH radiotherapy. In: *Physics in Medicine & Biology 67 075002* (2022)

[KW16] Kolanoski, Hermann ; Wermes, Norbert: *Teilchendetektoren: Grundlagen und Anwendungen.* Springer-Verlag Berlin Heidelberg, 2016

[Lam15] Lambrechts, Koen: *Fitting the Bragg Peak for accurate proton range determination.* `https://fse.studenttheses.ub.rug.nl/13103/1/eindversie_bacheloronderzoek_K_1.pdf`, 2015

[Lin21] FLASH Radiotherapy: History and Future. In: *Frontiers in Oncology* (2021)

[MEG] *Siemens Healthineers - X-ray Tubes & X-ray Tube Assemblies.* `https://www.oem-products.siemens-healthineers.com/x-ray-tube`,

[Mes15] Meschede, Dieter: *Gerthsen Physik - 25. Auflage.* Springer-Verlag Berlin Heidelberg, 2015

[MET] *METAS.* https://www.metas.ch/metas/de/home.html,

[MFG+22] Marinelli, Marco ; Felici, Giuseppe ; Galante, Federica ; Gasparini, Alessia ; Giuliano, Lucia ; Heinrich, Sophie ; Pacitti, Matteo ; Prestopino, Giuseppe ; Vanreusel, Verdi ; Verellen, Dirk ; Verona, Claudio ; Rinati, Gianluca V.: Design, realization, and characterization of a novel diamond detector prototype for FLASH radiotherapy dosimetry. In: *Medical Physics 49* (2022), S. 1902–1910

[Moc] *Mocontronic System GmbH.* `https://www.mocontronic.de/`,

[MPS+02] Mathieson, K. ; Passmore, M.S. ; Seller, P. ; Prydderch, M.L. ; O'Shea, V. ; Bates, R.L. ; Smith, K.M. ; Rahman, M.: Charge sharing in silicon pixel detectors. In: *Nuclear Instruments and Methods in Physics Research A 487* (2002), S. 113–122

[MRL+20] McManus, M. ; Romano, F. ; Lee, N. D. ; Farabolini, W. ; A.Gilardi ; Royle, G. ; Palmans, H. ; Subiel, A.: The challenge of ionisation chamber dosimetry in ultra-short pulsed high dose-rate Very High Energy Electron beams. In: *Scientific Reports 10:9089* (2020)

[MSW] *MSW Motion Control GmbH.* `https://www.msw-motion.de/`,

[Nan] *Nanotec.* `https://de.nanotec.com/`,

[Nes14] Nesteruk, Konrad P.: Beam monitor detectors for medical applications. In: *Reports of Practical Oncology and Radiotherapy 19* (2014), S. 32–36

[NIS] *Stopping-Power & Range Tables for Electrons, Protons, and Helium Ions.* `https://www.nist.gov/pml/stopping-power-range-tables-electrons-protons-and-helium-ions`,

[NPL] *NPL.* `https://www.npl.co.uk/`,

[Nuc] *IAEA: Live Chart of Nuclides.* `https://www-nds.iaea.org/relnsd/vcharthtml/VChartHTML.html`,

[OBP+22] Oancea, C. ; Balan, C. ; Pivec, J. ; Granja, C. ; Jakubek, J. ; Chvatil, D. ; Olsansky, V. ; Chis, V.: Stray radiation produced in FLASH electron beams characterized by the MiniPIX Timepix3 Flex detector. In: *Journal of Instrumentation 17 C01003* (2022)

[PJG+17] Petersson, Kristoffer ; Jaccard, Maud ; Germond, Jean-Francßois ; Buchillier, Thierry ; Bochud, Francois: High dose-per-pulse electron beam dosimetry—A model to correct for theion recombination in the Advanced Markus ionization chamber. In: *Medical Physics, vol. 44, 3* (2017)

[PKF+20] Poppinga, Daniela ; Kranzer, Rafael ; Farabolini, Wilfrid ; Gilardi, Antonio ; Corsini, Roberto ; Wyrwoll, Vanessa ; Looe, Hui K. ; Delfs, Björn ; Gabrisch, Lukas ; Poppe, Björn: VHEE beam dosimetry at CERN Linear Electron Accelerator for Research under ultra-high dose rate conditions. In: *Biomedical Physics & Engineering Express 7 015012* (2020)

[PTW] *PTW Dosimetry - Advanced Markus Chamber.* `https://www.ptwdosimetry.com/fileadmin/user_upload/Online_Catalog/DETECTORS_Cat_en_16522900-14/blaetterkatalog/index.html#page_34`,

[Rad] *Radiation Dosimetry: What is Bragg Curve and Bragg Peak.* `https://www.radiation-dosimetry.org/what-is-bragg-curve-and-bragg-peak-definition/`,

[RFG+22] Rinati, Gianluca V. ; Felici, Giuseppe ; Galante, Federica ; Gasparini, Alessia ; Kranzer, Rafael ; Mariani, Giulia ; Pacitti, Matteo ; Prestopino, Giuseppe ; Schüller, Andreas ; Vanreusel, Verdi ; Verellen, Dirk ; Verona, Claudio ; Marinelli, Marco: Application of a novel diamond detector for commissioning of FLASH radiotherapy electron beams. In: *Medical Physics 49* (2022), S. 5513–5522

[RSM+20] Romano, F. ; Subiel, A. ; McManus, M. ; Lee, N. D. ; Palmans, H. ; Thomas, R. ; McCallum, S. ; Milluzzo, G. ; Borghesi, M. ; McIlvenny, A. ; Ahmed, H. ; Farabolini, W. ; Gilardi, A. ; Schüller, A.: Challenges in dosimetry of particle beams with ultra-high pulse dose rates. In: *Journal of Physics: Conference Series 1662 012028* (2020)

[Sch21] Schmidt, Sebastian: *Dosimetry and X-ray spectroscopy with the photon counting pixel detector Dosepix*, Friedrich-Alexander Universität Erlangen-Nürnberg, PHD Thesis, 2021

[SGKP22] Sommer, M. ; Granja, C. ; Kodaira, Satoshi ; Ploc, Ondřej: High-energy per-pixel calibration of timepix pixel detector with laboratory alpha source. In: *Nuclear Instruments and Methods in Physics Research Section A Accelerators Spectrometers Detectors and Associated Equipment* (2022)

[SHF+20] Schüller, Andreas ; Heinrich, Sophie ; Fouillade, Charles ; Subiel, Anna ; Marzi, Ludovic D. ; Romano, Francesco ; Peier, Peter ; Trachsel, Maria ; Fleta, Celeste ; Kranzer, Rafael ; Caresana, Marco ; Salvador, Samuel ; Busold, Simon ; Schönfeld, Andreas ; McEwen, Malcolm ; Gomez, Faustino ; Solc, Jaroslav ; Bailat, Claude ; Linhart, Vladimir ; Jakubek, Jan ; Pawelke, Jörg ; Borghesi, Marco ; Kapsch, Ralf-Peter ; Knyziak, Adrian ; Boso, Alberto ; Olsovcova, Veronika ; Kottlerf, Christian ; Poppinga, Daniela ; Ambrozova, Iva ; Schmitzer, Claus-Stefan ; Rossomme, Severine ; Vozenin, Marie-Catherine: The European Joint Research Project UHDpulse – Metrology for advanced radiotherapy using particle beams with ultra-high pulse dose rates. In: *Physica Medica 80* (2020), S. 134–150

[SKJ18] Schlegel, Wolfgang ; Karger, Christian P. ; Jäkel, Oliver: *Medizinische Physik*. Springer-Verlag Berlin Heidelberg, 2018

[SM69] Smithrick, John J. ; Myers, Ira T.: Average Triton Energy Deyosited in Silicon per Electron-Hole Pair Produced. In: *Physical Review 1, 2945* (1969)

[SPO] Strydom, W. ; Parker, W. ; Olivares, M.: *Electron Beam: Physical and clinical aspects*. `http://www-naweb.iaea.org/nahu/DMRP/documents/Chapter8.pdf`,

[SSW23] Schütze, Paul ; Spannagel, Simon ; Wolters, Koen: *Allpix Squared User Manual - Version v2.4.0*. `https://project-allpix-squared.web.cern.ch/usermanual/allpix-manual.pdf`, 2023

[Ste] *Data sheet stepper motors LA421S07-B-TJCA*

[Stra] *National Library of Medicine - X-ray Image Production Equipment Operation*. `https://www.ncbi.nlm.nih.gov/books/NBK564423/`,

[Strb] *Strahlenklinik Erlangen*. `https://www.strahlenklinik.uk-erlangen.de/`,

[TMC] *Data sheet TMCM-6110*. `https://www.mocontronic.de/wp-content/uploads/2015/07/TMCM-6110_ShortSpec.pdf`,

[UHD] *UHDpulse - Metrology for advanced radiotherapy using particle beams with ultra-high pulse dose rates*. `http://uhdpulse-empir.eu`,

[Ull21] Ullmann, Leonie: *Untersuchung und Analyse der Bias-Spannungs-Abhängigkeit des hybriden, photonenzählenden Pixeldetektors Dosepix*, Friedrich-Alexander Universität Erlangen-Nürnberg, Bachelor Thesis, 2021

[Ver] *Elekta - Versa HD*. `https://www.elekta.com/products/radiation-therapy/versa-hd/#slide1`,

[VFP$^+$19] Vozenin, Marie-Catherine ; Fornel, Pauline D. ; Petersson, Kristoffer ; Favaudon, Vincent ; Jaccard, Maud ; Germond, Jean-Francois ; Petit, Benoit ; Burki, Marco ; Ferrand, Gisele ; Patin, David ; Bouchaab, Hanan ; Ozsahin, Mahmut ; Bochud, Francois ; Bailat, Claude ; Devauchelle, Patrick ; Bourhis, Jean: The Advantage of FLASH Radiotherapy Confirmed in Mini-pig and Cat-cancer Patients. In: *Clinical Cancer Research 25* (2019), S. 35–42

[Won12] Wong, Winnie: *A Hybrid Pixel Detector ASIC with Energy Binning for Real-Time, Spectroscopic Dose Measurements*, Mid Sweden University, PHD Thesis, 2012

[XCO] *NIST - XCOM: Photon Cross Sections Database*. `https://www.nist.gov/pml/xcom-photon-cross-sections-database`,

[ZAB$^+$15] Zang, A. ; Anton, G. ; Ballabriga, R. ; Bisello, F. ; Campbell, M. ; Celi, J.C. ; Fauler, A. ; Fiederle, M. ; Jensch, M. ; Kochanski, N. ; Llopart, X. ; Michel, N. ; Mollenhauer, U. ; Ritter, I. ; Tennert, F. ; Wolfel, S. ; Wongb, W. ; Michel, T.: The Dosepix detector — an energy-resolving photon-counting pixel detector for spectrometric measurements. In: *Journal of Instrumentation, 10 C04015* (2015)

Danksagung

Zuletzt möchte ich allen Leuten danken, die mich während meiner Masterarbeit unterstützt haben:

PD Dr. Thilo Michel als Betreuer dieser Arbeit, ohne den diese Masterarbeit nicht möglich gewesen wäre. Vielen Dank für die angenehme Betreuung, der vielen Messideen und der stetigen Hilfsbereitschaft bei Fragen und Problemen aller Art.

Prof. Dr. Stefan Funk für die Übernahme der Zweitkorrektur dieser Arbeit. Ich freue mich auf die nächsten drei Jahre mit ihm als Doktorvater.

Dennis Haag als Betreuer dieser Arbeit und Ansprechpartner bei Fragen aller Art. Vielen Dank für die stetige Hilfsbereitschaft, Interpretieren von Messungen, der vielen Messideen und Hilfe bei sämtlichen Problemen rund um das Programmieren und Simulationen. Außerdem vielen Dank für das sehr ausführliche Korrekturlesen dieser Arbeit und den hilfreichen Verbesserungsvorschlägen.

Florian Beißer für das ausführliche Korrekturlesen mehrerer Kapitel und als stetiger Ansprechpartner bei Fragen rund um den Dosepix.

Sebastian Schmidt für seine Hilfsbereitschaft und Unterstützung bei Problemen aller Art in der Anfangsphase dieser Arbeit. Auch über seine Zeit beim ECAP hinaus war er immer als Ansprechpartner zur Stelle. Auch vielen Dank für die Beteiligung beim Konstruieren des Wasserphantoms und Beantwortung von Fragen technischer Art.

Naomi Vogel für das ausführliche Korrekturlesen eines Kapitels und den hilfreichen Verbesserungsvorschläge, vor allem bezüglich Sprache.

Carolin Kupillas, Patrick Hufschmidt und allen anderen Kollegen für das entspannte Arbeitsklima.

Constantin Rauch für seine Unterstützung bei der Lösung von Problemen rund um die Röntgenanlage.

Alfred Kaluza und Thorsten Kühn für ihre Unterstützung bei Problemen mit der Pumpe für die Röhrenkühlung.

Prof. Dr. Christoph Bert, Maya Shariff, Willi Stillkrieg und Manfred Schmidt von der Strahlenklinik Erlangen für das Ermöglichen von Messungen an der Strahlenklinik. Durch den sympathischen Umgang und Unterstützung bei den Messungen waren die kurzen Ausflüge innerhalb Erlagens immer sehr angenehm. Ein besonderer Dank an **Maya Shariff** für ihre hilfsbereite Art und Beantwortung vieler Fragen rund um die Beschleunigeranlagen.

Thomas Kurin als stetiger Ansprechpartner bei Fragen rund um die Ausleseboards.

Die Mitarbeiter der mechanischen Werkstatt für die Fertigung des Wasserphantoms.

Die Mitarbeiter der elektronischen Werkstatt für die Beantwortung von Fragen rund um die Motorsteuerung für das Wasserphantom.

Heike Wilhelm für die Unterstützung bei bürokratischen Angelegenheiten.

Meiner Familie für die stetige Unterstützung während des kompletten Studiums.

Statutory Declaration

I, Markus Schneider, hereby confirm that I produced this Master's thesis entirely by myself and that I used none than the presented tools and sources.

Erlangen, 17 February 2023 Markus Schneider